

Allowing Distributed Generation to Improve Power System Stability By Applying
Virtual Synchronous Machine Approach

A Dissertation

Presented in Partial Fulfillment of the Requirements for the

Degree of Doctor of Philosophy

with a

Major in Electrical Engineering

in the

College of Graduate Studies

University of Idaho

by

Mohamed M Abuagreb

Major Professor: Brian K. Johnson, Ph.D.

Committee Members: Herbert L. Hess, Ph.D.; Ahmed Abdel-Rahim, Ph.D.;

Yacine Chakhchoukh, Ph.D.

Department Administrator: Joseph D. Law, Ph.D.

May 2020

Authorization to Submit Dissertation

This dissertation of Mohamed M Abuagreb, submitted for the degree of Doctor of Philosophy with a major in Electrical Engineering and titled “Allowing Distributed Generation to Improve Power System Stability By Applying Virtual Synchronous Machine Approach,” has been reviewed in final form. Permission, as indicated by the signatures and dates given below, is now granted to submit final copies to the College of Graduate Studies for approval.

Major Professor: _____ Date: _____
Brian K. Johnson, Ph.D.

Committee Members: _____ Date: _____
Herbert L. Hess, Ph.D.

_____ Date: _____
Yacine Chakhchoukh, Ph.D.

_____ Date: _____
Ahmed Ibrahim, Ph.D.

Department
Administrator: _____ Date: _____
Joseph D. Law, Ph.D.

Abstract

The installed power capacity of DG is increasing; many of distributed generators are connected to a grid by inverters. The DC/AC inverters are controlled by a Phase Locked Loop (PLL) so they can be synchronized with power system frequency. If this capacity becomes larger, the grid power system become unstable, because the inverter is controlled to follow the power grid frequency. Performance of a photovoltaic generation (PV) plant with an integrated battery energy storage system (BESS) is examined under different system conditions. Although the penetration of distributed renewable energy sources into the traditional grid has risen over the past decade, the potential negative impact of this integration can never be overemphasized. The proposed scheme is evaluated in system studies under fluctuating levels of solar irradiation related to the weather conditions. As the changes in irradiation and temperature occur, the dc link voltage changes due to the changes in power produced, the inverter ac power is controlled to regulate the dc voltage. This research models are energy management system which is based on a hysteresis control algorithm for the battery, which limits the abrupt charging/discharging of the battery, thus increasing battery lifespan which also compensating for change in PV output and power system conditions.

The PV source does not have significant energy storage. However, it can supply small quantity of energy for the grid system because it has dc capacitor located in the dc link. Separate energy storage, such as a battery, can work with a PV source to supply energy for the frequency control. In addition, with increasing penetration of the inverter based power generation, there is decrease in inertia due to the fast frequency tracking of the PLL, which speed up dynamic behavior and stability problems on the power grid. To mitigate this problem, the integration of virtual synchronous generators (VSG) based on the photovoltaic (PV) generation plus energy storage is

proposed. This research implemented the VSG control based on the swing equation model of a synchronous generator. The VSG can be designed to aid the integration of large-scale photovoltaic generation into the power grid. Through this concept, it is plausible for the DG to exhibit the characteristics and behavior of synchronous generators (SG) such as inertia behaviour, droop functions and damping. These factors make it possible for the PV to contribute to the control and stability of the power grid.

The work also presents a proposed a simple method calculating approximate for approximating battery sizing with respect to power and energy by providing emulation inertia in order to meet the target system inertia and power/frequency characteristics. Three cases were simulated in order to calculate the amount of the battery energy sizing needed to support the power grid inertia which reduces the rate of change of frequency deviation.

These models are designed and simulated in the electromagnetic alternate transients program (ATP) to simulate the power system. The power grid is testing with the ATP program and validated with powerworld simulator.

Acknowledgements

Firstly, I would like to express my sincere gratitude to my advisor Prof. Brian Johnson for the continuous support of my Ph.D study and related research, for his patience, motivation, and immense knowledge. His guidance helped me in all the time of research and writing of this dissertation. I could not have imagined having a better advisor and mentor for my Ph.D study.

My appreciation is extended to the committee: Prof. Ibrahim and Prof. Chakhchoukh, for their insightful comments and encouragement.

Lastly, I would like to express my special appreciation and thanks to Prof. Hess who helped and supported me.

Dedication

To my Mom Ayada and my Dad Mohamed

To my wife Lila and my kids

To my brothers and sisters

Table of Contents

Authorization to Submit Dissertation	ii
Abstract.....	iii
Acknowledgements	v
Dedication	vi
Table of Contents	vii
List of Tables	xii
List of Figures	xiii
1 Introduction	1
1.1 Problem Description	5
1.2 Objectives	6
1.3 Literature Review	6
2 Power System Stability: An Overview	11
2.1 Power System Operation and Stability	11
2.1.1 Introduction.....	11
2.1.2 Definition of Power Stability	12
2.1.3 Power Angle Stability Classification.....	14
2.1.4 Voltage Stability.....	17
2.2 Dynamic Power Versus Angle Relationships	21
2.2.1 Swing Equation	23
2.2.2 Equal Area Criterion	25
2.3 Frequency Response Following a Grid Disturbance	27

2.3.1	Machine Inertia Response.....	28
2.3.2	Response of primary frequency control devices	28
2.3.3	Response of secondary frequency.....	30
2.3.4	Response of tertiary frequency	30
3	Matching Response of a Synchronous Machine and a Virtual Syn-	
	chronous Disturbances	31
3.1	Introduction	31
3.2	Synchronous machine (background).....	31
3.2.1	Synchronous generator assumptions.....	33
3.2.2	Reference frame orientation of SG	35
3.2.3	Equivalent circuits for D-axis and q-axis.....	37
3.2.4	Per Unit Synchronous Machine Stator Voltage Equations	37
3.2.5	Per Unit Synchronous Machine Rotor Voltage Equations.....	39
3.2.6	Synchronous Machine Stator and Rotor Flux Linkage Equations in pu.....	39
3.2.7	Power and Torque.....	41
3.3	Replication of a SG model in VSC Control	41
3.3.1	Introduction of Virtual Inertia	41
3.3.2	Reference Frame Orientation of virtual synchronous generator....	44
3.4	Utilizing a VSC for VSG.....	45
3.4.1	Droop Controller	46
4	Models for Inverter Coupled Generation and Storage.....	49
4.1	Voltage Source Converter.....	49
4.1.1	VSC Interconnection with AC Grid	50
4.1.2	VSC Power Controller	51
4.2	Controller Specifications and Design of VSC.....	53

4.2.1	Voltage Controller	54
4.2.2	Inner current control	55
4.2.3	High Pass Filter.....	57
4.2.4	Outer Loop Controller	59
4.2.5	DC Link Voltage Controller.....	59
4.2.6	Tuning of PI controllers.....	61
4.2.7	Tuning for Voltage Controller	61
4.2.8	Tuning for the Current Controller	63
4.3	Synchronization	64
4.3.1	Phase Locked Loop.....	64
4.4	Determining Battery Ratings and Description of Proposed Solution	68
4.5	Battery Sizing Calculations.....	68
4.6	Energy Storage System Power Capacity Calculation	70
4.7	Sizing the ESS to Enhance Stability	71
4.8	Power Balanced Based on Swing Equation	72
5	Utilizing Photovoltaic Generation Combined with Energy Storage	74
5.1	Design and Test of a Combined PV and Battery System Under Multiple Load and Irradiation Conditions (paper 1).....	74
5.1.1	Introduction.....	74
5.1.2	System Architecture	76
5.1.3	Simulation Results and Discussion	83
5.1.4	Conclusion	89
5.2	Energy Management of a Battery Combined with PV Generation (pa- per 2)	89
5.2.1	Introduction.....	89
5.2.2	System Architecture	91
5.2.3	DC Link Voltage Regulation Under Margins.....	99

5.2.4	Simulation Results and Discussion	100
5.2.5	Summary and Conclusion.....	104
6	Synchronous generator and Virtual synchronous generator design control and models.....	106
6.1	Implementation of Emulated Inertia using PV Generation with Energy Storage to Improve Integrated Grid Response (paper1)	106
6.1.1	Introduction.....	106
6.1.2	System description.....	108
6.1.3	Simulation Results and Discussion	115
6.1.4	Summary and Conclusion.....	121
6.2	Evaluation of Virtual Synchronous Generator Compared to Synchronous Generator (paper 2)	122
6.2.1	Introduction.....	122
6.2.2	System Modelling for SG and VSG Comparison	123
6.2.3	Simulation Results.....	129
6.2.4	Conclusion	135
7	Results and Discussion.....	137
7.1	Test Scenarios	137
7.1.1	TEST SCENARIO 1	138
7.2	TEST SCENARIO 2.....	148
7.3	Energy Storage Capacity Estimation	153
7.4	Discussion	156
8	Summary, Conclusions and Future Work	158
8.1	Summary.....	158
8.2	Conclusions	160
8.3	Future Work.....	161

Appendix A Virtual Synchronous Generator, Synchronous Generator, and PV Model Parameters.....	173
Appendix B Virtual synchronous generator control and simple dynamic machine model implemented in ATPDraw.....	177
B.1 Reactive Power Control, Governor and VSG swing equation	177
B.2 Virtual Impedance, Voltage Control and Current Control.....	177
B.3 Synchronous Generator Parameters	178
Appendix C Average model boost converter and Phase Locked Loop	180
C.1 DC/DC Boost Converter Average Model	180
C.2 Bidirectional Buck Boost Converter Average Model.....	180
C.3 Phase-Locked Loop	181
Appendix D IEEE Formal Reuse License	182

List of Tables

5.1	The Parameters of the Battery	97
6.1	The Parameters of the BESS	110
7.1	The results for Test 1	147
7.2	The result for Test 2	151
A.1	Virtual Synchronous Generator Parameters	173
A.2	Synchronous generator governor and exciter parameters	174
A.3	Synchronous generator machine parameters	175
A.4	The parameters of the KC200GT solar array at $25^{\circ}C$, $1000W/m^2$ [8] . . .	176

List of Figures

1.1	General schematic diagram of the VSG [4]	2
2.1	Cases demonstrating natural responses to small-disturbances[24]	15
2.2	Transient response of the rotor angle during the disturbance [19]	17
2.3	Phenomenon of the voltage stability for the power system simple radial system	18
2.4	Power and current as function of load for an equivalent radial system [25]	20
2.5	PV curve of voltage collapse [25]	21
2.6	Idealized model of power versus angle relationship	22
2.7	Power transfer of between two machines	23
2.8	Equal area criterion [21]	26
2.9	Stages of System Frequency Response [27]	27
2.10	Synchronous machine governor characteristic with speed droop [28]	29
3.1	Simplified dynamic structure of synchronous generator	32
3.2	Three phase salient pole synchronous generator [19]	33
3.3	Synchronous Generator Rotor and Stator Circuits [19]	34
3.4	SG reference frame voltage vector relationship	36
3.5	D-axis synchronous machine equivalent circuit	38
3.6	Q-axis synchronous machine equivalent circuit	38
3.7	Damping Control [38]	43
3.8	VSG reference frame vector and voltage complex space vector	45
3.9	Voltage Magnitude and Frequency Droop Controller	47
3.10	Droop Controller to Make Converter Behave as a Voltage Source Behind a Reactance	47
4.1	3-phase two level dc/ac VSC	50

4.2	Compute active and reactive power	52
4.3	Active power and reactive power control	53
4.4	VSC Controller Design	53
4.5	Voltage Controller of Implementation	54
4.6	The inner current loop structure	55
4.7	Active Damping Controller	56
4.8	Outer Control Loop Option	59
4.9	Block diagram of a real and reactive power in the dq -frame [18]	65
4.10	Block diagram of basic single phase PLL controller [18]	66
4.11	Schematic diagram of the SRF-PLL [18]	67
4.12	Power control loop of VSG emulation based on swing equation.	73
5.1	The schematic diagram of the power system	76
5.2	Ideal single diode PV model	77
5.3	MPPT algorithm based on P&O method	78
5.4	MPPT function based on P&O method	79
5.5	BDBBC operation modes [66]	80
5.6	The equivalent circuit for a Lithium-Ion battery [68]	81
5.7	The BDBBC operation modes[69]	82
5.8	The control scheme of the BDBBC	82
5.9	Direct axis current regulator with current reference set from power reference	83
5.10	Solar irradiation variation versus time	84
5.11	Real power for the PV, load, and battery during irradiation change	86
5.12	The SOC of the battery in response to irradiation changes	87
5.13	P_{ref} , P_{PV} and $P_{Battery}$ in response to dispatch changes	88
5.14	The SOC of the battery during P_{ref} changes	88
5.15	The Schematic Diagram of the Study Power System	91
5.16	Ideal Single Diode PV Model	92

5.17	MPPT Function Based on P&O Method	93
5.18	The P&O method algorithm	94
5.19	The Equivalent Circuit for the Battery [68]	95
5.20	Discharge Characteristics Curve of the Battery	96
5.21	(a) The BDBBC Topology (b) The control scheme of the BDBBC	98
5.22	Real power control scheme with direct axis current regulator	98
5.23	The Energy Management Algorithm (Hysteresis) for the DC/AC Converter	100
5.24	Irradiation Change	101
5.25	The Real Power of the PV, Load, and Battery During Irradiation Changes	102
5.26	Voltage at the dc Bus During Irradiation Changes	102
5.27	The SOC of the Battery	103
5.28	The Battery Current During Charging and Discharging	104
5.29	The Battery Terminal Voltage During Sequence from Figure 10	104
6.1	The schematic diagram of the power system used in this paper	108
6.2	Ideal Single Diode PV Model	109
6.3	The equivalent circuit of the battery	110
6.4	Simplified block diagram of VSG model	112
6.5	Active Power Control and Inertial Emulation Based on Swing Equation .	113
6.6	Reactive Power Control and Virtual Impedance of VSG	114
6.7	Voltage and Current Controller of VSG	115
6.8	Grid frequency decrease	116
6.9	VSG active power response	117
6.10	Response of the battery power to grid frequency change	118
6.11	Dynamic Response of Load Voltage Amplitude	118
6.12	VSG Reactive Power Response	119
6.13	VSG angular speed variations with $T_a = 5$ sec and 20 sec	120
6.14	VSG Active Power Response	120

6.15	Battery Real Power Response	121
6.16	The main circuit and control block of SG	124
6.17	The main circuit and control block of VSG	125
6.18	Reactive Power Control Loop (a) VSG (b) SG	126
6.19	Active Power Control loop of VSG	127
6.20	Active Power Control, turbine and governor	128
6.21	Comparison between SG and VSG response to an increase in real power load on the grid with change in frequency	129
6.22	Comparison between SG and VSG response to an increase in real power load on the grid with change in per unit power set point	130
6.23	Comparison between SG and VSG response to an increase in real power load on the grid with change in output power (W)	131
6.24	Comparison between SG and VSG response to an increase in reactive power load on the grid with change in voltage at point of interconnect . .	132
6.25	Comparison between SG and VSG response to an increase in reactive power load on the grid with change in delivered reactive power	133
6.26	Comparison between SG and VSG response to disturbances to different inertia time constants with frequency responses with $T_a=6$ sec	134
6.27	Comparison between SG and VSG response to disturbances at different inertia time constants with frequency responses at $T_a = 20$ sec	135
7.1	Comparing power response at PCC with $T_a = 4$ sec and $K_d=400$ following a loss of generation	139
7.2	Comparison of the system frequency response to disturbances with $T_a= 4$ sec and $k_d =400$ at different droop gains	140
7.3	The represent of equation governing the rotor motion of the VSG	141
7.4	Total power from droop term and damping term in response to disturbance with $T_a= 4$ sec and $k_d =400$	141

7.5	Comparison of (a) Battery output power under different droop gains and $T_a = 4$ sec (b) variation of the SOC of the battery when K_ω is varied . . .	142
7.6	Phase angle displacement of (a) VSG reference frame, (b) PLL reference frame	144
7.7	Comparison of the system frequency response to disturbances with $T_a = 4$ sec and $k_d = 0$ when K_ω is varied	145
7.8	Comparing power response at PCC with $T_a = 4$ sec and $K_d = 0$ following a loss of generation	146
7.9	Comparison of the system frequency response to disturbances with $T_a = 10$ sec and $k_d = 400$ at different droop gains.	148
7.10	Comparison of battery output power to disturbances with $T_a = 10$ sec and $k_d = 400$ at different droop gains	149
7.11	Comparison of the system frequency response to disturbances with $T_a = 10$ sec and $k_d = 0$ when K_ω is varied	150
7.12	Comparison of battery output power to disturbances with $T_a = 10$ sec and $k_d = 0$ when K_ω is varied	151
7.13	Virtual Kinetic Energy	153
7.14	Energy required to satisfy damping term	154
7.15	Change in energy from the battery in response to the disturbance	155
7.16	Total energy (E_{total})	156
B.1	Reactive Power Droop Control and VSG Inertia with Governor	177
B.2	Virtual Impedance, Voltage and Current Controllers of VSG implemented in ATPDraw	178
B.3	Parameters of Synchronous Generator implemented in ATPDraw	179
C.1	DC/DC converter average model implemented in ATPDraw	180
C.2	DC/DC converter average model implemented in ATPDraw	181

C.3 Schematic Diagram of the PLL implemented in ATPDraw	181
D.1 Permission from IEEE to Reproduce an Article as Chapter 5 of this Dis- sertation	183
D.2 Permission from IEEE to Reproduce an Article as Chapter 5 of this Dis- sertation	184
D.3 Permission from IEEE to Reproduce an Article as Chapter 6 of this Dis- sertation	185

Chapter 1: Introduction

In order to overcome the challenge of relying on fossil fuels, research on green energy sources can help sustain the power supply for the world. Most of the world's islands can benefit from renewable energy, as the majority of them are currently dependent on fossil fuels [1]. Renewable energy combined with power electronic control has some advantages, which includes small output impedance and fast control response of reactive power and active power. The participation of distributed energy in the frequency and voltage regulation of the distribution and transmission network is necessary in order to reduce the distributed power's impact on the networks (i.e. distribution and transmission networks). To ensure the consumption of the distributed energy by the grid, there must be a full extraction of the distributed power potential for ancillary services. The distributed power supply must also provide the possible ancillary services to the grid. Due to the numerous shortcomings of the renewable energy generation, the usage of the virtual synchronous generator control strategy is proposed. Using this strategy, the conventional rotary power and the renewable energy generation have similar grid characteristics. This makes the participation of the renewable energy in the frequency control of the power system plausible. The renewable energy can also provide ancillary services to the power grid through this means [2, 3].

Unlike conventional rotating synchronous machines, the renewable sources are not capable of providing the required amount of inertia to ensure stability of the power system. Although some renewable sources such as some wind turbines can supply a decent amount of frequency to the power grid due to its small stored kinetic energy if synchronous generator are used. In contrast, the photovoltaic (PV) sources do not have kinetic energy. However, it can supply small quantity of energy for the grid system because it has a dc capacitor located in the dc link. In addition, energy storage such as battery can work with PV sources to supply frequency control.

With increasing penetration of the power generation, there is negative influence of low inertia on the dynamic behavior and stability problem on the power grid. One solution to the instability issue of the generator is the implementation of virtual inertia. This virtual inertia can be provided through the concept of Virtual Synchronous Generator as shown in the Figure 1.1. The dynamic behavior of a synchronous generator, which is represented by its fundamental swing equation can be emulated to produce virtual inertia and can be implemented in the Virtual Synchronous Generator (VSG). The parameters of the VSG can be controlled in order to improve the system's response, unlike in a real synchronous machine [4, 5].

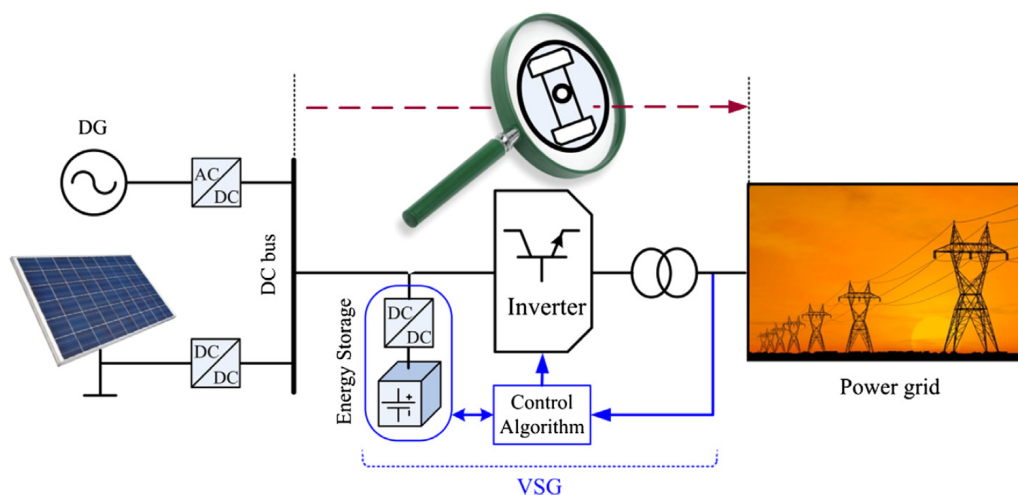


Figure 1.1: General schematic diagram of the VSG [4]

A VSG emulates the inertia response behavior of a synchronous machine in the distributed generation, specially the capability to respond to frequency deviation. The dynamic control that is provided by a VSG is able to release or absorb kinetic energy similar to the conventional generator. VSG is generally consist of renewable energy combined with stored energy, a control mechanism and an inverter. Most renewable energy sources have not inertia or damping factor. But such sources can be controlled as a SG by adding a VSG controller. The VSG emulated mass can provide the frequency droop in the grid and the dampeing support for grid oscillations. These

advantages are the electromechanically same as a SG [5]. By emulation of virtual inertia in the power system, the VSG can control of the active power in the inverter. The nominal state of charge (SOC) can be set at 50% of the capacity of ESS in the VSG. The VSG will have the ability to deliver or take power from the system. During operation of VSG depends the SOC it should be stay between 20 % and 80 % . The VSG works in the virtual active mode between these limits; otherwise, it will be work in the load mode to change the storage [6, 7].

Because of typical control algorithms that optimize real power output, power-electronic coupled generation, such as photovoltaics, are limited in their ability to supply reactive power to stabilize power system voltage and do not add to system inertia to support power system frequency. The existing power electronics can be used as voltage regulation devices, and with small additional storage, can serve as artificial inertia to stabilize system frequency [7, 8]. PV and type IV wind turbine inverters can be integrated with Flexible AC transmission system (FACTS) devices which, through their fast, flexible, and effective control capability, provide voltage stability by the injection of controllable reactive power during system disturbances [9]. Normal daytime energy flow in the system would be from the PV array to the grid via the power electronic converter operating at unity power factor to maximize revenue.

The proposed energy storage and controls allow the power electronic converter to provide voltage and frequency stability at all times by injecting reactive power and acting as synthetic inertia. Storage coupled with wind or PV generation can also make the power output of these generators dispatchable rather than directly tracking fluctuations in wind or irradiance. Additional storage can be placed on the converter DC link in PV and type IV wind turbine generation to minimize the number of additional devices needed in the system [6, 7]. According to the power flow studies, a microgrid seems to be an ideal current source that feeds power to the system. The

microgrid working in grid following mode does not have ability to work by itself during islanded mode, and it has to operate together with the power system feeding it. To keep the power system stability especially when many microgrids units are added, the calculated power algorithm that generates the current reference is dependent upon the control system performance of the microgrid, which affects the performance of the converter. Control of the grid voltage and frequency will be regulated by reactive and active power inputs.

A maximum power point tracking (MPPT) algorithm is an algorithm used to extract the maximum power from the PV array at a given instant of time. The solar irradiation is varying with time which causes changing in environment temperature and solar cell temperature which can cause the PV cell MPP to change. The converter control mechanism can track peak active power and vary reactive power to support the grid in response to disturbances such as voltage sags and load variation [8, 10].

The emulated inertia implemented in the VSG mitigates the rate of change of frequency (ROCOF) through its fast dynamic frequency response, this characteristic is especially required in a power system that is isolated, where the initial ROCOF can very high, which often results in incessant and needless triggering of protection relays [11].

Protective relays with power swing blocking function are liable to misoperation due to a lower system inertia causing more rapid power swings. This might cause out-of-step tripping malfunction due to, either changes in the swing impedance trajectory causing unwanted isolation during stable operation or the alteration in the electrical center for the swing and thus. The optimal out-of-step tripping protection location moves because of an increased proportion of wind generation. Fault response behavior differs for wind generation or PV systems compared to that of rotating synchronous machines because it depends on their converter control implementation. The impact of this characteristic on the bulk generation system has become of interest to

power system researchers. Recent studies have been performed on the performance of different protection schemes such as distance protection and negative sequence-based protection [12].

During a large disturbance in a power system, if the accelerating energy exceeds the available decelerating energy the system could lose synchronism. However, if this difference can be reversed then the response will be stable. Machines with large inertia help improve stability of this response. If energy storage is used to provide this it necessary to size it. Due to the dynamic characteristic of the VSG and the size of the worst case disturbance is unknown, the accurate size of the BESS required to maintain stability in the system cannot be determined. Nevertheless, there is some assumptions that can be used to estimate size of the BESS which are: linearization around the operating point, the mechanical input power is constant for the transient system study [2]. The amount of the storage energy needed to support the system with low rotating inertia due to combination of a large amount of the PV generation. Some researchers suggest the size of the BESS devices is to be 10 % of the distributed generation capacity [2, 4].

This dissertation focuses on a fundamental grid operational requirement to maintain stability throughout a low-inertia grid by creating artificial inertia and providing dynamic reactive power from power electronic coupled generation, such as photovoltaics and type IV wind turbines. This may offer enhancement of grid stability and can facilitate grid code compliance for wind power plants and photovoltaic (PV) [13].

1.1 Problem Description

1. Maintaining stability on a low-inertia grid is critical, but challenging.
2. Lowering inertia causes large and faster frequency changes during power unbalances
3. Creating artificial inertia and providing dynamic reactive power from power

electronic coupled generation and energy storage on the VSC DC link offer enhancement of grid stability.

4. The stabilizing capacity of artificial inertia needs to be quantified with metrics to determine ratings requirements for artificial inertia systems.

1.2 Objectives

1. Build a system and simulation of the study system using ATP/EMTP.
2. Build local control topologies to coordinate PV generation systems with energy storage and artificial inertia controls to improve frequency stability.
3. Define energy storage sizing requirements including total energy stored and available instantaneous real power.
4. Metrics for evaluating artificial inertia systems:
 - Magnitude of inertial response power (MW) available proportional to ability to influence frequency).
 - Rate of power change for inertial change.
 - Duration of inertial response (determined by energy capacity of the storage elementing).

1.3 Literature Review

As renewable energy sources such as photovoltaic and wind turbine generation become more common, there are many great challenges to implement, design and integrate them into the existing power grid without compromising system stability. Instability of power or voltage can result in major blackouts. Furthermore, conflict of deregulating the power system has reduced system stability+ due to decrease in investment in system capacity.

There are many papers showing that voltage stability can be improved by using power electronics. In addition, several discuss the impact phase angle and frequency stability control devices have in the system during system disturbances. By using FACTS devices such as (STATCOM) or (SVC) working with type IV wind turbines generation we can improve voltage stability through system disturbances such as sudden load changes or voltage sag due to faults. Based on static analysis we can recover voltage stability. STATCOM compensation can increase the steady state voltage stability margin of the power system [9],[14].

Stability of voltage has become a primary interest of the improvement of operations and planning of modern day power systems with most attention directed to understanding regional voltage collapse the sequences of events that leads to it. FACTS devices can adjust both reactive and active power flows on the system. It is more cost effective to improve quality and stability of power transmission by supplying active dynamically controlled or reactive power to the grid [15].

Voltage stability improvement has been investigated in cases with wind generation connected to the grid by using FACTS devices, using a static VAR compensator (SVC) to control voltage in the system. SVC devices can adjust voltage by injecting reactive power into the system to maintain voltage stability. System stability has been improved by using FACTS controllers. The FACTS controllers improved system stability; however, the main concern with FACTS devices is their high cost [6],[16]. The authors of [17] show stability studies for wind farm generation in Iran, which, when connected to the net grid required SVC and STATCOM, to improve power system stability. Initially the wind farms system pulled a large amount of reactive power from the grid because most of the wind turbines used induction generators. This caused voltage to be low, and affecting voltage stability when heavy load changes occurred in the distribution system [17]. The FACTS device mitigated the problems.

The references above do not use energy storage systems to provide added benefits

to increase angle and voltage stability. If we have a weak grid tie on the system or disturbances in the system from faults or voltage sags, energy storage can make help the system stable. PV and type IV wind turbine generation can work with FACTS devices to make the system stable. Another way to stabilize the weak grid frequency is to add artificial inertia to the power generation with an inertia controller implemented. It is possible to implement an additional control loop for the power electronic converter, which enable the artificial inertia control.

A lot of technical papers address the usage of energy storage to improve voltage or transient stability, most of which centers on the impact of energy storage such as flywheels, or superconductors on the power system. In one class of flywheel, the moment of inertia could be increased using a steel mass that has a large radius that could handle rotational velocities 10000 rpm and lower [15]. Distributed generation can use the stored energy or virtual rotational inertia to make the grid frequency stable. In addition, for any generation supplemented with energy storage, the virtual inertia can be integrated into the control mechanism for its power converter [14]. The authors of [5] used a method for the calculation of rotational inertia effect of renewable generator on the stability of the power system. In this case they explain that renewable energy sources such as photovoltaics and wind turbines that have been connected with inverter do not support the system with rotational inertia.

As the renewable energy resources with traditional inverters achieve high penetration, the inertia of the system is decreased. When the rotational inertia in the power system is low, the frequency dynamics are faster and it becomes challenging to control frequency and operation of the power system. Inverters for energy storage devices can support the grid with artificial inertia. Frequency control is possible if an additional control path is added, allowing an inertia response to be emulated [5],[7]. Without an additional control, the frequency support deteriorates. However when additional energy storage control is implemented, the frequency support is tremen-

dously improved. Renewable energy sources also have limitations of when and how much energy can be generated; energy storage has a significant role in helping when generation is unavailable or reduced in capacity. Energy storage systems have helped bypass the limitations of renewable energy sources. In addition, energy storage can aid regulation of frequency and transient stability and voltage support [13]. The authors in [9] introduced a new approach by using distribution static compensator (DSTATCOMs) to improve stability in the system. The converter in this approach is connected in parallel and it includes droop control to produce the needed reactive and real power. The ac capacitor bank is sized carefully to avoid low frequency oscillation.

The authors of [2, 11] implemented VSG in the weak grid incorporated into a PV Generation combined with battery energy storage to improve grid frequency improving system stability. The authors of [2] classifies that, during a big disturbance, the BESS should supply or absorb energy to prevent excessive frequency deviation. Some researchers recommended the power rating of the BESS devices to be at 10 % of the distributed generation capacity, but they did not discuss the energy requirement to improve the system frequency.

Many papers talk about improving voltage stability using FACTS devices such as STATCOM and static VAR compensator. Some papers mention using stored energy to improve stability, and they address the impact of artificial inertia on system stability and resilience when integrated into type 4 wind turbines, PV generation, and Flexible AC transmission system devices to support a weak grid. During the disturbances, the phenomenon of providing or absorbing energy system is explained by the conventional swing equation to calculate the required power from the amount of stored energy needed to support the transient stability in the system.

Due to the costs associated with the implementation of the energy storage, it is important to develop innovative services that would aid the stability of the system frequency. In this regard, a lot of research questions have come up over the past

few years. Considering several historical frequency data analysis [4] and [18], this dissertation aims to address some of these questions, which include:

- How fast should the ESS be allowed to discharge or charge to avoid decreasing the lifespan of the battery?
- What should the SOC be at which the ESS is not operate at when providing or absorbing power in order to improve the lifespan of the energy storage?

This dissertation describes an approach for sizing the battery based on the required power transfer. The contribution of energy storage system to emulate inertia to improve system stability is described. Simulations were conducted on 9-bus test system with PV integration to highlight the effectiveness of this approach. The battery size required for appropriate inertia response was validated by transient simulations and the result obtained from this study is presented in this chapter.

The research question which needs to be quantifiably answered is: "Does adding artificial inertia with energy storage such as batteries, flywheels, or superconducting magnetic energy storage actually improve system stability?" Methods to show how well artificial inertia improves system stability when power system disturbances occur are needed. Another concern is how much artificial inertia will be added to make the system stable, and what are the power and energy rating of the battery energy storage system for grid inertial response?

Chapter 2: Power System Stability: An Overview

This chapter reviews the power system definitions as used in this dissertation. The first section explains the phenomena of power system stability. Voltage stability is discussed in the following section. Finally, the last two sections elaborate the power versus angle relationship including the main features of the swing equation and the equal area criteria. Frequency response to grid disturbances including the definition of inertia response and frequency response during disturbances will be discussed in the concluding sections.

2.1 Power System Operation and Stability

2.1.1 Introduction

An important point of concern in power system stability is the stability of the response to a transient disturbance in the system. The equilibrium point under steady-state occurs when the input mechanical torque and output of the electric torque of each machine are equal if losses are ignored and the rotor speed is constant. The steady-state balance is disturbed if unbalanced behavior occurs in the power system, which causes the rotors to decelerate or accelerate, which can be represented using the swing equation. When a large disturbance occurs the generator angle and possibly its frequency varies with respect to the system. If the generator breaker is open due to a fault, it could lose synchronism with the system prior to re-closing. This condition causes abnormal current or voltage and a change in frequency with respect to the system fundamental frequency for that generator[19]. If such generator is not re-synchronized or removed from the system immediately it can cause instability of the power system, sometimes a local blackout. As a result, the generator controller will observe this speed difference and bring the generator speed to the synchronous speed for power angle stability [20].

The stability of the power system is related to the torque for each synchronous machine. When there is not enough synchronizing torque, this can lead to power system instability through an aperiodic drift in the rotor angle's. Also, decreasing the damping torque can lead to power system oscillatory instability [21].

The voltage transients may appear on a power system for a few second but if corrective action are not taken, may cause damage to equipment and impact system operation. Some voltage transients may appear after a specific system operation state or disturbance, which can be predicted through detailed study of transient voltage stability of the power system to determine corrective actions [22].

Further, maintaining steady-state system stability is also very important for power system operation. The load on a power system is always varying in real-time, as does the output of some forms of renewable generation and these variation need to be balanced by available generation. The balance between electrical and mechanical power for an individual machine should be maintained. When the speed of the rotor runs higher or lower than the system operating frequency, this could lead to loss of synchronism and the machine will be detached from the power system. The slip between the stator rotating field and the rotor field can leads to high disturbances in the output power of the generators. If the protection device measures a slip more than a threshold value, it will trip an unstable generator from the power grid [20, 22]. The power system should be modeled, and simulated to maintain ensure stable voltage and frequency response for small disturbances.

2.1.2 Definition of Power Stability

Power system stability refers to the ability of the system to maintain operational equilibrium in steady-state and recover stability after a disturbance affects to the system. The major problem associated to the security of the system's operation was recognized in 1920s as power system stability. Unstable response of the power system

produces many problems and in extreme cases blackouts. As a result, an important concern in system operation is ensuring that the system operates at a stable point[22].

The Most challenging situation for maintaining stability in the power grid is when a large generator disconnects unexpectedly and a large disturbances occurs. Fast change in photovoltaic or wind generator output for large facilities can also create problems. To make the power system more stable, operators need to plan for those situations during the design and specification of devices connected to the grid. Events such as loss of large generators, sudden demand or loss of several critical lines at once can cause blackout or even damage equipment connected to the grid. If operators take have tools to mitigate disturbances it is possible to have much more stable power system [20, 23].

The power system is extremely complex As the load and generation are changing continuously dispatchable generation responds to maintain balance. Modern power systems require more complex controllers to maintain balance between load and generation. An equilibrium boundary must be maintained between generation and load requirements to keep the power system balanced. In addition the power system should also have proper protection schemes to recover its point of stability following major events[23].

Due to the improvements in distributed control and communication systems and automation, modern power systems are more stable, secure and reliable. However challenges with retirements of conventional generator replaced with inverter based generation risks this accomplishment:

- Conventional power plants are controlled since their fuel can be stored or consumed based on system requirements, unlike the renewable sources that depend on the weather. These conditions result in rapidly variable generation, which are not easily controllable.
- The response of the synchronous generators to disturbances is different from

the power electronically controlled renewable energy. The power electronic controllers show different behavior in response to disturbances and try to maintain constant power output as a first priority to maximize revenue.

- HVDC transmission can be controlled rapidly. Power flow can also modulated to damp power swings [23].

2.1.3 Power Angle Stability Classification

When analyzing power system stability, there are two phenomenon that should be taken into consideration pertaining to rotor angle stability: small-disturbance system phenomena and transient stability [23].

2.1.3.1

Small-disturbance refers to small perturbation from system's initial operating point under minor disturbances of the system. These small disturbances results from minute changes in the load and power system generation. The response of the power system for the small disturbances depends on the generators inertia, strength of the power transmission system, and response of the generator power excitation controls [24].

The power system disturbances are regarded to be small enough for that the system equations can be linearized the purpose of the angle stability analysis. The power system angle stability depends upon, first an increase in the steady-state angle of the rotor results from lowering of the torque synchronizing and second the damping torque proportional to the speed deviation [19] and [24]. The small signal response of a conventional power system can be classified using the cases in Figure 2.1.

- Case 1: If both the steady-state angle of the rotor and damping torque are positive then stable operation is maintained.

- Case 2: For a generator with constant field voltage having a radial connection to a huge power system, insufficient synchronizing torque results in instability.
- Case 3: For a case with a lack of damping torque, growing oscillations will occur which also causes instability.

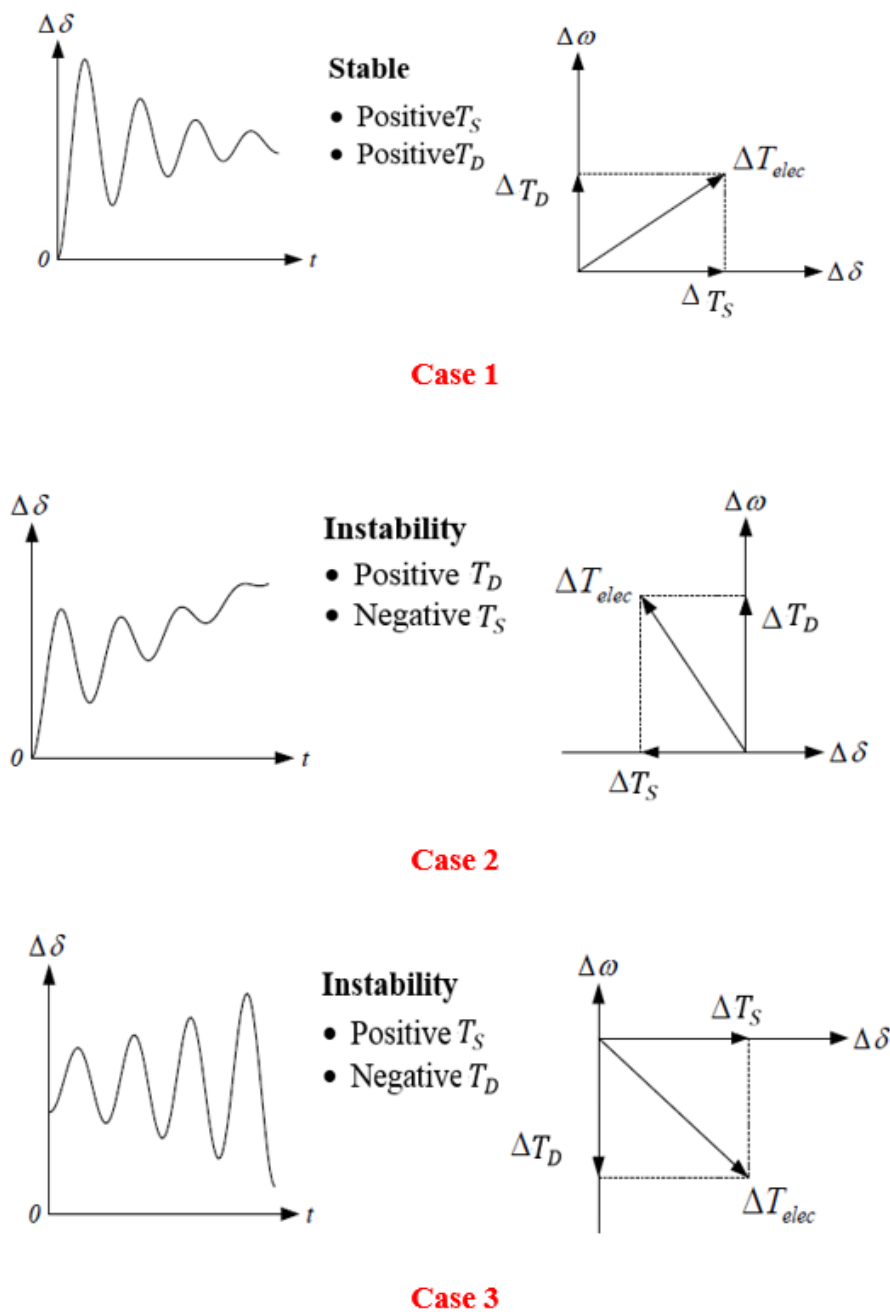


Figure 2.1: Cases demonstrating natural responses to small-disturbances[24]

When large disturbances are taken into consideration, the impact factors include large currents, large torque values, and deviations of rotor angle, where the outcome is dependent on the power system's nonlinear behavior. However, the smaller disturbance behaviour in power signals can also eventually lead to large oscillations towards power system instability [19] and [20].

2.1.3.2

One type of major disturbance analysis is transient stability analysis which refers to the ability of the system to recover equilibrium condition after heavy transient situation in the power system. The ability of the power system to sustain synchronism depends upon its capacity to stabilize the transients. There are two main factors for transient stability; initial operation conditions and amplitude and duration of transient disturbances. The system response to a large transient involves large generator rotor angle swing and follows a nonlinear power angle relationship. The large disturbances on the power system are caused by short circuits resulting in tripping of critical lines. The modeling for system stability can include a three phase fault or a fault associated with a transformer. The protection scheme should be configured to respond to each fault according to its type and location. If the breaker response is too slow an unstable response is more likely. But most faults have minimal stability risk [25].

Figure 2.2 illustrated how transients may appear for few seconds on a power system and can cause huge disturbance due to oscillation. There are three contingencies discussed in the figure to compare the system response on each scenario. In a stable response, the rotor angle increases until breaker action occurs and then oscillation, where amplitude decreases and stabilizes when it reaches a new steady state. There are two scenarios for instability, in the first instability scenario the rotor angle changes relative to a reference and continues to diverge. For the second instability scenario, the

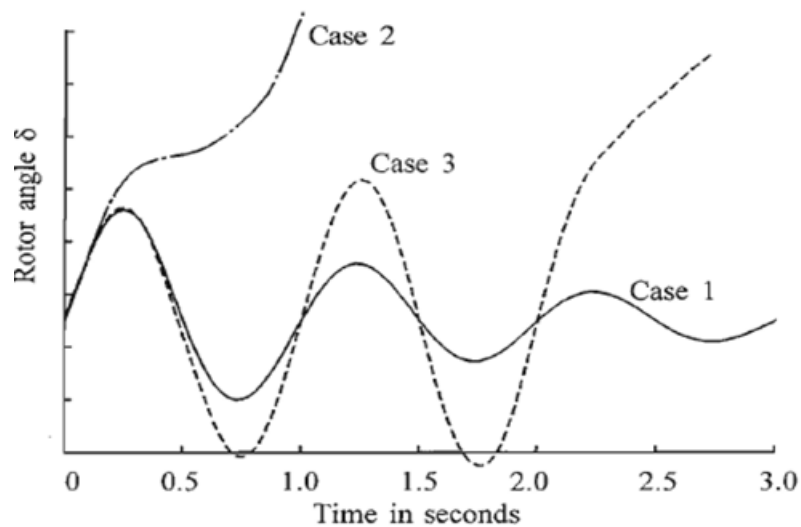


Figure 2.2: Transient response of the rotor angle during the disturbance [19]

rotor angle is not stable, the first swing does not blow up, but the resulting oscillations have negative damping. This nonlinear response may be due to interactions between generators and their controls in the system [20] and [23].

2.1.4 Voltage Stability

Voltage stability denotes the ability of power system to maintain the voltage at all buses acceptable level after disturbance happens in the grid. Voltage stability depends on the capability of the power system to recover the equilibrium between reactive power supply and demand. However, instability is generally increased in the system by the magnitude of the voltage oscillation. In addition, voltage instability may happen when there is disturbance that lead the voltage increase or decrease at some of the buses. The result from voltage instability is loss of some loads in the area or possibly voltage collapse in response faults or large generators that have tripped in response to disturbance.

Voltage instability generally occur on the power system which are connecting large loads, power system faults, starting motors and energizing transformers can cause

voltage instability. In addition, voltage drop occurs in the transmission network when the large reactive and active power flow through the inductive line reactance causes a decrease in performance of the transmission network [19], [20] and [22].

Voltage sags are generally short duration events which occurs when a large load is connected, transformers are energized or due to power grid faults. Voltage sags are large in magnitude and short in duration. The steady state of voltage sag impacts on system voltage stability should include components such as Line-commutated converters (LCC) HVDC converters and induction motors [24].

Voltage collapses are usually long duration events, associated with failures in the power system. These collapses occur when the total load is too large, large load are suddenly connected, faulted, or when there is insufficient reactive power. Local voltage sags are not too harmful for the system as they can be compensated by switching inductors or capacitors, while the system-wide voltage collapse can damage power system equipment in severe cases [19] and [22]. Voltage stability is impacted by the system impedances, fundamentally the source, line and load combined. A voltage instability can occur when a sudden change in impedance is added to the system leading to an unstable steady-state, as shown in Figure 2.3.

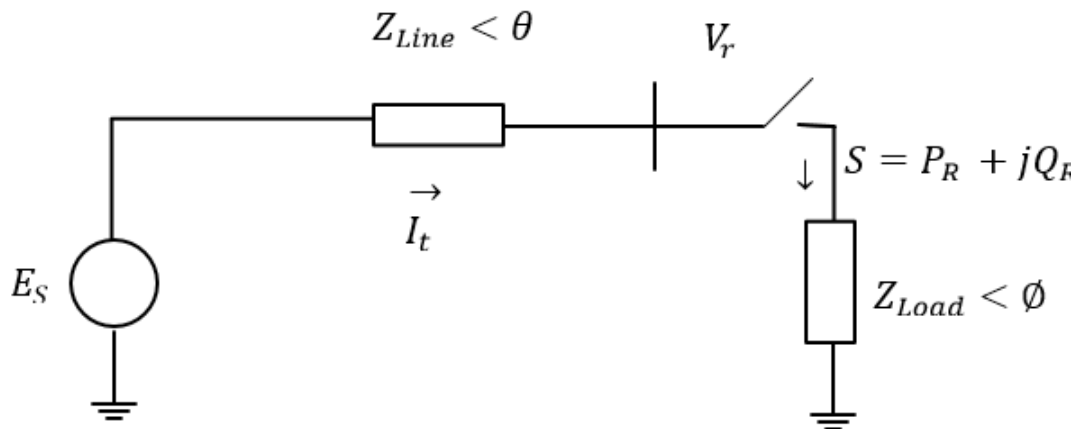


Figure 2.3: Phenomenon of the voltage stability for the power system simple radial system

The magnitude of the current, I_t , given by the equation (2.1):

$$|I_t| = \frac{E_s}{\sqrt{(Z_{Line} \cdot \cos\theta + Z_{Load} \cdot \cos\phi)^2 + (Z_{Line} \cdot \sin\theta + Z_{Load} \cdot \sin\phi)^2}} \quad (2.1)$$

Where Z_{Load} is the impedance magnitude of the load.

\vec{E}_s is the voltage source equivalent behind the impedance.

\vec{Z}_{Line} the impedance of the transmission line.

Equation (2.1) can be re-written as

$$I_t = \frac{E_s}{Z_{Line} \sqrt{F_L}} \quad (2.2)$$

where the F_L

$$F_L = 1 + \left(\frac{Z_{Load}}{Z_{Line}}\right)^2 + 2\left(\frac{Z_{Load}}{Z_{Line}}\right)\cos(\theta - \phi) \quad (2.3)$$

The voltage magnitude at the load can be represented by the following equation:

$$V_r = Z_{Load} \cdot I_t = \frac{1}{\sqrt{F_L}} \frac{Z_{Load}}{Z_{Line}} \cdot E_s \quad (2.4)$$

The real power provided to the load (P_{load}) is given in equation (2.4)

$$P_R = V \cdot I_t \cdot \cos\phi = \frac{Z_{Load}}{F_L} \left(\frac{E_s}{Z_{Line}}\right)^2 \cdot \cos\phi \quad (2.5)$$

From the Figure 2.4, the power transfer to the load relative to maximum power, P_{max} , to the 0.8pu voltage source and start increasing slowly up to 1pu. The 1pu voltage source point is the maximum power transfer point as the ratio of line impedance to the load impedance is 1. If the load impedance starts decreasing relative to line impedance, the power transfer starts decreasing.

Power transmission is analyzed by studying the current transferred along lines and the voltages at the ends of the lines. The PV curves for a load bus in radial system power system is shown in Figure 2.5. The relationship between the power and

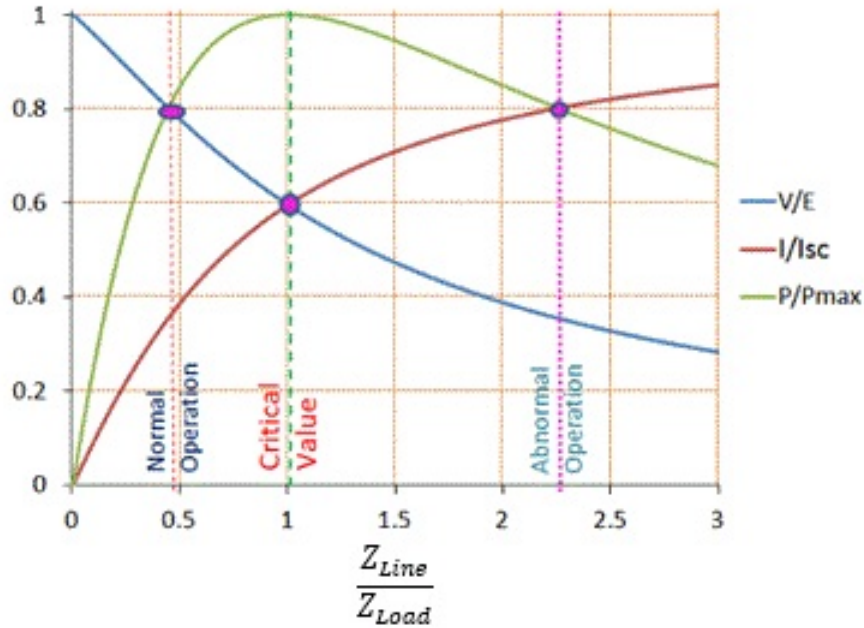


Figure 2.4: Power and current as function of load for an equivalent radial system [25]

voltage is a quadratic function. The normal range on top part of the curve shows that active power can be increase at expense of small decrease in voltage magnitude. The uppermost voltage curve in the graph is the normal operating range. In this region, a decrease in power transfer increases voltage with a stable response. The lower value of voltage at same power level is an unstable point, where voltage falls as load decreases, and most loads draw less power when voltage falls. The system voltage stability limit defines, the maximum power transfer that is defined as the lose of curve. The other factor that can change our system stability curve is the line impedance. The change in line impedance can significantly change the maximum power that can be transmitted as shown by comparing the two curves in Figure 2.5 [26].

In addition, if a fault occurs in the transmission line when it is operating close to its limit, the fault can affect the system in such a way that the maximum power transfer point is lower the Pre-fault power transmission [24] and [26]. This also influences the load recovery of the system following a disturbance.

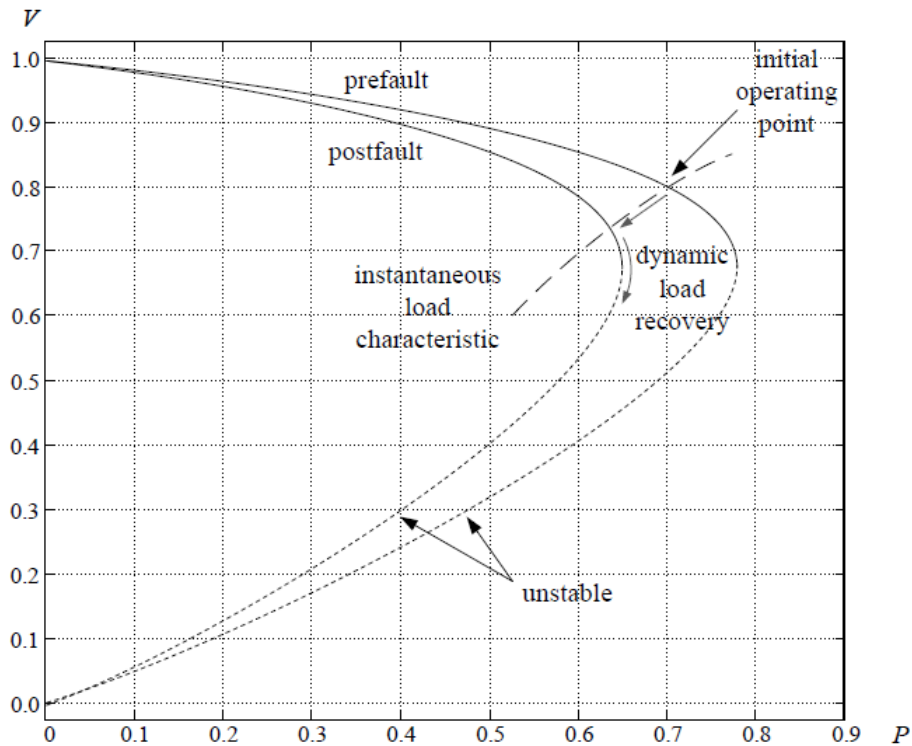


Figure 2.5: PV curve of voltage collapse [25]

The components that enhance the voltage stability require adequate modeling for analysis. These components include capacitor banks, protection, control of secondary frequency, and Flexible Alternating Current Transmission Systems (FACTS) devices [24].

2.2 Dynamic Power Versus Angle Relationships

Power system transient instability happens when there is sudden disturbance in the system such as the disconnection of large generator from the system. Such disturbances lead to large changes in the grid's power flow. Due to the inertia effect, the angle of the rotor does not change instantaneously and exhibits oscillatory behaviour. During the power disturbance, the kinetic energy that is stored in the rotating mass of the synchronous generator cannot be released instantly at the moment the disturbance happens in the system [20] and [23].

The relationship between the active power and angular position is an important characteristic in the stability of the power system rotor angle response. This relation of the rotor angle of the synchronous generator is nonlinear. To explain this, let us consider two synchronous machines that are connected through a transmission line. This transmission line has only an inductive reactance (X_L), ignoring both capacitance and resistance. In addition, consider machine 1 is generator and machine 2 is motor. This power is related to the rotor angular difference between these machines (δ). Figure 2.6 shows, per phase equivalent model where each machine has an internal voltage behind a reactance. The steady-state reactances for the generator is X_G and the motor is X_M . The voltages E_G and E_M depend on the machine excitation [20]. The power transferred P_e from generator to the motor is given by equation (2.6):

$$P_e = \frac{E_G \cdot E_M}{X_T} \cdot \sin \delta \quad (2.6)$$

where the X_T

$$X_T = X_G + X_L + X_M \quad (2.7)$$

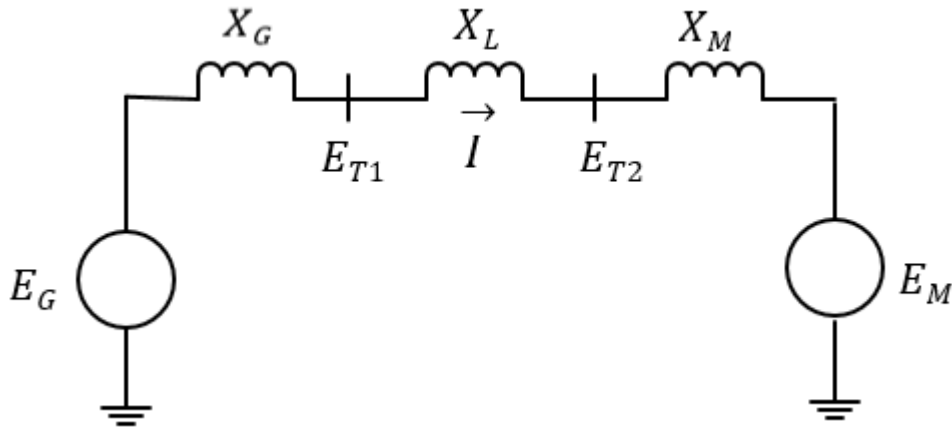


Figure 2.6: Idealized model of power versus angle relationship

Equation 2.6 can be plotted as a power versus angle graph as shown in the Figure

2.7. Initially of P_e is equal zero, as the angle is zero. As the angle increases, the P_e increases until this angle equals 90 degree. The maximum power can be transferred between these machines as that excitation level with an angle different of 90 degree. Any further increase in the angle after 90 degrees leads to decrease in the power transfer[20]. When the angle become 180 degree then the magnitude of power transfer equals zero as shown in the Figure 2.7.

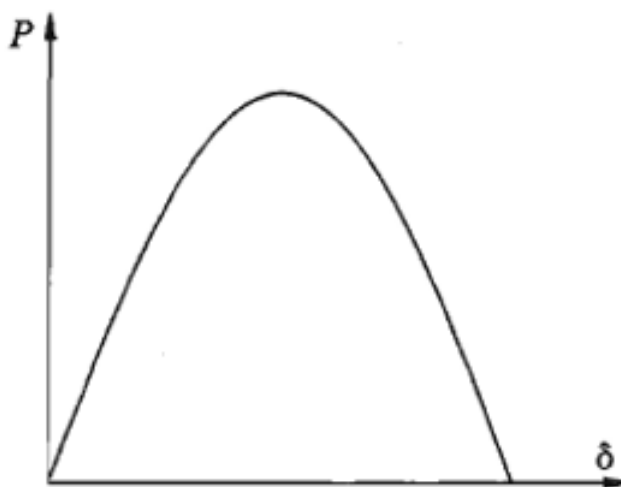


Figure 2.7: Power transfer of between two machines

2.2.1 Swing Equation

The curve in 2.7 is a static relationship. The swing equation describes the dynamic relationship between rotor angle with respect to the time and the electromechanical behaviour of the machine. This equation is important in the analysis of the single machine stability and can be expanded to look at system-wide stability. Let us start with a three-phase synchronous generator which runs at certain mechanical power operation point form its prime mover. The prime mover in the synchronous machine transfers the mechanical torque to the shaft. The rotor produces an electromagnetic torque from the shaft's mechanical torque which leads to electric power transfer. In

the synchronous generator analysis in this thesis, the losses due to friction, windage and core losses are ignored [21], [22] and [27]. The mechanical and electric torques for the generator are positive, the motion of the rotor is defined by Newton's second law of motion, in equations (2.8), (2.9) and (2.10)

$$J\alpha_m(t) = T_m(t) - T_e(t) = T_a(t) \quad (2.8)$$

$$\alpha_m(t) = \frac{d\omega_m(t)}{dt} = \frac{d^2\theta_m(t)}{dt^2} \quad (2.9)$$

$$\omega_m(t) = \frac{d\theta_m(t)}{dt} \quad (2.10)$$

Where J is total moment of inertia of all of the masses on the rotor shaft $Kg - m^2$ $T_m(t)$ is mechanical torque provided by prime mover in Newton meters ($N - m$). $T_e(t)$ is electrical torque related to the three phase output power of the generator including the electric losses ($N - m$).

$T_a(t)$ is accelerating torque, the difference between T_m and T_e ($N - m$).

$\alpha_m(t)$ is angular acceleration of rotor (rad/s^2).

$\omega_m(t)$ is velocity of rotor angle in (rad/s).

$\theta_m(t)$ is rotor mechanical angle is respect with fixed reference (rad).

T_m and T_e are equal in steady-state so T_a is zero. When the T_a is positive the α_m will be positive the rotor will accelerate, this true when T_e is less than T_m . On the other hand, the rotor speed decreases when the T_e is greater than T_m .

The angular position of rotor is measured with respect to the synchronously rotating reference axis of the rotor relative to the terminals or an arbitrary reference point, as defined in equation (2.11):

$$\theta_m(t) = \omega_{msyn}(t) + \delta_m(t) \quad (2.11)$$

Where $\delta_m(t)$ is the position of rotor angular (rad).

$\omega_{msyn}(t)$ is synchronous angular velocity of the rotor angular, *rad/s*.

Substituting equations (2.11), (2.10) and (2.9) into (2.8) lead to:

$$J \frac{d^2 \theta_m(t)}{dt^2} = \frac{d^2 \delta_m(t)}{dt^2} = T_m(t) - T_e(t) = T_a(t) \quad (2.12)$$

Equation (2.12) can be simplified by converting the actual values to per unit by dividing this equation by rated apparent power (S_{rated}) of the generator. The resulting equation include a damping term (D) is:

$$\frac{2H}{\omega_{syn} \cdot \omega_{pu}(t)} \cdot \frac{d^2 \delta_m(t)}{dt^2} = P_{m.pu}(t) - P_{epu}(t) - \frac{D}{\omega_{msyn} \cdot \frac{d\omega_m(t)}{dt}} = P_{apu}(t) \quad (2.13)$$

Where $P_{epu}(t)$ is electrical power output in pu, $P_{mpu}(t)$ is the supplied mechanical power in pu. H is constant which relates kinetic energy stored as $1/2 J \omega_{msyn}^2$ to the generator MVA rating (S_{rated}). The value of H is typically between [1-10] p.u.-s. D is a damping factor and is fairly small between [0-2]. The constants D and H are typically provided with generator data.

2.2.2 Equal Area Criterion

Consider equation (2.13) for a machine connected to the infinite bus. Figure 2.8 shows the relation between the electric power and mechanical power with the power system angle from equation (2.6) in response to a disturbance [21]. In prefault steady-state operation, assume the initial rotor angle is $\delta = \delta_0$, $P_m = P_{m0}$, and $P_e = P_{e0}$. The mechanical power has a step change from P_{m0} to P_{m1} , δ increases δ_0 until it is equal to δ_1 the rotor accelerates following (2.13) until electric and mechanical power become $P_{m1} = P_e$ and $\frac{d^2 \delta_m(t)}{dt^2}$ becomes zero. However, the response will still increase to exceed δ_1 where P_e is higher than P_m . This result leads to accelerating power P_a and the

rotor decelerates until eventually δ reaches a maximum of δ_2 at which the rotor angle swings back to δ_1 . It will oscillate back and forth until it settles at δ_1 .

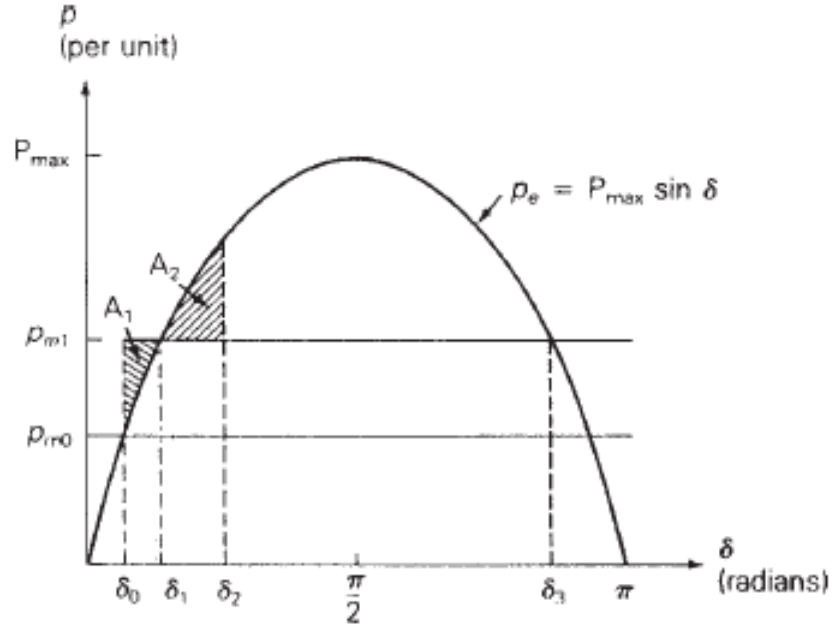


Figure 2.8: Equal area criterion [21]

As shown in the Figure 2.8, there are two areas highlighted. First area is A1 is accelerating area and located between P_m and P_e . Second area A2 is decelerating area which is located at $P_m < P_e$ and $\delta_1 < \delta < \delta_2$. The accelerating area is bounded by the extent that δ and P_e vary.

Power system first swing instability can be described using the equal area criterion as a case where the power angle reaches and passes δ_3 in Figure 2.8. It is the result of A1 exceeding the available decelerating area A2. However, a stable swing occurs when the A1 equals A2 and the available A2 is bounded by δ_3 . It can be concluded from the above discussion that A1 represents to energy added due to acceleration of the rotor, while A2 is to the energy lost through the deceleration.

2.3 Frequency Response Following a Grid Disturbance

It is important to keep the frequency stable in the power system to ensure system stability. Maintaining stability of frequency after a disturbance or unbalance in the power system between the power generation and the grid load is measured by the ability of the frequency to return to steady-state following the power swing. Other factors that affect the power system frequency include the response of the equipment controls and protection response. The system response for a system dominated by synchronous machines can be divided into four stages: Inertia Response, Primary Frequency Response, Secondary Frequency Response and Tertiary Frequency Response as shown in the Figure 2.9 [22] and [27]. Human operators response comes into play in the secondary response and is key to the tertiary response.

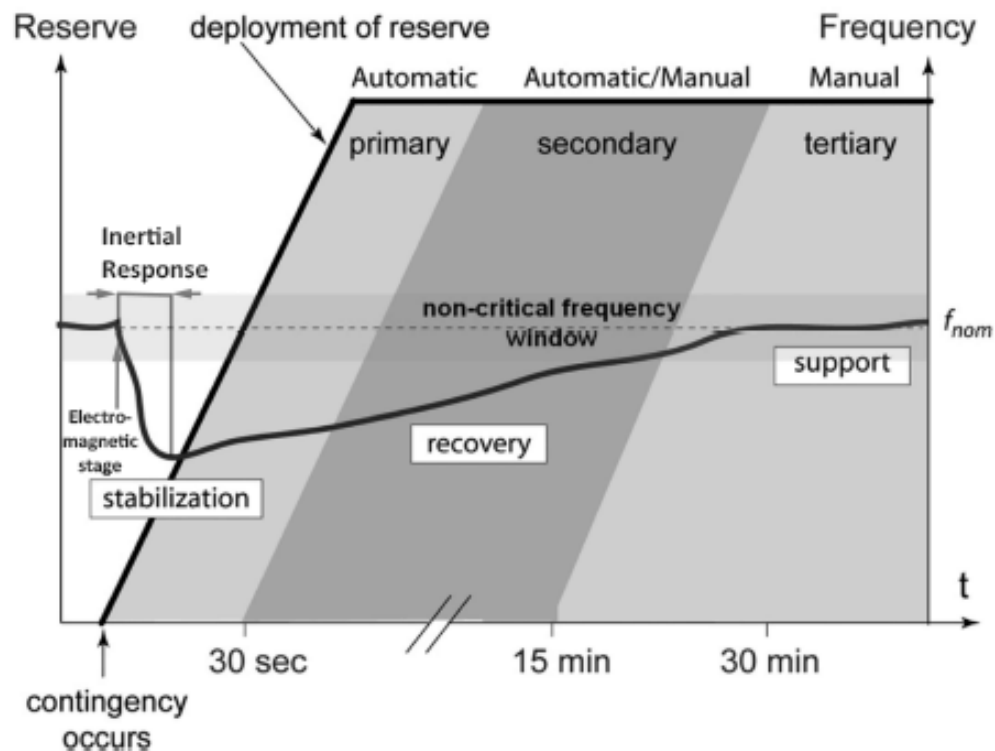


Figure 2.9: Stages of System Frequency Response [27]

2.3.1 Machine Inertia Response

After the electromagnetic response to the disturbance, the response of cumulative inertia of the system is part of the electromechanical system frequency response. This stage occurs in the initial swing of the rotor and oscillatory response is occurring in the electrical and mechanical outputs. In this stage, the stored kinetic energy starts to dissipate and the synchronous generators slow due to caused a frequency decay due to the increase in the difference between the electrical output and mechanical input. These variations do not make the angle of the bus voltage vary suddenly, but do lead to an adjustment of the equilibrium points for each power generator. The electrical power variation is related to the amount of the inertia and is measured as the rate of change of speed $\frac{d\omega}{dt}$. This can lead to an increase or decrease in the power frequency depending on the triggering event. The higher the rotating inertia of a system, the slower the rate of change of the frequency (ROCOF) and the more likely the response is to be stable. A fast ROCOF can result in the system varying faster than the actual load control response leading to loss of stability. Hence, power frequency stability is easier to maintain large inertia, which enables the primary frequency control equipment to operate in within their response parameters [27] and [28].

2.3.2 Response of primary frequency control devices

The machine inertia affects the rate and magnitude of frequency deviation the power system in response to events. When this deviation is out of dead band shown in the Figure 2.10, the primary controller responds between 20-30 seconds and to stop the drop or rise in the power frequency measured at the generator by generator output power. The feedback control for the frequency response of each machines keep the power system stable. Therefore the deficit in power is covered by the combined

governor action [29]. Figure 2.10 shows a typical governor characteristic with droop in the speed control. A primary frequency controller keeps the frequency oscillation Central near the initial steady state (f_{ss}) following a the system disturbance. But, there is a difference between the re-established frequency and normal frequency (f_0) due to the droop response $\Delta f_{ss} = f_0 - f_{ss}$. This primary frequency controller with droop control is able to reduce oscillations, but cannot recover the frequency to its original value, which is instead provided through use a secondary frequency response [28]. The response times of these controls are generally in the range of seconds due to mechanical system limitations.

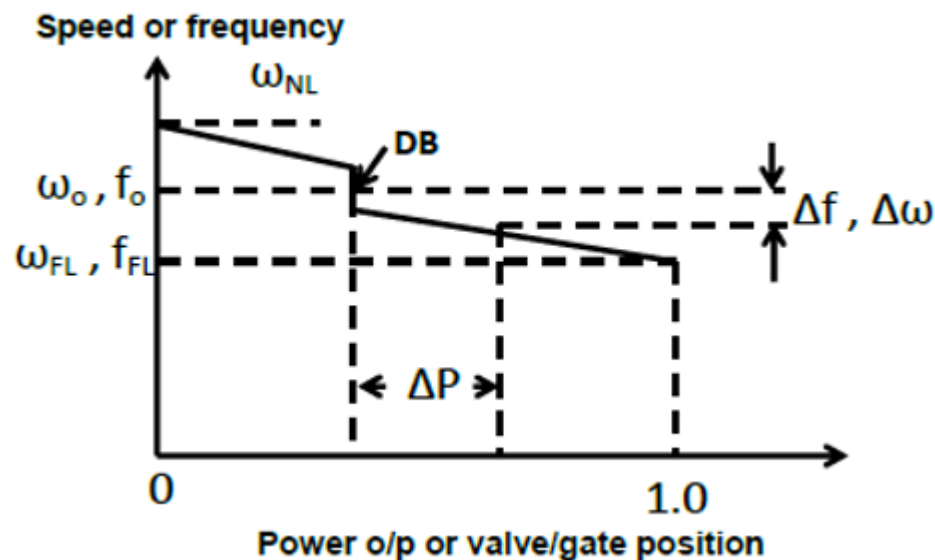


Figure 2.10: Synchronous machine governor characteristic with speed droop [28]

Where:

Rated speed at the nominal condition ω_0, f_0 .

Full load speed ω_{FL}, f_{FL} .

No load speed ω_{NL} .

2.3.3 Response of secondary frequency

This stage of response is used to reduce the steady state error Δf_{ss} due to the response of the primary frequency control. In addition, the response of the secondary frequency includes emergency reserve, which is usually an action that is centrally coordinated. Based on the operator's need, the speed droop point of the generators is varied in the secondary control. This is achieved by altering the prime mover's load reference which is used in the compensation of the load changes. In this stage, the response rate of the frequency is lower than primary frequency response. The system frequency can recovery to the rated value between 30 seconds to 30 minutes as shown in the Figure 2.9.

2.3.4 Response of tertiary frequency

In order to balance generation and load, tertiary frequency control operates over a balancing interval of 15 to 30 minutes (depending on the rules of local jurisdiction) [23] and [28].

Chapter 3: Matching Response of a Synchronous Machine and a Virtual Synchronous Disturbances

This chapter consists of two sections that present two of the main ideas in this dissertation. The first section presents the theoretical and practical background of modeling synchronous machines including some assumptions that are made in this work. The second section discusses the concept of creating a virtual synchronous machine with virtual inertia including droop and damping control and matches that response to the synchronous generator.

3.1 Introduction

Many electric energy sources are connected to a power system to fulfill the basic load requirement. A major fraction of this power is supplied through synchronous machines. Synchronous generators are used to produce an electric energy by converting mechanical energy from gas turbines, steam turbines and hydro turbines [20].

The block diagram in Figure 3.1 models a synchronous generator (SG) which consists of two dynamic parts: an electrical part and a mechanical part. The diagram shows that the first stage in the operation process burns fossil fuel to generate the required steam. This resultant steam creates the movement of the turbine, which in turn turns the rotor of the generator. Most generators installed in an electric power network are SGs. A SG converts the delivered mechanical power from the steam turbine to electrical power that will be supplied to the loads through the network [30].

3.2 Synchronous machine (background)

The major parts of a synchronous generator are the stator and rotor. The stator has a stationary armature winding, which is electrically connected to the electric system,

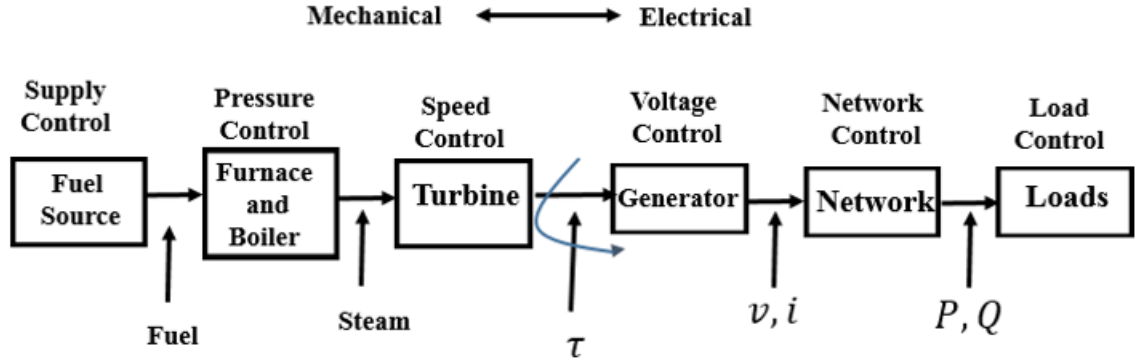


Figure 3.1: Simplified dynamic structure of synchronous generator

while the rotor is made up of an electromagnet used to produce a rotating magnetic field. In order to enhance and control the strength of the magnetic field in the rotor, DC current is applied to the rotor winding in the SG. A 3-phase voltage is induced in the stator winding due to the rotation of the rotor field [19] and [22].

As noted above, the field winding induces AC voltage in the armature winding through use of a DC current to produce a magnetic field. More space is required for the insulation of the armature winding due to the fact that it operates at a much higher voltage than the field windings. In addition, the armature winding requires ample mechanical strength because they are usually exposed to high currents. As a result of these factors, placing the armature winding on the stator is the desired practice a high MVA ac machine as shown in the Figure 3.2 [20] and [29].

Since the armature experiences a fluctuating magnetic flux, thin laminations are used to build the stator iron to minimize eddy current losses. When generating balanced three-phase currents, the magnetic field created in the air-gap by the armature current will rotate at synchronous speed. The DC current in the rotor produces a field that revolves with the rotor. When the rotor and stator fields both rotate at the same speed, they generate a steady torque. The rotor must therefore spin at a synchronous speed of $(N = \frac{120f}{P})$. Where the N is the synchronous speed, f is the

frequency and P is the number of poles. Depending on the speed, there are two commonly used structures for the rotor. The first option is a salient pole rotor, which is often used in slower speed rotors, such as those of hydro turbines. The second option is a cylindrical rotor design this is used in steam and gas turbines that work at high velocities [19]. Figure 3.2 shows as salient pole rotor with two poles.

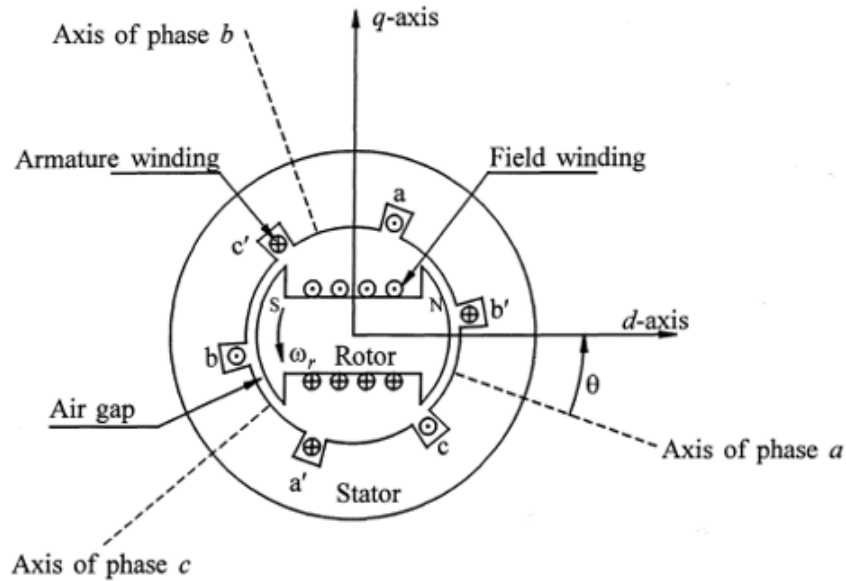


Figure 3.2: Three phase salient pole synchronous generator [19]

3.2.1 Synchronous generator assumptions

There are some assumptions used in the mathematical modeling and analysis of the SGs that arise from the machine design. Voltages are assumed to be balanced and sinusoidal. The current is also assumed to be balanced and sinusoidal for steady state operation. The inductance of the stator is constant and the stator winding is distributed sinusoidally along the air-gap. For the purposes of the research, the damper winding on the rotor is included and only one pair of poles is assumed. The effects of hysteresis, saturation, and eddy currents are neglected. The equations of the machine are derived with the assumption that the relationship of the flux-current

and all the circuit couplings are linear[20] and [30].

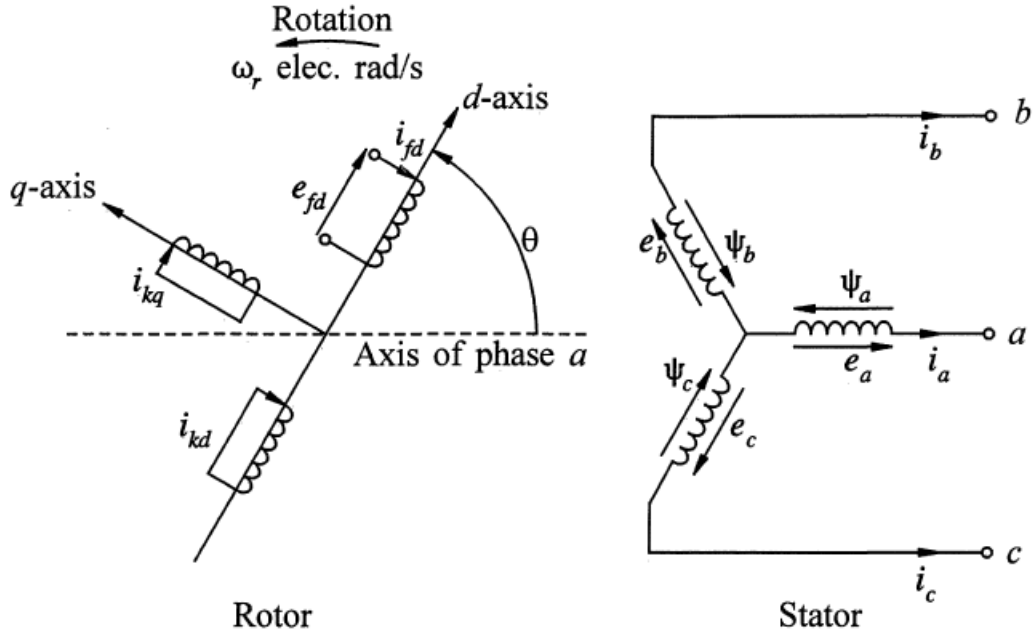


Figure 3.3: Synchronous Generator Rotor and Stator Circuits [19]

Figure 3.3 shows the stator and the rotor models used in this section. The geometry of stator windings contains a 3-phase armature winding [a, b and c] carrying ac current, and a rotor circuit with a dc input and includes the affected rotation of the machine. When the rotor is rotating, it produces a magnetic field that induces voltage in the stator winding. In addition, the rotor includes damper windings [d, q] and a field winding f_d which is connected to the DC current source [22], [29] and [30]. The current flow in the amortisseur circuit (damper winding) can be represented by two sets of closed circuits. In the first set of closed circuits, the flux is along the direct axis (d-axis) which is aligned with with the field axis flux. In the second set, the flux is along quadrature (q-axis) or at a right angle to the field axis.

Figure 3.2 and Figure 3.3 show the SG rotor angle θ is between the d-axis and center-line magnetic axis of phase A. The rotation direction of the d-axis leads the phase A winding. When the SG rotor starts to rotate with respect to the stator, then θ increases at a constant rate. The relationship between θ , rotor angular velocity ω_r ,

and the time (t) is defined in equation (3.1):

$$\theta_{sm} = \omega_r \times t \quad (3.1)$$

where θ is the angle between the phase a axis and the d-axis measured in electrical radians (rad) and ω_r is measured in electrical radians per second (rad/s).

There is also another assumption in the polarity of the conventional generator; the polarity is assumed to be positive when the direction of the current stator winding is flowing out of the machine and when the current in the field winding flowing into the machine [20], [29] and [30].

To simplify analysis, the Park's transformation is used to convert quantities from the stationary abc reference frame to rotating $dq0$ reference frame. The transformation takes the angle as an input and uses it as a reference [20]. The matrix transformation from abc phase variables to $dq0$ variables are defined in equation (3.2):

$$\begin{bmatrix} i_d \\ i_q \\ i_0 \end{bmatrix} = \frac{2}{3} \begin{bmatrix} \cos\theta & \cos(\theta - \frac{2\pi}{3}) & \cos(\theta + \frac{2\pi}{3}) \\ \sin\theta & -\sin(\theta - \frac{2\pi}{3}) & -\sin(\theta + \frac{2\pi}{3}) \\ \frac{1}{2} & \frac{1}{2} & \frac{1}{2} \end{bmatrix} \begin{bmatrix} i_a \\ i_b \\ i_c \end{bmatrix} \quad (3.2)$$

The constant can be $\sqrt{\frac{2}{3}}$ or $\frac{2}{3}$ [20].

3.2.2 Reference frame orientation of SG

The SG orientated Synchronous Reference Frame (SRF) rotates at the angular speed of the voltage at the grid in steady state. Therefore, the rotor phase angle θ_{SG} as indicated in the Figure 3.4 is continually varying between 0 and 2π . The difference of the phase rotor angle $\delta\theta_{SG}$ is represents the difference between SG SRF orientation and the rotation of grid voltage vector. The SG oriented SRF is applied for the modeling and control of the system, and the system electric model is analyzed in this

reference frame [30]. Consider that the amplitude of the per unit (pu) grid voltage \hat{V}_g is known, the grid voltage in the generator oriented SRF, V_g^{SG} , can be mapped as in equation (3.3) [31] and [32].

$$V_g^{SG} = \hat{V}_g \cdot e^{-j\delta\theta_{SG}} \quad (3.3)$$

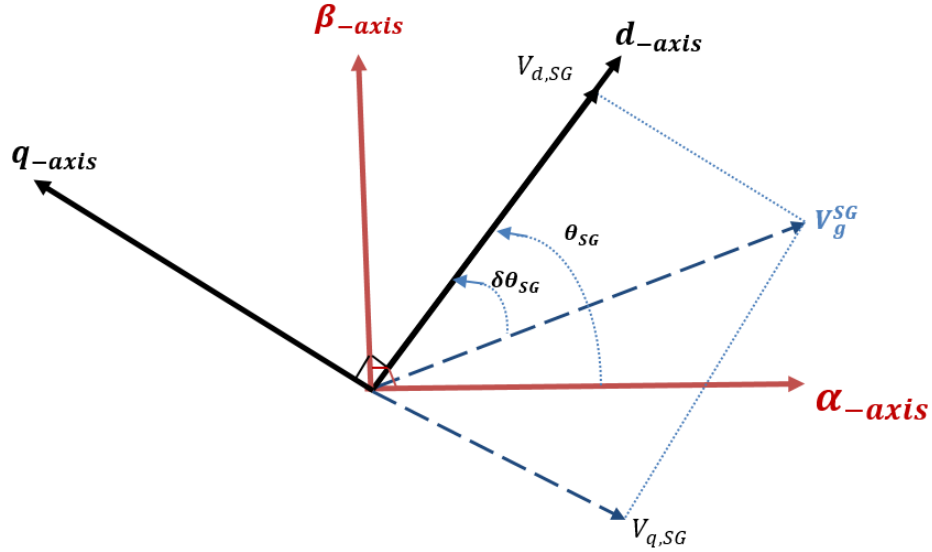


Figure 3.4: SG reference frame voltage vector relationship

The swing equation between synchronous generator and the grid can be represented in the SRF as shown in (3.4):

$$\frac{d\omega_{SG}}{dt} = \frac{1}{T_{SG}} (\tau_{m,SG} - \tau_{e,SG} - K_{d,SG} \delta\omega_{SG}) \approx \frac{d\delta\omega_{SG}}{dt} \quad (3.4)$$

Where:

$$d\delta\omega_{SG} = (\omega_{SG} - \omega_g)$$

$$\tau_{m,SG} = \frac{P_{m,SG}}{\omega_{SG}}$$

In these equations $\delta\omega_{SG}$ is the perunit deviation of the angular rotor speed; ω_g is perunit actual angular frequency of the grid; $P_{m,SG}$ is mechanical power input of SG in pu; $\tau_{m,SG}$ and $\tau_{e,SG}$ is input mechanical torques and electric torque of SG, all

in pu; T_{Sg} is inertia time constant and $K_{d,SG}$ is the damping factor constant. The term $K_{d,SG}$ will be equal zero, when the amortisseur circuit are ignored in the model [33] and [34] .

3.2.3 Equivalent circuits for D-axis and q-axis

The flux linkage between the field winding and the amortisseur is represented by the series inductance ($L_{fld} - L_{ad}$) as shown in the d-axis equivalent circuit. Because the flux linking the damper circuit is approximately equal to the one linking the armature (due to the damper winding being close to the air gap), this series inductance is usually ignored. However, this will only be the case if the damper circuit are fully pitched in practice. In order to maintain the identity of the field circuit, it is imperative to include the series inductance ($L_{fld} - L_{ad}$) in the equivalent circuit.

On the other hand, there is no field winding in the q-axis, hence the amortisseur represents the total effect of the eddy current paths and the damper windings. Consequently, it can be assumed that a single mutual flux L_{aq} links both the damper and armature circuits. Figures 3.5 and 3.6 show the equivalent circuits of the synchronous machine mapped to the synchronous dq0 reference frame. In addition, all the directions of current, voltages, resistances and inductances are labeled in in these circuits [19].

3.2.4 Per Unit Synchronous Machine Stator Voltage Equations

The generator stator voltage equations in the rotating reference frame are shown in equations (3.5)-(3.7) [30].

$$e_d = p\varphi_d - \varphi_q\omega_r - R_a i_a \quad (3.5)$$

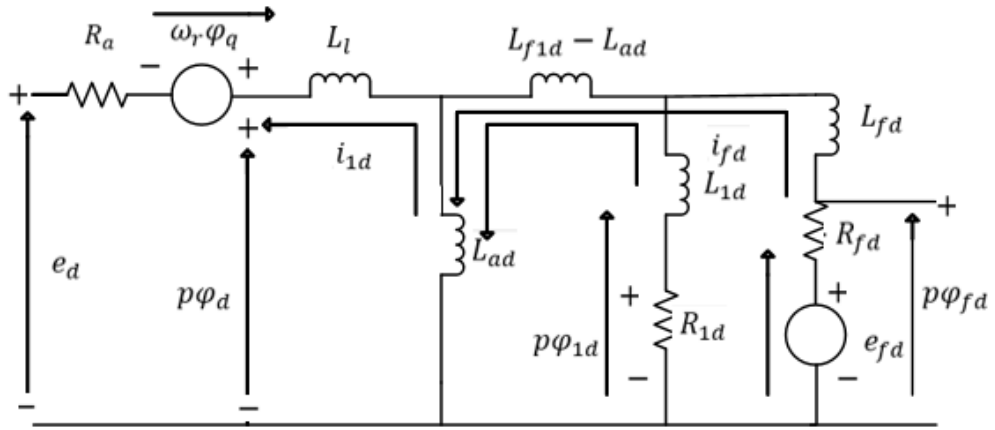


Figure 3.5: D-axis synchronous machine equivalent circuit

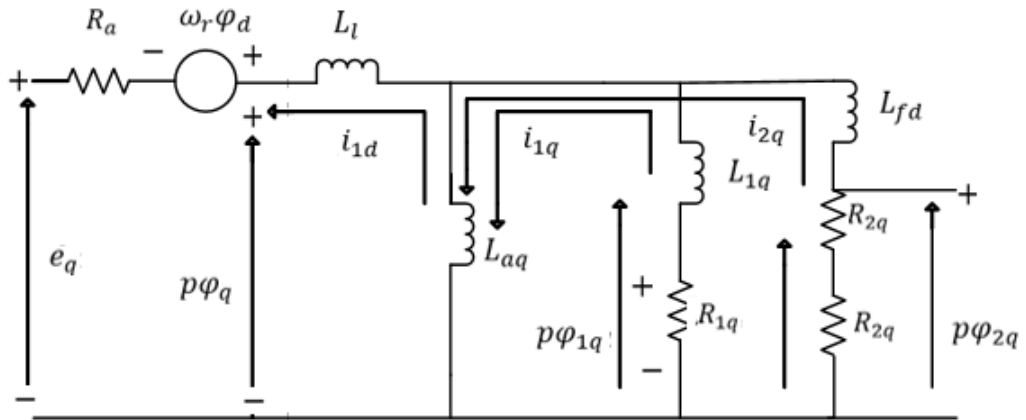


Figure 3.6: Q-axis synchronous machine equivalent circuit

$$e_q = p\phi_q + \phi_d\omega_r + R_a i_q \quad (3.6)$$

$$e_0 = p\phi_0 - R_a i_0 \quad (3.7)$$

Where ω_r is the angular velocity of the rotor in rad/s , (p) is derivative with respect to time, ϕ_d , ϕ_q are the armature flux linkages in per unit, and R_a is armature resistance in per unit.

3.2.5 Per Unit Synchronous Machine Rotor Voltage Equations

The rotor position does not affect the self-inductance and mutual inductance of the rotor currents, so they remain constant regardless of the rotor position. However, there is variance in the mutual inductance between the rotor and the stator with respect to rotor position θ [20]. The rotor voltage equations are shown in equations (3.8)- (3.11), assuming the rotor excitation is zero in the steady-state.

$$e_{fd} = p\varphi_{fd} + R_{fd}i_{fd} \quad (3.8)$$

$$p\varphi_{1d} + R_{1d}i_{1d} = 0 \quad (3.9)$$

$$p\varphi_{1q} + R_{1q}i_{1q} = 0 \quad (3.10)$$

$$p\varphi_{2q} + R_{2q}i_{2q} = 0 \quad (3.11)$$

Where, the flux linkages are $\varphi_{fd}, \varphi_{1q}, \varphi_{2q}$. And the parameters $R_{fd}, R_{1d}, R_{1q}, R_{2q}$ are resistances, i_{fd}, i_{1d}, i_{1q} and i_{2q} are the field currents.

3.2.6 Synchronous Machine Stator and Rotor Flux Linkage Equations in pu

The equations (3.12)-(3.18) are the results of the transformation of the flux linkages components of the stators and rotors into $dq0$, which are then converted to per unit [19]. The equations of the stator flux linkage in per unit are provided in (3.12), (3.13) and (3.14).

$$\varphi_d = -i_d(L_{ad} + L_1) + L_{ad}\cdot i_{fd} + L_{ad}\cdot i_{ad} \quad (3.12)$$

$$\varphi_q = -i_q(L_{aq} + L_1) + L_{aq}\cdot i_{1q} + L_{aq}\cdot i_{2q} \quad (3.13)$$

$$\varphi_0 = L_0 i_0 \quad (3.14)$$

Where L_{ad} and L_{aq} are the unsaturated mutual inductance of the armature d-axis and q-axis; while L_1 is the unsaturated leakage inductance of the armature.

To simplify the rotor flux equation, the rotor base quantities are properly selected to ensure that the mutual inductance in each axis between the rotor and stator circuits are equal [19]. The per unit flux linkage equations are shown in the following equations:

$$\varphi_{fd} = L_{ffd}\cdot i_{fd} + L_{f1d}\cdot i_{1d} - L_{ad}\cdot i_d \quad (3.15)$$

$$\varphi_{1d} = L_{f1d}\cdot i_{fd} + L_{11d}\cdot i_{1d} - L_{ad}\cdot i_d \quad (3.16)$$

$$\varphi_{1q} = L_{11q}\cdot i_{1q} + L_{aq}\cdot i_{2q} - L_{aq}\cdot i_q \quad (3.17)$$

$$\varphi_{2q} = L_{aq}\cdot i_{1q} + L_{22q}\cdot i_{2q} - L_{aq}\cdot i_q \quad (3.18)$$

Where the L_{f1d} is the unsaturated mutual inductance between the d-axis amortisseur and field circuit; $L_{1q}, L_{2q}, L_{1d}, L_{fd}$ are the unsaturated leakage inductance; while $L_{11d}, L_{11q}, L_{22q}, L_{ffd}$ are unsaturated mutual inductance that exist between d-axis amortisseur and the field circuits all in per unit.

$$L_{11d} = L_{f1d} + L_{1d} \quad (3.19)$$

$$L_{11q} = L_{aq} + L_{1q} \quad (3.20)$$

$$L_{22q} = L_{aq} + L_{2q} \quad (3.21)$$

$$L_{ffd} = L_{f1d} + L_{fd} \quad (3.22)$$

3.2.7 Power and Torque

The 3-phase instantaneous power output at the machine terminal in per unit calculated with in the dq0 frame components is given in the equation (3.23):

$$P_t = e_d \cdot i_d + e_q \cdot i_q \quad (3.23)$$

In addition, the air-gap torque (T_e) can be calculated the ratio of the power transferred through the air-gap and the rotor speed. The equation of the electromagnetic torque using the dq0 reference is given in the equation (3.24):

$$T_e = \varphi_d i_q - \varphi_q i_d \quad (3.24)$$

3.3 Replication of a SG model in VSC Control

3.3.1 Introduction of Virtual Inertia

In this research the emulated inertia is added to overcome some of the renewable energy sources' shortcomings. This will enable the renewable energy sources to have similar behavior to synchronous generators, and will contribute to the system's frequency control and will also support ancillary services for the power system.

Virtual inertia is the notion of simulating inertia where the response to power grid disturbances is disconnected from the power generation. This can be accomplished by adding another control to the power electronic interface controlling power output or by adding a energy storage system to supplement power injected to the power system. The control behaviors for VSG have already been implemented in simulation to support power system stability and reliability [35] and [36].

Equation (3.25) represents the power output of VSG and can be used as a study point for designing controls:

$$P_{VSG} = \frac{f - f^*}{R} - K_d(f - f^*) - K_J \frac{df}{dt} \quad (3.25)$$

where f is the frequency measured from the grid; f^* is designed stabilization frequency. The first term $\frac{f-f^*}{R}$ is the frequency droop term, which is determined from the desired frequency drop with changes in power. The second term $K_d(f - f^*)$ and the third term $K_J \frac{df}{dt}$, are the damping and inertia terms, which control the power transient response [37]. Implementing equation (3.25) in a VSC requires the ability to vary output power. If this is done with a PV inverter it will require normally operating below the maximum power point in order to be able increase or decrease output power following a grid disturbance. This research proposes adding an energy storage system to the dc link of renewable energy source to provide this variable output.

The inertia constant, K_J , represents the desired inertia response to imitate a conventional generator, which affects the rate of change of the frequency as well as the maximum deviation of frequency after the occurrence of a disturbance in the system. If generation facility controls are able to emulate virtual inertia, the active power has to be increased or decreased in proportion to the frequency deviation at the PCC or available energy storage.

The following requirements were used when implementing the VSG system in [35] and [37]

1. As seen in the block diagram in Figure 3.7, the VSG controls the active power in accordance to a frequency deviation error to provide damping.
2. The derivative of the gain, K_d , was set to be modifiable from 0 to 15 seconds in the machine base (values/unit).
3. The response of speed derivative was set to around 50 ms, with the possibility to increase the active power from the facility by 0.05 pu.

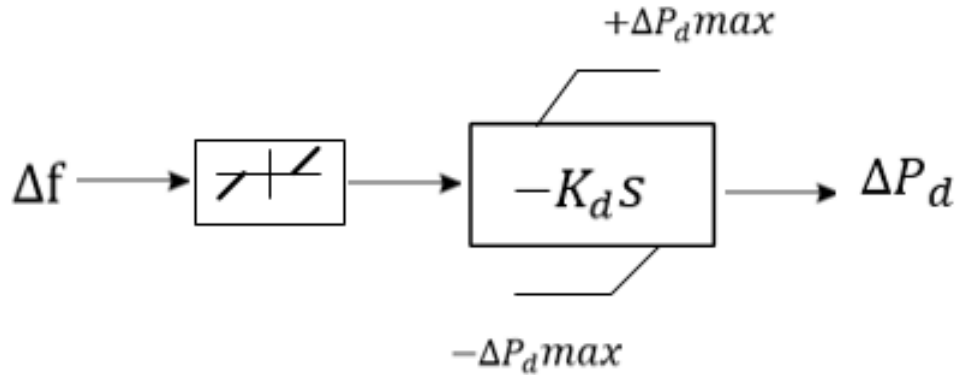


Figure 3.7: Damping Control [38]

4. At every control instant the active power should increase by ΔP_{max} from the previous value before the disturbance within a certain range whose increase is adjustable from 0 % (i.e. the block is not in use) to 10 % of the facility's nominal apparent power. Also, the control must reduce the power output using the same values as with the increment.
5. The stored energy must be available in the facility to provide the required increase or decrease ΔP_{max} . The energy storage in the facility absorbs or supplies power equivalent to 10% of the nominal apparent power for at least 2 s.
6. When the voltage is below 0.85 pu, derivative gain should be deactivated (taken out of service).
7. The system operator determines the K_d setting to be used depending on the prevailing requests of the electrical system.

The damping control system is designed minimize the oscillation depending on the increase or decrease at any moment by changing in the active power. To reduce the electromechanical oscillation behavior of the grid, the damping must be implemented to increase or decrease the magnitude of the active power output in response to the external oscillation, to damp the oscillation of the active power in frequencies 0.15 to

2 Hz [35] and [36].

3.3.2 Reference Frame Orientation of virtual synchronous generator

The synchronization control system of the virtual synchronous generator to the grid system is related to the effective phase angle of the virtual rotor of the VSG. The transformation between both VSG orientated SRF and stationary abc frame depends on the use of θ_{VSG} . In the PLL commonly used in grid connected converters synchronization is based on a fast tracking of the frequency and phase angle at the point of interconnect for the converter. In the case of the virtual synchronous machine orientated sequence reference frame has the same frequency of the grid voltage in steady-state, but it has an oscillator response to disturbances based on the swing equation, as will be discussed in Chapter 6. Figure 3.8 describes the effective rotor angle of the VSG, $\delta\theta_{VSG}$, which shows the difference between both d-axis for VSG orientated sequence reference frame and voltage vector at the rotating grid in a snapshot in time.

The VSG orientated sequence reference frame is used in the system for both modeling or control. The modeling of the electrical power system is mapped to the VSG reference frame. This has important features in the system modeling, because it helps to avoid multiple reference frame transformations between the global sequence reference frame (used for modeling electrical systems in a conventional converter Phase locked loop reference frame) and the local SRF (used for the VSG implementation of the controller) [34] and [39]. The voltage vector in the VSG orientated sequence reference frame is determined in equation (3.26), when the voltage at the point of interconnect to the grid, \hat{V}_g , is known:

$$\hat{V}_g^{VSG} = \hat{V}_g \cdot e^{j\delta\theta_{VSG}} \quad (3.26)$$

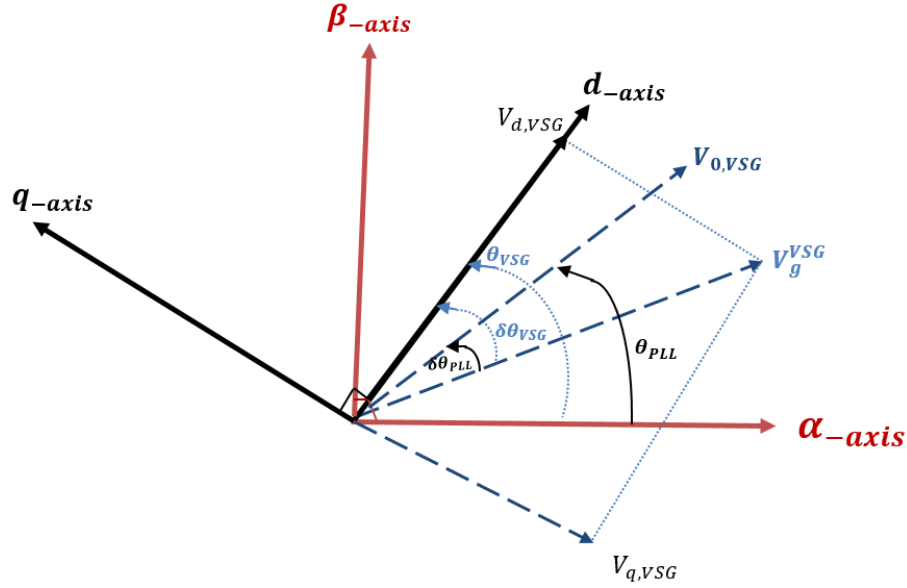


Figure 3.8: VSG reference frame vector and voltage complex space vector

In steady-state the PLL regulates the q -axis voltage in the converter reference frame to zero. The d -axis voltage reference is obtained based on traditional loop controller of reactive power [40]. The phase locked loop establishes sequence reference frame aligned with the vector of the voltage V_o . The displacement of phase angle of PLL with respect to the grid voltage is $\delta\theta_{PLL}$ which is similar to the virtual synchronous generator displacement of phase angle. Phase angle difference between PLL orientated SRF and VSG will be determined using the swing equation [39, 40]. This can be actualized by equation (3.27) [34].

$$V_0^{PLL} = V_0^{VSG} \cdot e^{-j(\delta\theta_{PLL} - \delta\theta_{VSG})} \quad (3.27)$$

3.4 Utilizing a VSC for VSG

The power system's frequency response can be divided into two main classes. The frequency controller of the power plants are not active in the first one, where it is dominated by the absorption or release of kinetic energy from the generator rotor.

Since the inertia impacts the change of frequency in this phase, the phase is referred to as inertia response. The primary control (governor action) and secondary control are used to first stabilize and then restore the frequency to its nominal value in the second class [35] and [36]. Automatic load shedding can be used as an additional measure in case of severe deviation in the grid's frequency tertiary control.

3.4.1 Droop Controller

A frequency droop control is implemented in the VSC to control output power to mimic both the natural behavior of the machine and the programmed governor control. Droop control is used in load sharing and main regulation of frequency. The advantage of adding droop control in the VSG is improvement stability of the grid. Droop control requires either that the DC link has large storage or that the power output of the PV or wind can be increase or curtailed. The DC link could experience large variation without contribution from energy storage or varying the output of the renewable source, which causes problems in the stability of the PV system.

There are two implemented controllers; either can be used in the droop controller. The first controller is essentially a combination of the conventional power converter control and an additional block used to adjust reference of the active power for the converter in response to deviation of the frequency. In this approach, the converter feeds the grid with the controllable, reactive and active power, becoming be a grid-supporting converter. The power reference that is obtained from the outer loop as shown in Figure 3.9 [35] and [36].

Figure 3.10 shows an alternative approach where the converter can be seen as a voltage source with a frequency which is calculated from the power error. As a result, the internal loop of the conventional converter inner controllers can reproduce the voltage directly based on the command. In addition, the frequency and the angle of the grid voltage source are used for synchronization. By using this method, there is

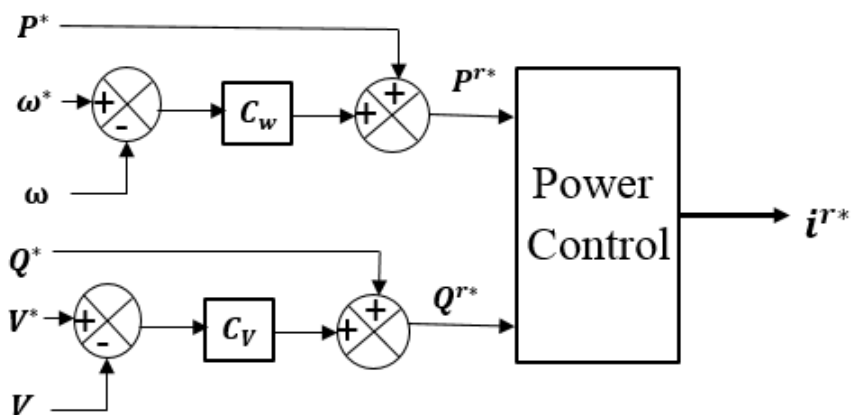


Figure 3.9: Voltage Magnitude and Frequency Droop Controller

no need to add any phase locked loop for synchronization, and the model will behave as voltage source behind an impedance [24].

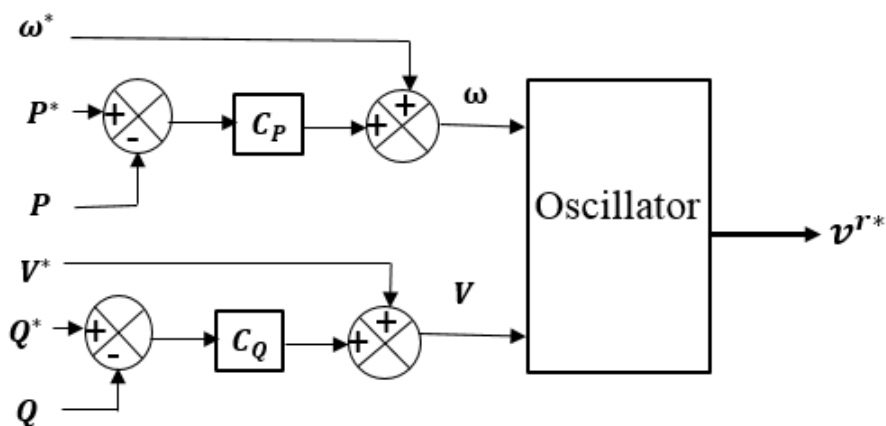


Figure 3.10: Droop Controller to Make Converter Behave as a Voltage Source Behind a Reactance

In this chapter, a general overview of the study conducted on synchronous generator's control requirement and its physical nature is presented. The aim of this study is to have a better understanding of inertia, damping controller, droop controller and load sharing properties of the Synchronous generator model. Being inspired by various existing modeling and control strategies of the modern SG systems, the best strategies that suits this research endeavor has been identified and implemented.

Also described in this chapter is the replication of a Synchronous generator

in voltage source converter control which focuses on emulated inertia services. It is expedient to have a comprehensive understanding of the concept and operation of the modern VSG implemented with contemporary control strategies in order to comprehend to need for this new functions. Therefore this chapter presents a detailed analysis of the consequences of reduced system inertia and the deployment of emulated inertia.

Chapter 4: Models for Inverter Coupled Generation and Storage

This chapter describes the models used in this thesis. The first section reviews the main features for control, design and specifications of the voltage source converter (VSC). The second section describes the PI controllers and phase locked loop controls modeling for the PV inverter. The third section, details the equivalent models for the PV generation system with a maximum power point tracking algorithm and the modeling of the battery energy system controls. The last section presents the BESS bidirectional buck/boost converter and the control methods to regulate the voltage on the DC link.

4.1 Voltage Source Converter

The major requirement of the renewable energy system with storage energy is the control of active and reactive power transferred to the ac system to help stability the voltage and the frequency in the power system. The most commonly applied approach to convert DC to AC in PV system as a voltage source converter (VSC). The VSC is connected to the power grid at a point designated as the PCC (point of common coupling). VSC independently controls the instantaneous active and reactive power at POI (point of interconnect). The phase angle, magnitude and frequency of the voltage output can be controlled using the inverter [41].

A dc capacitor is used for energy balance at the dc link. The dc voltage can vary significantly due to both the switching behaviour of the converter and the shifts energy balance between the dc and ac sides of the converter. Consequently, the capacitor must be large enough to handle the sustained charge/discharge current, during switching sequence of the converter. The VSC topology applied here uses six IGBTs each connected in parallel to a reverse diode as illustrated in the Figure 4.1 [41].

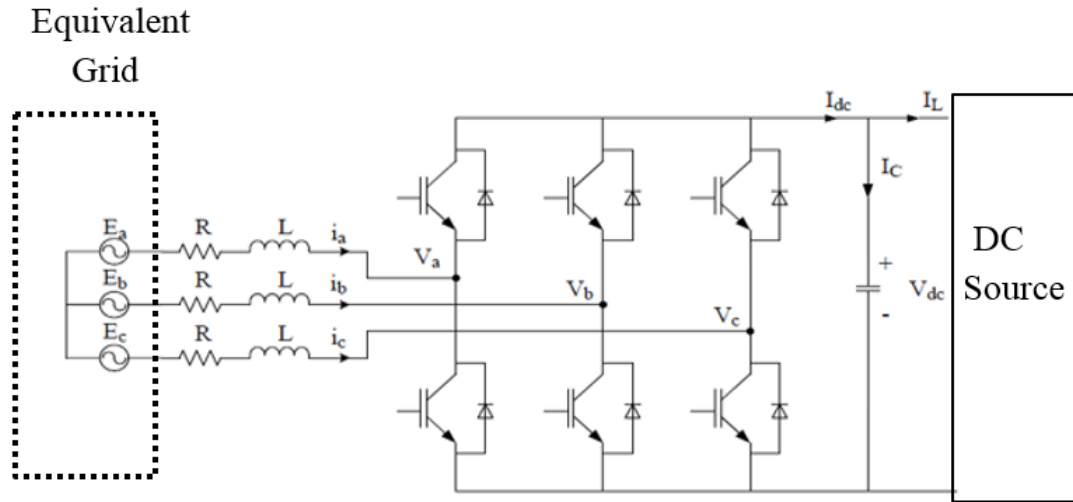


Figure 4.1: 3-phase two level dc/ac VSC

The switching of the IGBTs is controlled using a pulse-width modulation scheme. The PWM reference signal sets frequency, phase and amplitude for the converter output voltage. This makes it possible to regulate the converter's AC output voltage, phase angle and amplitude instantaneously. Regulation can then be conducted through different control loops to determine these two independent controls (amplitude and variables angle) [28] and [41].

4.1.1 VSC Interconnection with AC Grid

In order to connect renewable energy sources such as PV or wind to the power grid, different controllers are needed than to those with conventional energy sources. The renewable sources are often variable sources, due to dependence on the wind speed, temperature, variations in sunlight irradiance. Power generated from renewable sources presents a big challenge because it fluctuates significantly with time. Furthermore, the output power of renewable energy sources is usually DC, which is not compatible with the AC power grid [28] and [41].

When the VSC is connected to the equivalent grid as shown in the Figure 4.1, the

voltage loop equation across the R-L branch can be described applying Kirchhoff's voltage law resulting in equations (4.1) - (4.3) [28]

$$v_a = -Ri_a - L\frac{di_a}{dt} + e_a \quad (4.1)$$

$$v_b = -Ri_b - L\frac{di_b}{dt} + e_b \quad (4.2)$$

$$v_c = -Ri_c - L\frac{di_c}{dt} + e_c \quad (4.3)$$

Where:

v_a, v_b, v_c are the instantaneous converter terminal voltages.

e_a, e_b, e_c are the grid Thevenin equivalent voltages at the POI.

R is resistance between the POI and the converter terminal.

L is inductance between the POI side and the converter terminal.

By applying dq transformation to the synchronous reference frame, voltages in the d-axis and q-axis can be represented in equations (4.4) and (4.5) given as:

$$v_d = -Ri_d + \omega_e Li_q - L\frac{di_d}{dt} + u_d \quad (4.4)$$

$$v_q = -Ri_q - \omega_e Li_d - L\frac{di_q}{dt} + u_q \quad (4.5)$$

Where ω_e is the frequency in the grid, v_d and v_q denote d, q components of the voltage. The line current in the d, q components are represented by i_d, i_q .

4.1.2 VSC Power Controller

The ac power output from the inverter should be equal to that generated from renewable energy source. Both instantaneous active and reactive powers after dq transformation from the point of common coupling (PCC) can be calculated using the

measured voltage and current [42] and [43]. By ignoring the power losses in the VSG, the active power P_{out} and reactive power Q_{out} that is injected by power converter can be described by the following equations:

$$P_{out} = \frac{3}{2}(v_d \cdot i_d + v_q \cdot i_q) \quad (4.6)$$

$$Q_{out} = \frac{3}{2}(v_q \cdot i_d - v_d \cdot i_q) \quad (4.7)$$

Where v_d , v_q and i_d , i_q are the dq voltage and current at the PCC after transformation from abc to dq . The zero sequence term is neglected since the system is ungrounded on the ac side.

Figure 4.2 shows how the abc to $dq0$ transformation is used to compute output both active and reactive powers [42].

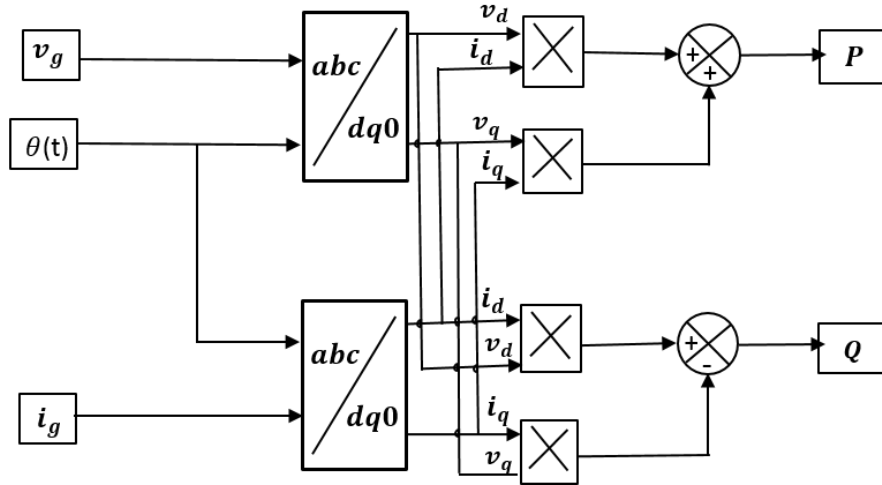


Figure 4.2: Compute active and reactive power

This makes it easier to implement power control in the grid side. The phase locked loop for synchronizing to the POI regulates v_q to 0 to align v_d with the positive peak of v_a . The above equations of injected active and reactive power can then be simplified as (4.8) and (4.9):

$$P_{out} = \frac{3}{2}(v_d i_d) \quad (4.8)$$

$$Q_{out} = \frac{3}{2}(-v_d i_q) \tag{4.9}$$

A closed loop feedback with a proportional-integral (PI) controller can improve the accuracy of the achieved active and reactive power. Figure 4.3, shows such control schemes for active and reactive power. The outputs of the control loop are the set point current regulators.

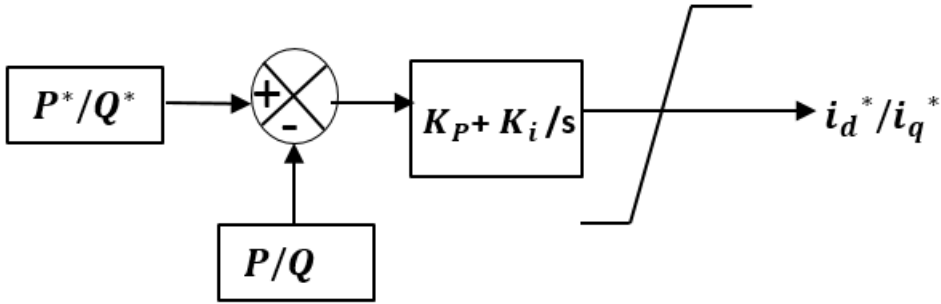


Figure 4.3: Active power and reactive power control

The real power or the DC link voltage can be controlled by using the active power control loop. On the other hand, the AC side voltage or the reactive power can be controlled by using the reactive power control loop [18].

4.2 Controller Specifications and Design of VSC

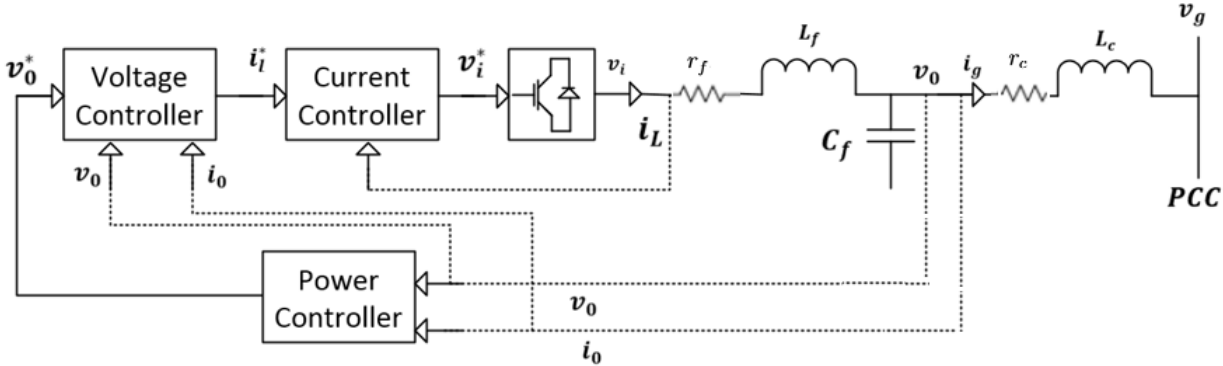


Figure 4.4: VSC Controller Design

The power section applied here consists of a three phase VSC and a LCL filter as

shown in the Figure 4.4. The controller of the VSC consists of two parts. The first part is an output loop control, which is either real power control, or a combination DC voltage control or an ac voltage control. The second controller is an inner current regulator, which is designed to reject the disturbances from the higher frequency switching and protect the VSC switching device from overcurrent [41] and [44].

4.2.1 Voltage Controller

Figure 4.5 shows the voltage controller structure. The d-axis and q-axis for the voltage components v_d^* , v_q^* are used as decoupled terms for the PI controller for the voltage. The voltage controller decoupling terms are related to the angular velocity of traditional SG. The output signal from voltage control are reference current values i_d^* and i_q^* which is used as the input of current controller [40]. The mathematical modeling details of PI controller for the output voltage at the capacitor filter in Figure 4.4 as described in equations (4.10) and (4.11):

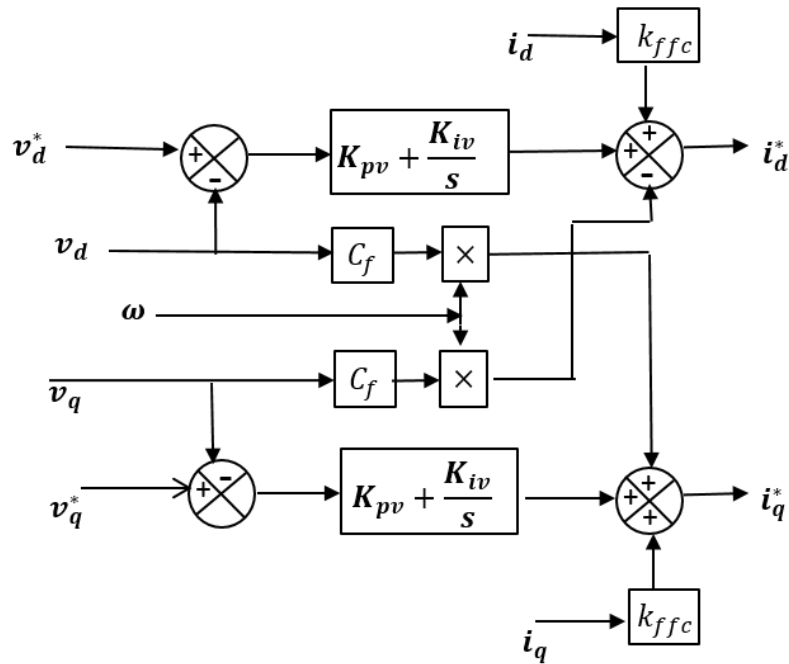


Figure 4.5: Voltage Controller of Implementation

$$i_d^* = (v_d^* - v_d)(k_{pv} + \frac{k_{iv}}{s}) - \omega C_f v_q + K_{ffv} i_d \quad (4.10)$$

$$i_q^* = (v_q^* - v_q)(k_{pv} + \frac{k_{iv}}{s}) + \omega C_f v_d + K_{ffv} i_q \quad (4.11)$$

Where k_{pv} and k_{iv} are the proportional and integral gains for the PI controller. The gain of the factor K_{ffv} is used for disabling or enabling feed-forward of actual measured currents at the power grid, and is usually adjusted between 0 and 1.

The voltage controller generates current references that should be limited to reject any over-current due to faults or disturbance in the grid system. When the reference of the current is saturated, the voltage controller should be protected from windup situation. Within the normal process range, these limitations would not affect the dynamic structure of the control [45] and [46].

4.2.2 Inner current control

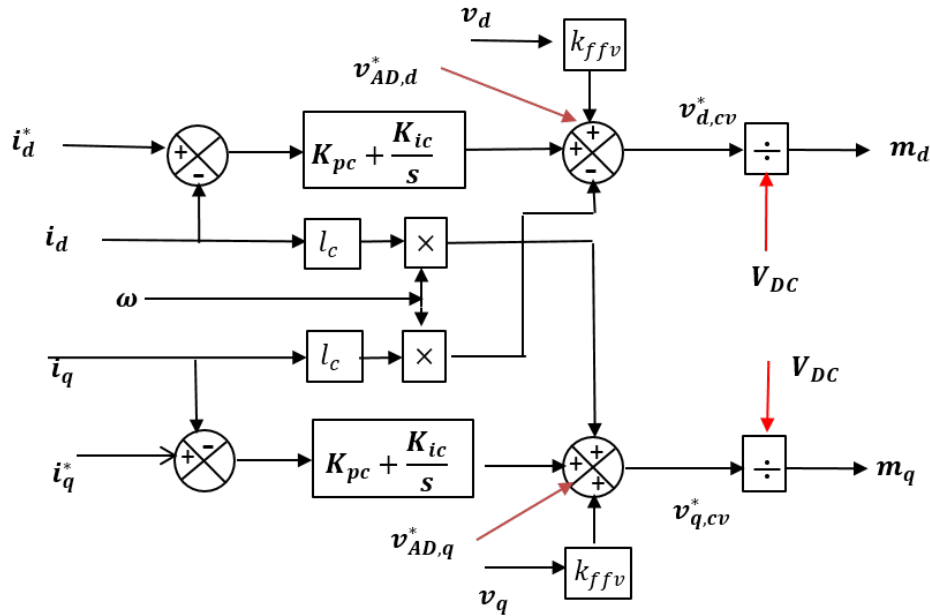


Figure 4.6: The inner current loop structure

The objective of inner current control loop, is to create the voltage modulation

reference for the PWM block such that converter's injected current is tracking the reference closely. The controller of the inner current loop for the VSC consists of decoupling terms with PI controller as shown in the Figure 4.6. The voltage output reference from the inner controller v_d^* is obtained from the combination of two other components namely a voltage feed-forward and current decoupling terms as written in the equation (4.12) [41], [43] and [44].

The state equations of the inner current control of the VSC from the Figure 4.6 can be written:-

$$v_{d,cv}^* = v_d K_{ffv} - \omega L_c i_q + (k_{pc} + \frac{k_{ic}}{s})(i_d^* - i_d) - v_{d,AD}^* \quad (4.12)$$

$$v_{q,cv}^* = v_q K_{ffv} + \omega L_c i_d + (k_{pc} + \frac{k_{ic}}{s})(i_q^* - i_q) - v_{q,AD}^* \quad (4.13)$$

Where gains of PI controller are k_p and k_i . The feed-forward voltages are v_q and v_d .

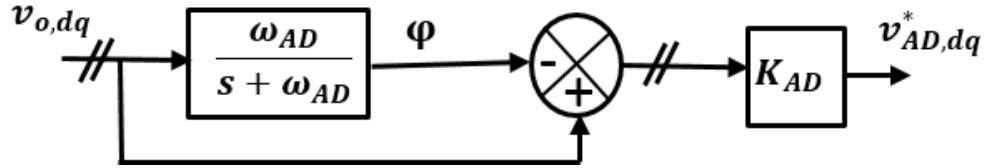


Figure 4.7: Active Damping Controller

The block diagram 4.7, shows an active damping controller v_{AD}^* which is added in the current controller loop to suppress the filter's LC oscillations. The implementation of the active damping is dependent on high-pass filtered value of the actual measured voltage v_0 from the difference between outputs of the low-pass filter and v_0 at the same voltage level. The obtained signal from high-pass filter will be multiplied with scaled factor, k_{AD} , and after that it will subtracted with the control signal of the current controller in order to eliminate oscillated voltages cross the capacitor. This is illustrated in equation (4.14) [39], [40] and [47].

$$v_{AD}^* = K_{AD}(v_0 - \varphi) \quad (4.14)$$

The cut-off frequency is ω_{AD} , φ is internal states of the low-pass filter used for the active damping gain, as shown in equation (4.15):

$$\frac{d\varphi}{dt} = (\omega_{AD}v_0 - \omega_{AD}\varphi) \quad (4.15)$$

Finally, the voltage output from inner current controller loop v_{cv}^* together with active damping are divided by measured dc voltage V_{DC} at the dc link determine modulation functions m . By ignoring the switching losses and any delay in the implementation of PWM, the output voltage v_{cv} of converter is the instant average is written in equation (4.16) [39].

$$m = \frac{v_{cv}^*}{v_{DC}}, v_{cv} = mv_{DC} \implies v_{cv} \approx v_{cv}^* \quad (4.16)$$

The DC/AC converter is modelled such that the AC system side is decoupled from the DC link. This ensures that neither circuit will affect the performance of the other during the power exchange situation. The power demand from AC side should be balanced from DC link of the VSC. It is necessary to have a sufficient real power source or stored energy source connected to the DC link to fulfill grid requirement.

The output current of the VSC is noisy and has harmonics at the POI. These harmonics can be filtered LCC filter.

4.2.3 High Pass Filter

The high frequency PWM switching of the VSC power electronics leads to the creation of voltage or current harmonics within the proximity of the switching frequency. The generated harmonics can produce disturbances impacting sensitive device on the grid

system. In some cases, this disturbance can cause power losses [41]. A filter is added to reduce this impact. The LCL filter in Figure 4.4 acts as a series low pass filter to allow the 60 Hz and low frequency voltage and current flow to the system and a shunt capacitor tuned to transfer high frequency harmonic and noise to neutral.

Likewise, the filter components can cause resonances due to harmonics of the power system if it is not designed appropriately. The magnitude of the reactive power produced by the filter increases proportionally as the filter capacitance increases, and this reactive power impacts the filter's design. In order to ensure that the shunt filter exhibits high shunt impedance characteristics at the nominal frequency of 60Hz, the capacitor of the RLC filter has to be carefully selected. Similarly, to determine the capacitor's impedance, 10-% of the MVAR rating of the generator would be taken or in some cases the per unit system calculations are used for impedance of the system [18] and [41].

The initial tuning of the LC resonance is performed with the resistance neglected. The inductance is chosen based on the capacitance calculated above such that the resonance is mean the switching frequency.

$$\omega_{re} = 2\pi f_s \quad (4.17)$$

$$L_f = \frac{1}{\omega_{re}^2 \cdot C_f} \quad (4.18)$$

Where the resonant frequency [rad/s] is ω_{re} , switching frequency Hz is f_s , filter capacitance [F] is C_f , filter inductance [H] is L_f . As choosing both L_f and C_f , and the parallel inductance impedance equal the value of the filter resistance R_f that will be chosen.

$$R_f = \omega_{re} L_f \quad (4.19)$$

4.2.4 Outer Loop Controller

A common objective for VSC outer loop is to balance the power injected to the DC link from the renewable resource with power transferred to the AC power grid. In the VSC, as described in the Figure 4.8, there are four commonly applied combinations of outer control loops: regulation of the (AC) voltage at PCC, control of the active power, regulation the voltage at DC link, and control of the reactive power. The i_q^* is output from the outer controller will be input for the inner current loop controller. The reactive power flow through the grid or regulation the voltage ac can be controlled by control of the q-axis component of the current (i_q). The active power flow or the regulation the voltage at DC link can be controlled by using d-axis component of the current (i_d) [41], [44] and [48].

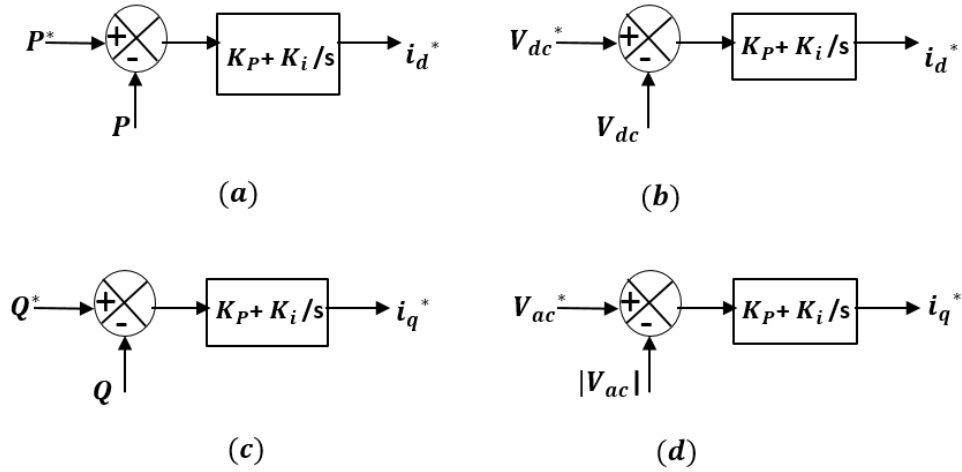


Figure 4.8: Outer Control Loop Option

4.2.5 DC Link Voltage Controller

From the equations (4.8) and (4.9), the injected or absorbed instantaneous active and reactive power from the power grid will be proportional to the current i_d and i_q . Equation (4.20) is shows the relation between ac voltage, dc voltage and modulation function of the PWM scheme for a three phase VSC electronic converter [42, 48].

$$V_{rms} = m_a \frac{V_{dc}}{2\sqrt{2}} \quad (4.20)$$

Where m_a is the amplitude of the modulation function of the PWM reference. The equation ignores the switching losses and the harmonics.

Figure 4.8(b) shows a comparison between the actual voltage at the DC link (V_{dc}^*) against the measured voltage dc voltage (V_{dc}). The output of this comparison is the error. This error is used to obtain the reference current (i_d^*) through a PI controller as shown in Figure 4.8 [28, 44].

Hence, a dc voltage controller is generally included in the control of a power converter. The balanced power at the dc side will be equal to the power at the ac side during a steady-state through the VSC is given as:

$$P_{ac} + P_{dc} + P_{cap} = 0 \quad (4.21)$$

$$\frac{3}{2}v_d i_d + V_{dc}I_{dc} + V_{dc}I_C = 0 \quad (4.22)$$

Where P_{ac} is power exchange in the ac side (*watt*), P_{dc} is the dc power side (*watt*). The I_C and I_{dc} are the at the capacitor current and average dc link current respectively. In the steady-state the average I_C is zero.

The derivative of the DC voltage is given in the following equation:

$$\frac{dV_{dc}}{dt} = -\frac{3v_d i_d}{2cV_{dc}} \left(i_d + \frac{2V_{dc}I_{dc}}{3v_d} \right) \quad (4.23)$$

$$I_{dc} = \frac{3}{4\sqrt{2}} m_a i_d \quad (4.24)$$

By controlling the d-axis current, i_d , the inner control loop can regulate the DC link voltage as shown in equation (4.24). This nonlinear relationship is the reason the PI controller is needed to linearize the equation and regulate the dc link voltage [48]. The dc voltage regulation as part of the larger control scheme can be seen in

Figure 4.8(b).

4.2.6 Tuning of PI controllers

A PI controller is a type of feedback control loop widely used in control systems. In this case the VSC has the proportional integral controller to control both the d-axis and q-axis current components as well as for the outer dc voltage regulation loop. The parameters of the PI controller should be carefully calculated to obtain the best performance of the closed loop controller. The major purpose of tuning PI controller is to make the cut-frequency be as high as possible in order to obtain faster system response, good oscillation damping and small overshoot [28] and [41].

The open loop transfer function is used for the symmetrical optimum, modulus optimum methods to improve the stability of the system and the response speed. In addition, the modulus optimum method is also utilized if the transfer function of the plants in the system is of low order (i.e. less than three), for making the cut-off frequency as high as possible. Then, the PI controller's integral time constant is selected to eliminate the dominant pole if the transfer function surrounds one leading pole and another negligible pole. The symmetrical optimum method is more appropriate when the transfer function has a pole at the origin or close to the origin. This method is used for tuning the PI controllers and it advantageous in that it enhances the phase margin.

PI controller is chosen in the VSG because it has fast response and the static error capacity is zero. The PI controllers in the VSC control dc voltage and current control loops.

4.2.7 Tuning for Voltage Controller

Starting from the structure of the voltage controller shown in Figure 4.5, the Modulus Optimum criterion method [49] is used to set the parameters K_{pv} and K_{iv} for

the controller. The transfer function of the closed loop current controller can be approximated to the first order. The transfer function of the open loop for the voltage controller described in the equation (4.25), by assuming ideal decoupling of both q-axis and d-axis [50].

$$h_{v,dq} \approx (k_{pv} + \frac{k_{iv}}{s})(\frac{1}{1 + T_{eq,c} \cdot s})(\frac{1}{T_c \cdot s}) \quad (4.25)$$

Where the $(\frac{1}{1+T_{eq,c} \cdot s})$ is closed loop current controller and $(\frac{1}{T_c \cdot s})$ is the filter capacitor.

The constant time $T_{eq,c,s}$ describes the closed loop response of the current controller and the filter capacitor integral time constant T_c is determine 4.26:

$$T_c = \frac{c_f}{\omega_b} \quad (4.26)$$

$$T_{eq,c} \approx 2T_v \quad (4.27)$$

The Symmetrical Optimum criterion [51] is used to adjust the parameters of outer voltage controller loop for the VSC as shown in Figure 4.5. By using this method to confirm that, the maximum phase margin is located at the crossover frequency of the transfer function. The proportional integral controller gains K_{pv} and K_{iv} are calculated in the equations (4.28) and (4.29).

$$K_{pv} = \frac{T_c}{aT_{eq,c}} \quad (4.28)$$

$$K_{iv} = \frac{T_c}{a^3 T_{eq,c}^2} \quad (4.29)$$

Where the parameter $a = 2\zeta + 1$ is based on damping factor of the closed loop transfer function.

The conventional tuning method needs a difference in bandwidth between the internal current controller and outer voltage controller. Usually, the value of the

parameter a is increased until the outer voltage controller bandwidth is at a minimum of one decade lower than the bandwidth of the inner current controller.

4.2.8 Tuning for the Current Controller

The structure for internal current controller loops are shown in the Figure 4.6. The open loop of the transfer function for the inner current controller is illustrated in equation (4.30). The measured voltages are included in a feedforward gain to stabilize the system for large disturbances and a current cross-coupling term is added to the q-axis and d-axis equations. The first term in the equation below is PI controller, while the second term is the approximation of the PWM and last term is response of the filter inductor. Where the constant time of the filter inductor is T_1 , and the PWM controller time constant is T_v [49].

$$h_{c,dq} \approx (k_{pc} + \frac{k_{ic}}{s})(\frac{1}{1 + T_v s})(\frac{1}{r_f(1 + T_1 \cdot s)}) \quad (4.30)$$

Where the $(\frac{1}{1+T_v s})$ is PWM approximation and $(\frac{1}{r_f(1+T_1 \cdot s)})$ is the filter inductor. Equations (4.31) and (4.32) are used to calculate the approximated values of T_1 and T_v :

$$T_v \approx \frac{1}{2f_s} \quad (4.31)$$

$$T_1 = \frac{l_f}{r_f \cdot \omega_b} \quad (4.32)$$

Based on the open loop of the transfer function equation, the Modulus Optimum method is used to calculate the proportional integral controller gains for the inner current control loop of the VSG. This method is used for provide critical damping with the closed loop transfer function, and it matches the open loop transfer function if the pole is ignored. The parameters of PI controller after applying Modulus Optimum methods become:

$$K_{pc} = \frac{L_1}{2T_v \cdot \omega_b} \quad (4.33)$$

$$K_{ic} = \frac{L_1}{2T_v} \quad (4.34)$$

With the addition of T_v equations (4.33) and (4.34), the switching frequency of the converter can be used to limit both parameters of the proportional integral controller and the bandwidth of the current controller. Nevertheless, the phase margin of the Modulus Optimum methods is relatively high, approximately 65° . Hence there is margin for increased controller gains and bandwidth at the expense of increased oscillatory response [49].

4.3 Synchronization

Synchronization to the power grid is an essential characteristic of grid side converter control based on the synchronous generator frame. A unity power factor can be achieved by synchronizing the delivered power by using an algorithm to detect the grid voltage's phase angle and aligning the current at the point of interconnect with it. The Park's transformation is applied to move the measured voltages and currents to the synchronous dq reference frame. A phase-locked loop is used to track the system phase angle using the three measured phase voltages on the grid side. The phase angle is calculated by integrating the sum of a PI controller output with reference frequency. The phase is locked by resulting the q-axis voltage to zero [18] and [41].

4.3.1 Phase Locked Loop

A phase-locked-loop (PLL) is the used for tracking the actual grid frequency. The PLL uses an algorithm to detect the frequency and the phase angle of grid voltage [41].

The control model implemented for the grid-connected inverter is illustrated in Figure 4.9. The measured AC voltage at the Point of Common Coupling is transformed to the synchronous dq reference frame and denoted as V_{sd} and V_{sq} in equations (4.35) and (4.36) [18].

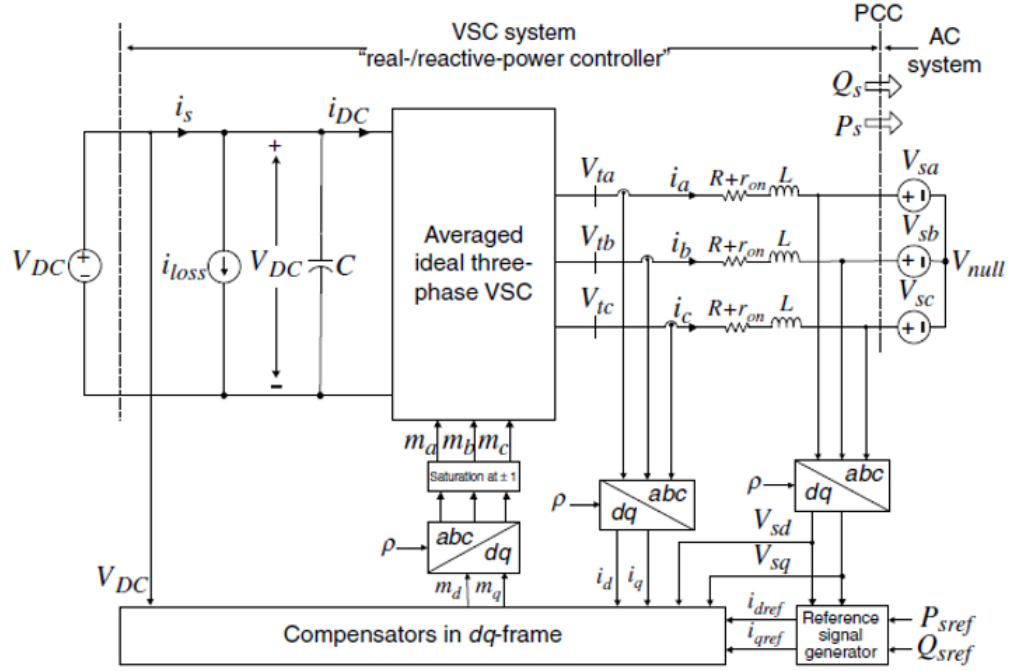


Figure 4.9: Block diagram of a real and reactive power in the dq -frame [18]

$$V_{sd} = V_s \cos(\omega_0 t + \theta_0 - p(t)) \quad (4.35)$$

$$V_{sq} = V_s \sin(\omega_0 t + \theta_0 - p(t)) \quad (4.36)$$

$$\omega(t) = \frac{dp}{dt} \quad (4.37)$$

In equation (4.36), $p(t) = \omega_0 t + \theta_0$ chosen to regulate $V_{sq} = 0$. Therefore, we design a feedback controller to align the phase and frequency to regulate V_{sq} to zero, as shown in the equation (4.38) [18].

$$\omega(t) = H(p)V_{sq} \quad (4.38)$$

where $H(p)$ is a compensator (linear transfer function).

Equation (4.39) describes to a nonlinear dynamic system response.

$$\frac{dp}{dt} = H(p)V_s \sin(\omega_0 t + \theta_0 - p(t)) \quad (4.39)$$

The PLL is tracking $(\omega_0 t + \theta_0)$, where the phase locked when $(\omega_0 t + \theta_0 - p(t))$ is almost zero. If the $H(s)$ has a low-phase frequency response then equation (4.39) shows a small sinusoidal perturbation near zero. Small variations of the frequency imply $\sin(\omega_0 t + \theta_0 - p(t))$ is approximately $(\omega_0 t + \theta_0 - p(t))$, which simplifies (4.39) to (4.40) [18]

$$\frac{dp}{dt} = H(p)V_s(\omega_0 t + \theta_0 - p(t)) \quad (4.40)$$

Figure 4.10, shows the feedback of a generic closed loop PLL control system.

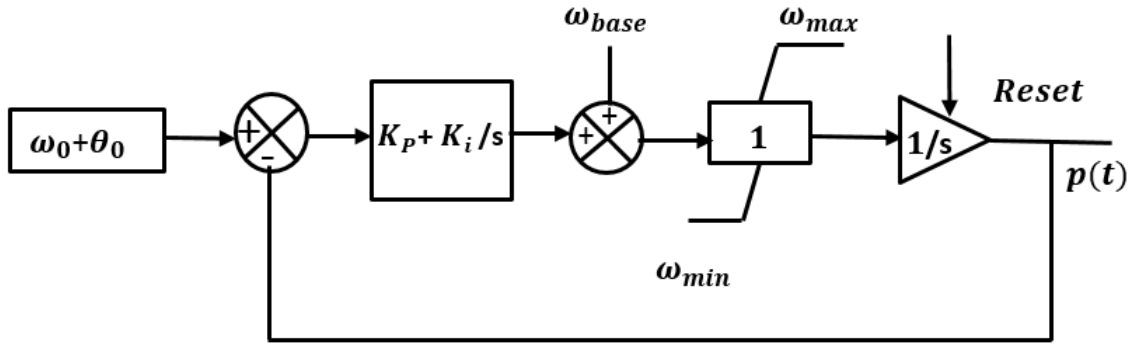


Figure 4.10: Block diagram of basic single phase PLL controller [18]

Figure 4.11 shows a three phase PLL that applies the Park's transformation to transform the line voltages (V_{sa}, V_{sb}, V_{sc}) and computes the angular speed ω of the dq -transformation. For the PLL to work properly v_{sq} should be zero in steady state which implies there is no voltage difference between v_{sd} and the peak of v_A [18].

The voltage controller oscillator (VCO) is used to create as a resettable integrator output. Each time it completes 2π radians it resets ρ to zero. VCO is a feedback

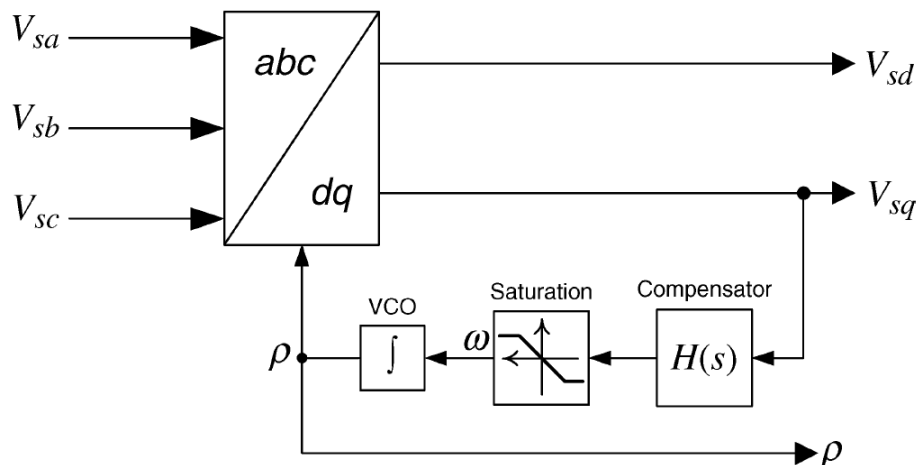


Figure 4.11: Schematic diagram of the SRF-PLL [18]

control block, which oscillates at a controlled fundamental frequency. For example for 60 Hz system $\omega = 376.99 \text{ rad/s}$.

As a result, PLL computes a synchronous reference measuring the frequency at PCC [18].

4.4 Determining Battery Ratings and Description of Proposed Solution

This chapter describes the system model used and describes methods for ratings battery power and energy ratings for the application. The implemented virtual synchronous generator and synchronous generator are modeled based on the concept of dual modeling and they are represented similarly will building on Chapter 6. Usually, the electric power networks are operating at a normal steady-state where the total generated power meets the total load plus system losses and frequency experiences small, slow variations in response to changes in load or renewable generation output. During abnormal operating conditions, the system frequency will exhibit larger, oscillatory variations.

4.5 Battery Sizing Calculations

Due to the increasing penetration of renewable energy in power generation, the frequency instability in the system may become a concern due to reduced inertia. The swing rated for the response due to a large change in load or generation can exceed the ability of convention control mechanisms to respond to stabilize the system. Energy storage systems can be used to emulate the response of large synchronous machines [52]. This research proposes adding energy storage on the dc link of PV inverters to provide inertia emulation. Ignoring the power losses, the power balanced between the PV generation, power from the storage system and the inverter output power is given by equation (4.41):

$$P_{Load} = P_{PV} + P_{ESS} \quad (4.41)$$

Where the P_{ESS} is the power absorbed or supplied by the storage energy

The VSG model describe in chapter controlled the real power set point for the inverter based on the swing equation. The energy storage connected to the dc bus of the inverter enabled this response. There are two methods to adjust the inertia response when severe disturbance occurs in the PV generation as proposed in the [52]. In the first option, frequency reserve capacities can be increased by increasing the responsive reserve generation, usually in the form of gas turbines. In addition, accommodating the alternating nature of the PV generation results in frequency ramping of conventional generation, the power plant components' efficiency.

The coordination between ESS and PV control is an important requirement, which is implemented in this research in order to enhance the output power of the PV integration and support the frequency. In addition, when the frequency becomes unstable, the BESS helps to enhance system stability by regulating the frequency of the power system, which is similar to the synchronous machine's inertia behavior. To create PV output power that would be similar to that of the SG output power under the principle of frequency regulation standards, new characteristic control converter of PV generation storage was created by adding the VSG technology. In most design of the VSG, PV generation is combined with ESS (such as the battery) and controlled on the dc bus of the converter. This design requires the structure described in Chapter 5 interfacing the energy storage system to the dc link through a bidirectional dc-dc converter that is controlled to regulate the inverter dc link voltage. .

In an alternative method, the output of the PV generation is operated below the maximum power point with case the generation level is de-rated [53]. The additional capacity, which is analogous to the spinning reserve in synchronous generator, supplies the required inertia response when there is disturbance in the system. The downside of this method is the lost revenue due to operating below the maximum power point. This approach is only economical if there is a market for supplying ancillary services. Another method which improves wind generation system's frequency

response through the depletion of the stored energy was proposed in [28]. Such approach can be implemented in the PV generation system, albeit with a very large dc-link capacity if the system is designed to be capable of responding to major disturbances. The peak power transfer rating of the storage and total energy storage capacity need to be selected to ensure the VSG provides sufficient emulated inertia.

4.6 Energy Storage System Power Capacity Calculation

This section is focused on amount of the storage energy required to support the system with low rotating inertia due to combine of large amount of the PV generation and estimate size these devices to keep stability in the system. To maintain stability in the power system, some researchers proposed sizing of the battery energy storage system devices is to be 10% of the distributed generation capacity [2]. The steady power transfer from a synchronous machine can be approximated by equation (4.42) if the stator resistance is neglected.

$$P_e = \frac{E_G \cdot E_M}{X_T} \cdot \sin\delta \quad (4.42)$$

When the suddenly large load is connected to the grid system, the SG starts to decelerate by inject stored energy from the rotor since the mechanical power can't change. If the suddenly large load is disconnected from the grid system, the synchronous generator start to accelerate.

The output from the PV stays constant during the power system disturbance. The energy storage supplies or absorbs power to allow the inverter to be controlled as a VSG. Equation (4.43) shows the role of the energy storage in the virtual synchronous generator control [2] and [54].

$$\frac{2H}{\omega_s} \cdot \frac{d\omega}{dt} = P_{m,VSG} - P_e \pm P_{ESS} \quad (4.43)$$

4.7 Sizing the ESS to Enhance Stability

If the change in angle of the synchronous machine in response to a disturbance is too large, the machine may lose synchronism with the ac system. Otherwise, If the machine has more inertia, the change in angle will be smaller and the machine will be likely to lose stability. In the case of the VSG, the energy storage system is sized to emulate the behavior of the generator. To simplify the calculation for rating the energy storage the small signal response of the VSG around the operating point is linearized and the emulated mechanical input power is assumed to be constant [4] and [2].

Equation (4.43) can be treated as linear if the mechanical power is constant and the change in electric power is linearized for small angles, resulting in (4.44).

$$\frac{2H}{\omega_s} \cdot \frac{d^2\delta_m(t)}{dt^2} = -K\Delta\delta \quad (4.44)$$

Where the K is the coefficient of the synchronizing power, which is calculated by using equation:

$$K = \frac{dP_e}{d\delta} = \frac{|E_a| \cdot |V_t|}{X_s} \cdot \cos\delta_0 \quad (4.45)$$

During abnormal condition the BESS should charge or discharge to slow the acceleration of angle, thus the BESS is support the power that will be equal the right-hand part from equation (4.46) [2] and [52].

$$P_E = \frac{|E_a| \cdot |V_t|}{X_s} \cdot \cos\delta_0 \quad (4.46)$$

4.8 Power Balanced Based on Swing Equation

The application of the virtual synchronous generator studied in this thesis is based on the conventional swing equation, which mimics the inertia in the SG. The implementation of this swing equation is linearized in relation to the speed as shown in equation (4.43). The virtual inertia's acceleration is calculated by power balance as represented in equation (4.47):

$$\frac{d\omega_{VSG}}{dt} = \frac{1}{T_a} (P_{m,VSG}^* - P_{out}) - P_d \quad (4.47)$$

Where:

$P_{m,VSG}^*$ is the pu virtual machine power input.

P_{out} is active power electrical measured from the grid (pu).

P_d is the damping power of VSG is defined (pu).

T_a is the constant time of virtual inertia which represents the inertia constant $2H$ in the conventional SG.

As represented in the block diagram in the Figure 4.12, the angular speed of the VSG is defined as ω_{VSG} which is integral from derivative of angular speed, while θ_{VSG} is resulting from integral of the ω_{VSG} . Also it describes the model of VSG based on the conventional swing equation. The damping power P_d mimics the power damping impact in the conventional SG, which implemented in the virtual synchronous generator based on the difference between ω_{VSG} and the measured PLL speed ω_{PLL} . The resulting difference will be multiplied by the damping factor of VSG, K_d [50] and [55].

In addition, part of Figure 4.12 shows the active power control (APC). The droop control represents the equivalent frequency speed governor SG steady-state characteristic. The virtual mechanical, P^{r*} , in the external loop is used as the reference input for the VSG. Thus, the APC is obtained by multiplying the droop constant gain

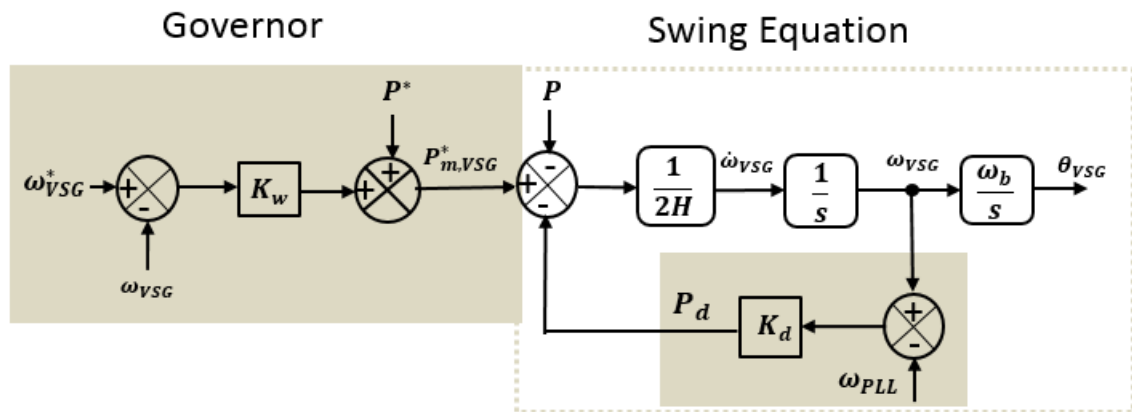


Figure 4.12: Power control loop of VSG emulation based on swing equation.

K_w with the difference between reference speed ω_{VSG}^* and actual ω_{VSG} and finally by adding to the external active power reference [52].

Chapter 5: Utilizing Photovoltaic Generation Combined with Energy Storage

This chapter consists of material from two papers, the first paper is published in the proceedings of the IEEE Innovative Smart Grid Technologies (ISGT) Conference held in Washington, DC from February 17-20, 2019. And the second paper is published in the proceedings of the IEEE 51st North American Power Symposium (NAPS2019) held in Wichita, Kansas from October 13-15, 2019.

5.1 Design and Test of a Combined PV and Battery System Under Multiple Load and Irradiation Conditions (paper 1)

5.1.1 Introduction

In order to overcome the challenge of relying on fossil fuels, research on green energy sources can help sustain the power supply for the world. Most of the world's islands can benefit from renewable energy, as the majority of them are currently dependent on fossil fuels. PV generators are connected to the power grid with power electronic converter to improve the system efficiency, stability and reduce cost [56, 57]. The implementation of PV generation in a real grid is a very challenging task. The response to load changes as well as irradiation and temperature changes in the output characteristics of PV panels non-linear. Due to the dependency of these variables, the use of a Maximum Power Point Tracking (MPPT) technique is important since it will result in a PV generation system providing the maximum power possible. There are many ways used to implement MPPT algorithms such as Incremental Conductance (IC) methods, Perturb and Observe (P&O) methods, and constant voltage methods [58].

Battery energy storage system (BESS) have become more widely used in the

distribution systems and especially with PV [56]. Energy storage has a significant role in helping the system to become stable and reliable, such as when the generated power from the PV is unavailable. When the output power from PV is decreased, the battery can supply power to the grid to maintain a constant DC link and stabilize the grid [57]. Also, the battery can be charged for the grid when the load demands less power than is generated [59].

In this paper, we are trying to make the interconnection of PV generation more stable and reliable by using BESS. The model is based on large paired batteries to store energy acquired during sunlight hours. The PV generation derives power from combination of small PV cells structured in parallel or series configuration. A single PV cell is capable of generating power approximately between 1-2 watts depends upon semi-conductor material. The PV system has two basic functions when connected to a battery to provide energy on-demand to electrical loads and provide storage for excess electrical energy generated by the PV array. The latter of which filtering out transient variations in the PV system outputs to provide electrical loads power with stable currents and voltages [60].

In order to have a larger battery capacity and a longer life cycle, the capital and operational costs will be higher. If the battery discharges at a current higher than its rated limits or is charged faster than its limits, then the cycle life of the battery will decrease. This can be overcome by selecting a battery that has a suitable maximum capacity and charge and discharge rates. This will increase the lifespan of the battery. There are four kinds of battery chemistries commonly considered for grid application which are: - Lithium-Ion (Li-Ion), Lead-Acid, Nickel-Cadmium (NiCd) and Nickel-metal-hydride (Ni-MH). In this paper, the battery is connected to the DC link of the PV system for stabilization and voltage regulation [61].

5.1.2 System Architecture

As shown in Figure 5.1, the power system model consists of different components: PV, MPPT control, boost converter, BESS, bidirectional DC/DC converter, and a DC/AC inverter. These models were implemented in an empty type program environment along with their corresponding control circuits as explained in the following sub-sections

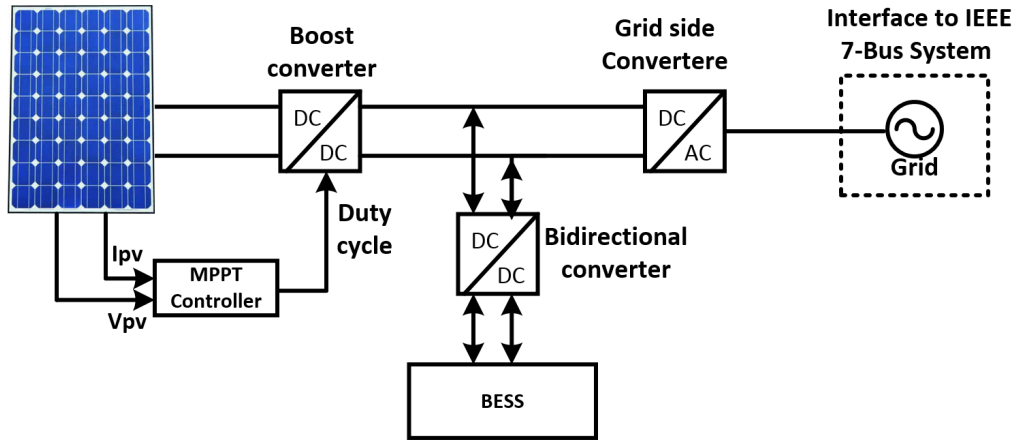


Figure 5.1: The schematic diagram of the power system

5.1.2.1- PV Model

A PV cell is represented by an equivalent circuit of its series resistance (R_s), parallel resistance (R_p), and one diode connected in parallel with a current source that represents the sunlight generation as shown in Figure 5.2.

There is a non-linear relationship between current and voltage created by the diode in this circuit. The mathematical model of an ideal PV cell can be described through the I-V characteristics curve theory of semiconductors [58]. The basic equation showing the output current I_{pv} of a PV module array that consists of a group of modules connected in parallel (N_p) and in series (N_s) cells combinations is

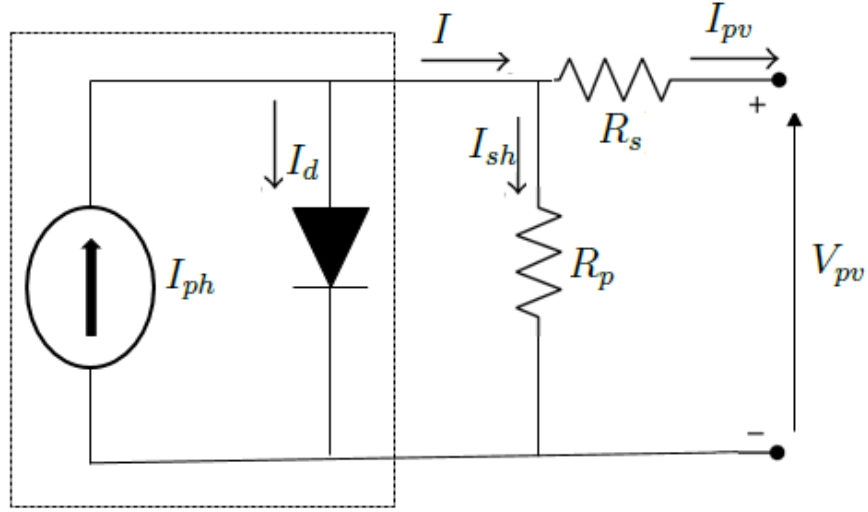


Figure 5.2: Ideal single diode PV model

$$I_{pv} = N_p \cdot I_{ph} - N_p \cdot I_o \cdot \left[\exp\left(\frac{1}{a \cdot V_t} \cdot \left(\frac{V_A}{N_s} + \frac{I_A \cdot R_s}{N_p}\right)\right) - 1 \right] - \frac{N_p \cdot V_A}{N_s \cdot R_p} - \frac{I_A \cdot R_s}{R_p} \quad (5.1)$$

The photon current is given by I_{ph} , I_o is the reverse saturation or leakage current of the diode and the thermal voltage is V_t . The shunt resistance is given by R_p and R_s represents series resistance. The variable a is the diode ideality constant between [usually between 1 -1.5]. The steps of calculating I_{pv} and the parameters of the KC200GT solar module at $25C^\circ$ and $1000 W/m^2$ are taken from [62].

5.1.2.2- MPPT Controller Model

A maximum power point tracking (MPPT) algorithm is an algorithm used to extract the maximum power from the PV array at a given instant of time. The solar irradiation is changing with time which causes variation in other physical quantities like environment temperature and solar cell temperature which can cause the PV cell MPP to change. The MPPT algorithm measures the voltage and current of PV array, and the power generation will be $P = V * I$. The MPPT algorithm tracks those

variations in the MPP to get maximum power output from the PV array [63].

In this paper, the Perturb and Observe (P&O) method is used due to the following advantages. The MPPT can have fast tracking when the perturbation is large and the needed accuracy is low. P&O algorithms work by taking measurements of both the terminal PV voltage and the PV current by adding small disturbances. Figure 5.3 describes the P&O method algorithm; the MPPT algorithm decreases or increases the duty cycle and observes the new power output. Then it compares the output voltage and current output from the PV array to find the MPP [59].

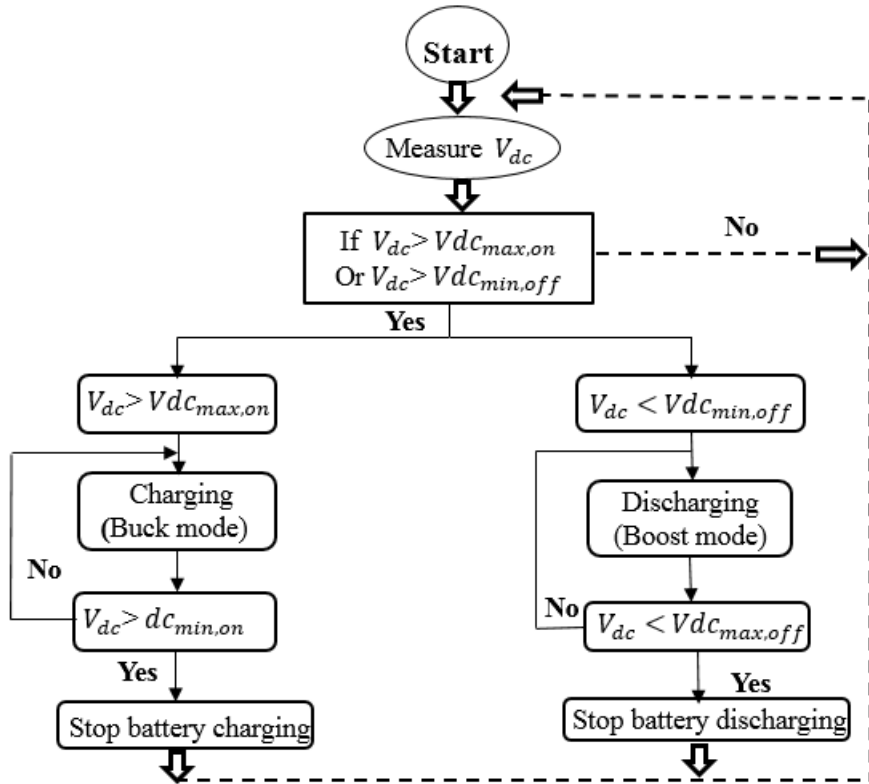


Figure 5.3: MPPT algorithm based on P&O method

From the PV power characteristic curve shown in Figure 5.4, the relationship between the change in power with respect to the voltage should be zero at the MPP when the duty cycle remains constant because it is defined by equation $\frac{dP}{dV} = 0$, where dP incremental change in power, and dV is the voltage incremental. If the duty cycle is increased, the instantaneous power is more than the previous power then the slope

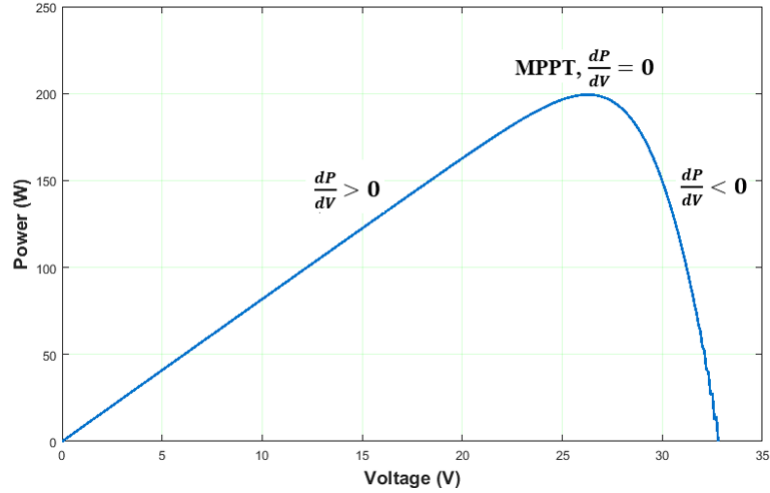


Figure 5.4: MPPT function based on P&O method

is positive $\frac{dP}{dV} > 0$. This is referred to as the voltage source region and the duty cycle will operate at a higher value. If the instant power measured is less than the previous power and the slope is negative, $\frac{dP}{dV} < 0$, then the duty cycle should be decreased by a small perturbation amount until the new MPP is reached. This is referred to as the current source region and the duty cycle operates with a lower value. Depending on the sign of, $\frac{dP}{dV}$, the algorithm decides on whether the duty cycle should be increased or decreased. Once the steady state power operating point is achieved, the MPPT will oscillate around the MPP [64]. The condition $\frac{dP}{dV} = 0$ for the DC-to-DC boost converter in this project is satisfied using the MPPT technique which regulates the pulse width modulation (PWM) control signal until this condition is met [60, 65]. When the PV is connected to a large grid then, it needs a boost converter to step up the voltage and match the voltage level designed for the DC link.

5.1.2.3- Boost DC/DC Converter Model

Since the output voltage of PV cell is low, the low voltage power taken by the PV array is converted to a higher voltage level using a unidirectional boost converter to allow utilization of the low voltage PV generation system for the grid. The configuration of

the unidirectional DC/DC boost converter with a MPPT algorithm control system is presented in Figure 5.5. The used the standard boost converter model described in [66, 67] is used in this work.

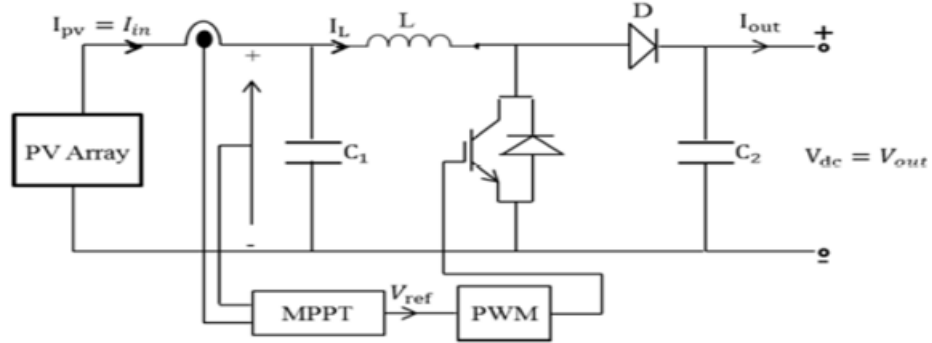


Figure 5.5: BDBBC operation modes [66]

5.1.2.4- Battery Energy Storage System Model

In this research, the an equivalent circuit battery model is used for dynamic simulation rather than electrochemical or experimental battery models. In this work, the generic battery model of a Lithium-Ion battery is used. The battery is modelled as a controlled voltage source. This battery model consists of a controlled voltage source connected to a series resistance as shown in Figure 5.6 [61]. The equations for the Lithium-Ion battery during discharge and charge modes is given in 5.2:

$$V_{Batt} = E_0 - Ri - -K\left(\frac{Q}{(Q - it)}\right)i^* + Ae^{(-B.it)} \quad (5.2)$$

The no load constant voltage is described by E_0 , i is the battery current and i^* represents the low frequency current dynamics. The exponential capacity factor given by B , which is the extracted capacity and Q is the capacity of the battery. The variable K is the polarization voltage constant, R is the internal resistance, A is the exponential of voltage zone amplitude and V_{Batt} is the terminal battery voltage.

The parameters for both discharge and charge modes are assumed to be the

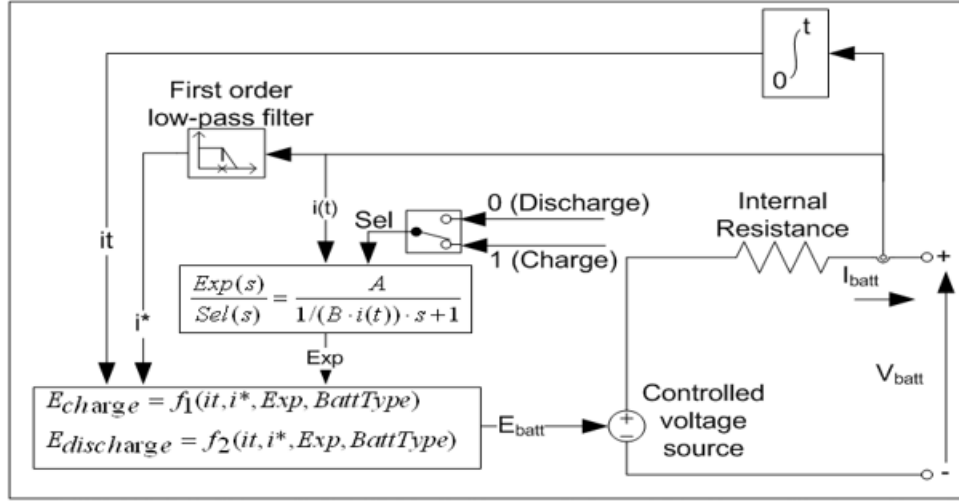


Figure 5.6: The equivalent circuit for a Lithium-Ion battery [68]

same; battery sizing is not calculated; the effect of temperature on the battery model is neglected for both discharging and charging the battery; and the internal resistance value of the battery is treated as constant so it does not change [59].

The main objective of the battery controller is to maintain a constant voltage at the DC link. Charging and discharging will vary the battery terminal voltage. The voltage reference at the DC link can be kept higher relative to the terminal voltage of the battery bank. In this work it is assumed that when the SOC is 85% the battery can supply 2.6 MW for one hour. The battery discharge rate is given by 5.3 [68]

$$\frac{2.6MW * 1hr}{900 * 0.85} = 3.4kAhr \quad (5.3)$$

5.1.2.5- Bidirectional Buck-Boost Converter (BDBBC) Model

The battery bank is connected to the DC link through a bidirectional DC/DC converter, which consists of two switches S1 and S2 that allow the converter to work as either a buck or a boost converter. As shown in Figure 5.7, when the converter works in boost mode, then the battery is discharging, and the DC link receives full power. Correspondingly, when the converter works in buck mode, it allows the battery to

charge by consuming power from the DC link [69].

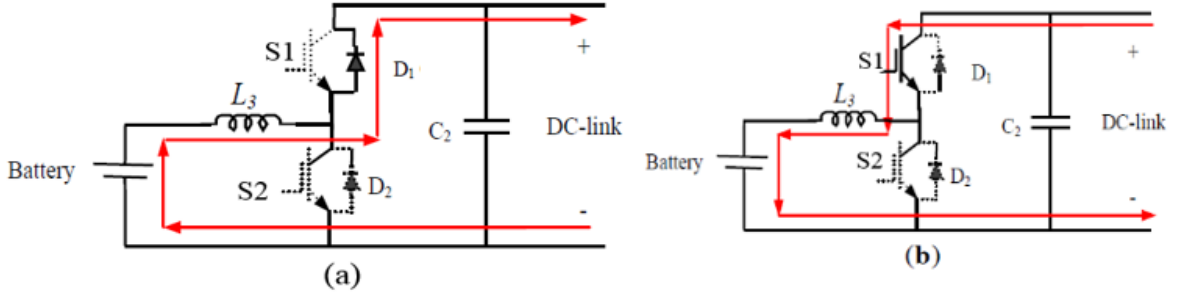


Figure 5.7: The BDBBC operation modes[69]

The control system of BDBBC consists of two main functions. An outer controller, which is responsible of regulating the voltage at the DC link, and an internal controller, that is responsible for regulating the battery current as shown in Figure 5.8 [61, 65].

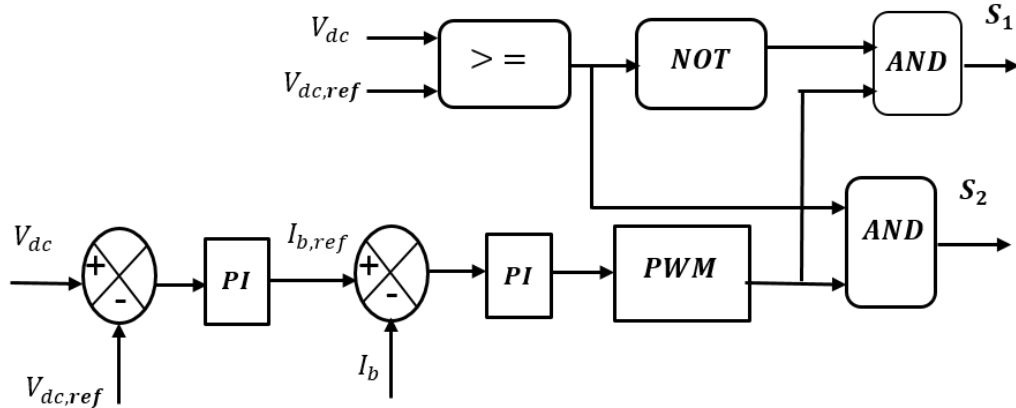


Figure 5.8: The control scheme of the BDBBC

5.1.2.6- The DC/AC Inverter Model

The DC side of the inverter connects the PV output and the battery is connected to the bulk grid through a DC/AC inverter. The inverter model is built based on a two level three phase voltage source converter (VSC). Since the high frequency switching behavior of the VSC is not our focus in this paper, a state space average model of

the VSC is implemented to represent the steady-state and low frequency dynamic conditions [18]. The control schemes for the VSC consist of two parts, inner and outer controls. The inner control, or current control, takes the error between the measured current of the AC system in the synchronous reference frame direct axis i_d and the reference current i_{dref} through a PI regulator to get the d-axis reference frame voltages. A similar loop is used in the q-axis. Then, these voltages are combined with two other components: a voltage feed-forward and current decoupling terms and scaled by to DC voltage to calculate the modulation functions m_d and m_q . The q-axis voltage at the point of common coupling is regulated to zero when proper synchronization is attached. The outer control or the voltage control is used to generate the reference quantities of the direct and quadrature currents i_{dref} and i_{qref} based on the output power of the PV and the desired ac system power factor setting. The inner and outer controls for the direct axis control loop are shown in Figure 5.9. The measured ac side terminal voltages and currents are transformed from the stationary abc phase domain to the two axis synchronous reference frame using the Park's transformation [18].

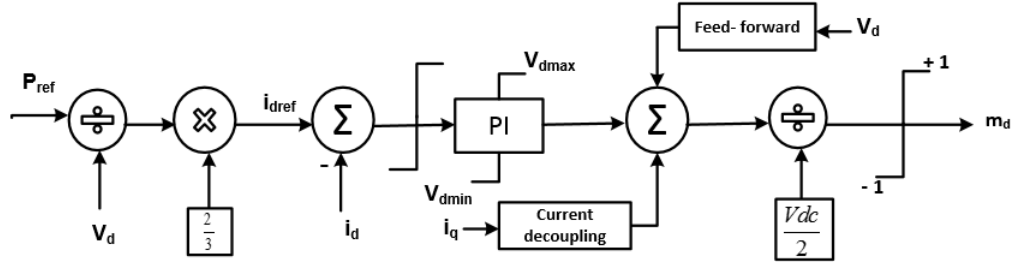


Figure 5.9: Direct axis current regulator with current reference set from power reference

5.1.3 Simulation Results and Discussion

The system in Figure 5.1 was implemented in the alternate transient program. The response of the system was tested by simulating cases with solar irradiation change

and ac load changes. Time is scaled such that each two seconds in the time axis represents an hour in the day time; where the day is assumed 12 hours from sunrise to sunset.

5.1.3.1- Irradiation change

Due to the variability in the PV output, the system operators often backup generators. This need can also be met by having energy storage interconnected to the grid or by taking advantage of diverse locations of renewable energy sources. For example, the California ISO has a real-time western regional energy imbalance market system which can integrate between wind, solar and tidal energy sources when available [68].

A battery energy storage systems (BESS) can play a significant role with the solar power sources because it can stabilize the response to sudden changes in solar irradiation. When the irradiation changes due to sunlight variation due to passing clouds, the output power of PV will change as well. The following scenarios are evaluated.

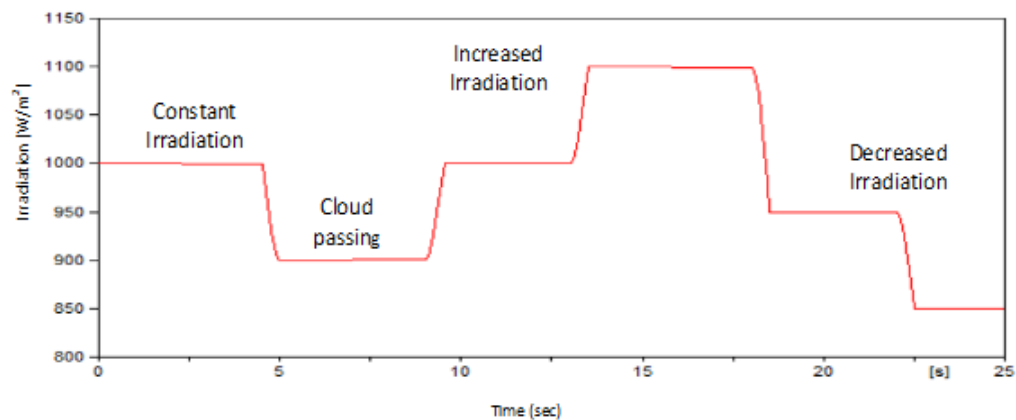


Figure 5.10: Solar irradiation variation versus time

- **Constant irradiation affected by weather conditions**

In this scenario the PV array is at a locality where the clouds are passing, thus making the irradiation of the PV array fluctuate. This scenario was captured in Figure 5.10 to show the system response under this variable generation condition. For example, at the start, the sun is bright, and the solar irradiations approach 1000 W/m^2 producing 2.6 MW, which would cover the connected load. The battery will be in standby-mode. When the clouds pass, the PV irradiation decreases to 900 W/m^2 and power output falls to 2.316 MW. As a result, the power demand is not equal to the power supplied, which lowers the voltage at the DC link. The battery delivers power to cover the shortfall as a secondary effect of balancing the voltage in the DC link. The battery discharged at 286.7 kW, instantaneous power, and the SOC is reduced to 73.7% after 5 seconds, when it was initially at 83%. After 5 sec, the irradiation goes back to initial condition of 1000 W/m^2 and the PV power rises back to 2.6 MW. The battery goes back to standby mode, and the SOC remains constant until there is another change in condition.

- **Increasing irradiation**

In afternoon, the sun gets brighter, the solar irradiation increases to 1100 W/m^2 , and the generated PV power increases to 2.896MW. The load condition is constant at 2.6MW. The battery converter controller will enter buck mode operation to store the extra power. The battery will draw power, balancing the system. The SOC will increase from 73.7% to 80%, with battery power at -292.1 kW, where the negative value indicates that the battery is charging as shown in Figures 5.11 and 5.12.

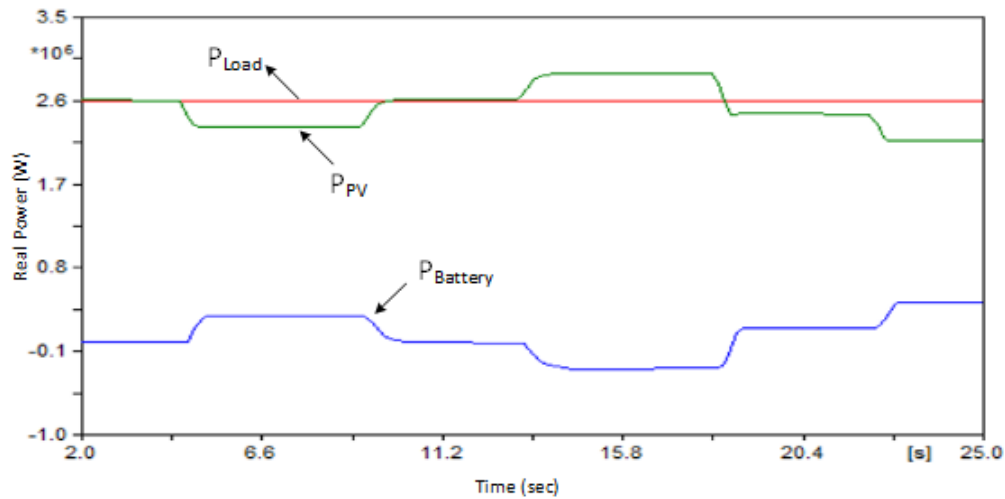


Figure 5.11: Real power for the PV, load, and battery during irradiation change

• Decreasing irradiation

In the evening, the sun is dimmer, and the solar irradiation is reduced to 950 W/m^2 , which decreases the generated power to 2.46 MW. This will result in a shortage of power to cover the load demand. Consequently, the boost converter will operate, and the battery will supply power to fulfill the load requirements. In addition, the SOC will decrease from 80% to 77.5% and the battery will discharge at 143 kW as shown in Figure 5.12. At the end of the day, the sunlight will reduce further, and the irradiation will drop to 850 W/m^2 . The generated PV power will decrease to 2.17 MW and the battery will be discharging and reach a level of 286.7 kW. The SOC decreases until solar irradiation reaches the load demand the next day. Figures 5.11 and 5.12 illustrate this response.

5.1.3.2 Load change

PV without storage is a non-dispatchable source. To demonstrate the ability of the PV system combined with storage to maintain a desired level of output as irradiation or load change, the inverter P_{ref} was varied to imitate the process of dispatching at

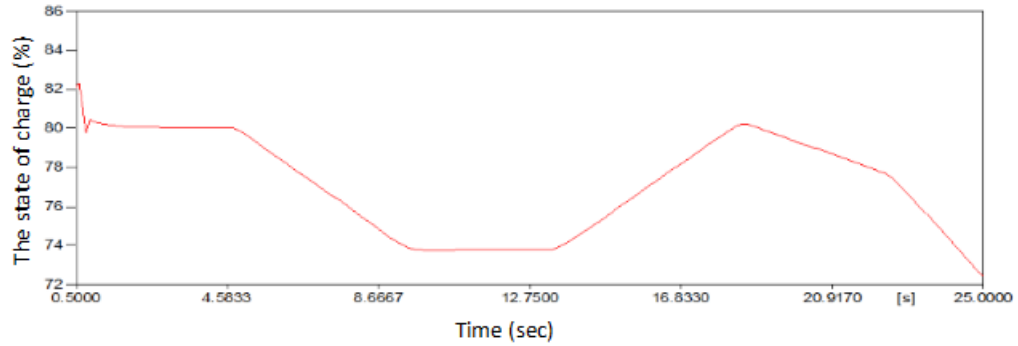


Figure 5.12: The SOC of the battery in response to irradiation changes

the request of the power grid operator. This case is used to verify the response of the BESS to load changes while the PV generation is kept constant. The change in P_{ref} causes the inverter power to vary. A change in dispatch is represented by changing P_{ref} for the inverter. The cases below show the change in P_{ref} in different time divisions for different scenarios.

- **Constant Load**

In the case of constant load, the PV output power equals the commanded ac power, and the DC link voltage will remain constant. As a result, the battery will not supply or absorb real power. This case is shown in Figure 5.13, and represented during the intervals $t = [2 - 5]$, $[10 - 15]$, and $[20 - 25]$ sec.

- **Response to Changes in P_{ref}**

In this case, the PV output power remains constant. When the PV output is unable to cover the command power reference, the battery enables balanced operation. When the load is increased, the battery will discharge to cover the demand. The total output power will be the sum of input power from the PV and battery. From Figure 5.13, we see that the PV power is 2.604 MW and output grid power is 2.898 MW, therefore we have about 300 kW shortfall of power and that will be met by the battery power.

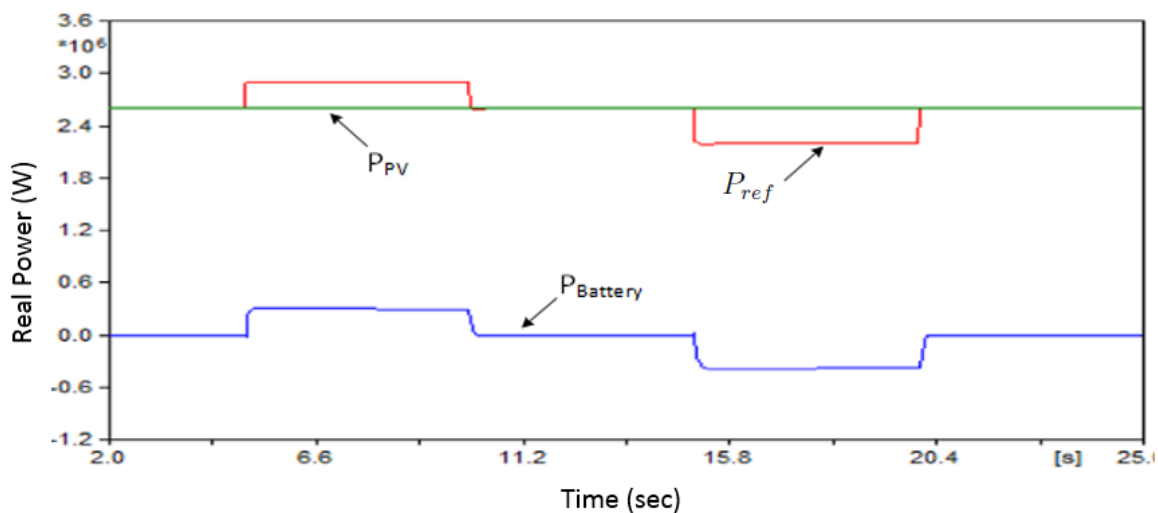


Figure 5.13: P_{ref} , P_{PV} and $P_{Battery}$ in response to dispatch changes

When the PV generated power is more than the total load, the battery will absorb the extra power. As a result, the bidirectional converter would switch to a buck converter when $t = [15 - 20]$ seconds in Figure 5.14. The PV array is generating 2.601 MW and P_{load} is 2.198 MW. This extra PV power of 398.1 kW will be stored balancing the DC link voltage.

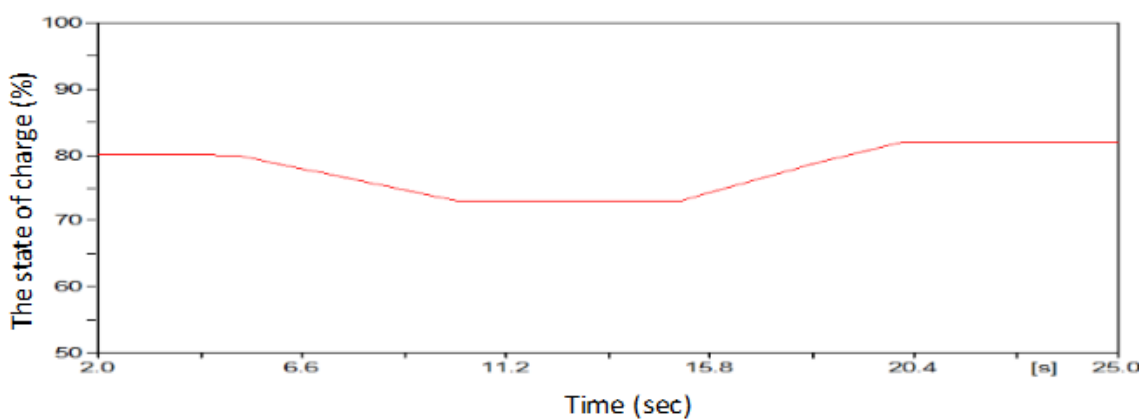


Figure 5.14: The SOC of the battery during P_{ref} changes

5.1.4 Conclusion

A change in irradiation or a change in inverter dispatch produces a power mismatch which causes the dc link voltage to change. Using bidirectional buck and boost converters can enhance the system resiliency by allowing the battery to charge or discharge according to the system requirement. A system model was developed in a power systems transients program and simulation cases were used to test the proposed system. Power electronic converters with advanced controls make renewable energy sources more reliable and they allow islanded system to operate for short time periods without backup generators.

5.2 Energy Management of a Battery Combined with PV Generation (paper 2)

5.2.1 Introduction

Renewable energy such as tidal energy, wind energy and photovoltaic are expanding beyond just being an area of research and to be sources of energy for the power grid. These renewable energy sources combined with power electronics have specific advantages when compared to conventional power generation [57]. Improvements in power electronic converters have made real time power response for grid demand possible. They do not require fuel and operate without green gas house emission [70]. Interfacing significant quantities of PV generation in a real grid is a very challenging task. Changes in the irradiation and temperature changes make the output characteristic of PV non-linear. The PV generation system can attain maximum power production for a given level of solar insolation if the Maximum Power Point Tracking (MPPT) technique is employed. This makes the MPPT techniques important in renewable energy implementation [58]. Renewable power sources like wind or solar may not be

available all the time, causing inconsistent generation and requires reserve generators to meet power demand. Power generation companies are experiencing challenges to make the renewable energy sources the predominant generation source. One possible solution to this challenge that has been studied for decades is the integration of Battery Energy Storage Systems (BESS) to the grid [56].

BESS is used in some distribution systems and especially in regions with high residential PV generation. It can play a vital role in the stability and reliability of the power system, in the sense that it supplies needed power when the external grid is unavailable or when the power generated by PV is insufficient due to inadequate sunlight. When the output power from PV varies, then a battery on the PV inverter dc link can supply or absorb power from or to the grid to maintain a constant dc link voltage and help stabilize the grid [56, 70]. Batteries with larger capacity have long life cycles and are typically very expensive. The life cycle of batteries is affected immensely when the battery is discharged at a current greater than its rated value or when it is charged at a current higher than the rated value. Selecting batteries with adequate maximum capacity and moderate discharge rate can help mitigate this challenge. This ultimately improves the performance and lifespan of the battery [53, 61]. The aim of this paper is to extend the lifetime of the battery by ensuring that it operates only when the need arises. By so doing, we will be able to stabilize the dc link voltage and reduce fast change or discharge of the battery.

When the inverter ac power reference of PV output power changes, causing the voltage at dc link to decrease or increase depending upon the balance of supply and demand. This causes a lot of charging or discharging [on and off] operations and this can be controlled by using the concept of hysteresis. The voltage needs to be regulated within a hysteresis band. If the range of the hysteresis is too small, then the battery will switch in between charge and discharge mode too often. Conversely, if the hysteresis value is too large, then the bidirectional controller will take a great

amount of time to respond [1].

5.2.2 System Architecture

As shown in Figure 5.15, the power system modeled here consists of the following components: PV model, MPPT controller, Boost converter for PV, BESS, Bidirectional DC/DC converter for the battery, a DC/AC converter, which are connected connects to the IEEE 7-bus power system. These models were built and tested with varying parameters (to evaluate stability) in the Alternate Transients Program (ATP) environment along with their corresponding control circuits, as explained in the following sub-sections.

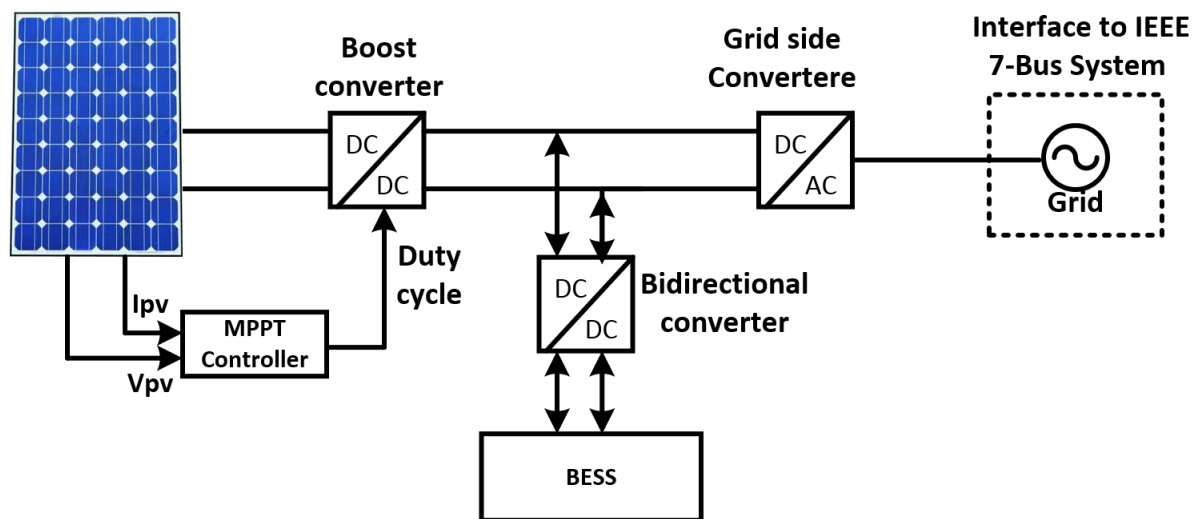


Figure 5.15: The Schematic Diagram of the Study Power System

5.2.2.1 Model of a Photovoltaic Cell

The PV cell generates a dc voltage (V_{pv}) under solar radiation. The quality of PV generation depends on the area of semiconductor material used in PV cell. The generated PV voltage is low, and it must be brought up to the input level of inverter or load through series connection of cells [58]. The performance of the output energy from PV modules is expressed in Wh/m^2 , while the total output power is represented

in Watt (W). A PV cell can be represented by an equivalent circuit of its series resistance (R_s), parallel resistance (R_p), and one diode connected anti-parallel with light generated by the equivalent current source as shown in Figure 5.16. The mathemat-

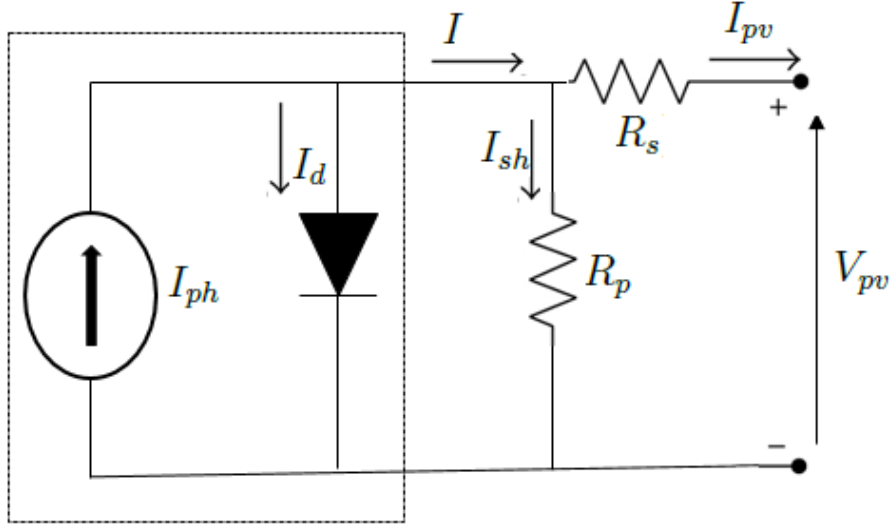


Figure 5.16: Ideal Single Diode PV Model

ical model of an ideal PV cell can be described through the I-V characteristics curve theory of semiconductors [57, 71]. The basic equation showing the output current I_{pv} of a PV array module is expressed in equation (5.4)

$$I_{pv} = I_{ph} - I_d - \frac{V_{pv} + (I_{pv}R_s)}{R_p} \quad (5.4)$$

Details of the I_{pv} calculations can be found in [1, 62].

5.2.2.2 Modeling of MPPT

At any given instant of time, maximum power can be extracted from the PV array by biasing the PV cell much like any other diode, and is here aided using MPPT. The basic operation of PV depends on the voltage and current with respect to the power. A closed loop control can be applied to the PV array to keep it at the best

voltage with respect to the maximum power which is called Maximum Power Point (MPP) [58]. The solar irradiation changes with time which causes variation in other

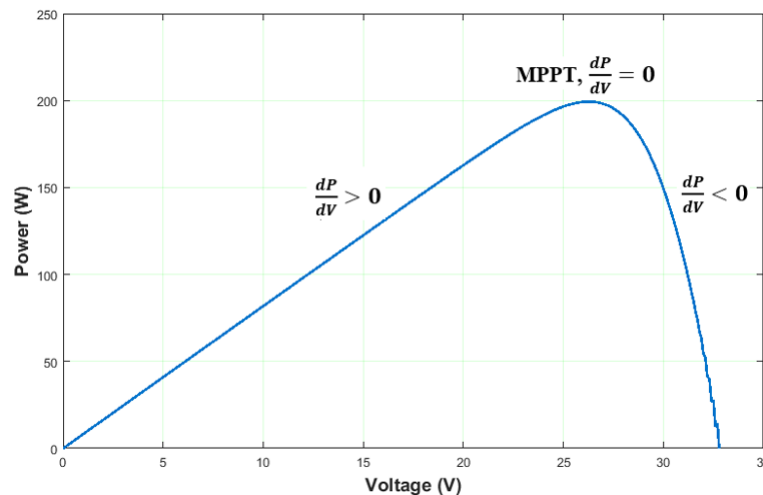


Figure 5.17: MPPT Function Based on P&O Method

physical quantities like environmental temperature and solar cell temperature, which all combine to cause the MPP to change. The MPPT algorithm tracks those variations in the MPP to get maximum output from the PV.

The Perturb and Observe (P&O) method is used here due to the following advantages. The MPPT can have fast tracking when the perturbation is large and the needed accuracy is low. However, MPPT can have high accuracy and take a long time to track the MPP when the perturbation is small. Thus, the variable perturbation can be used to improve that as shown in Figure 5.17. P&O algorithms work by taking measurements of both the terminal PV voltage and the PV current by adding small voltage disturbances [60].

The Figure 5.18 illustrates operation of the P&O method algorithm. The MPPT algorithm decreases or increases the boost converter duty cycle to track the new MPP.

When the PV array is connected to a load or distribution system, the output PV voltage level is not the same as that of the grid voltage at dc/ac converter dc link. A boost converter is applied to match the voltage level to the desired dc link rating. With the aid of the boost converter, a controlled current source obtained

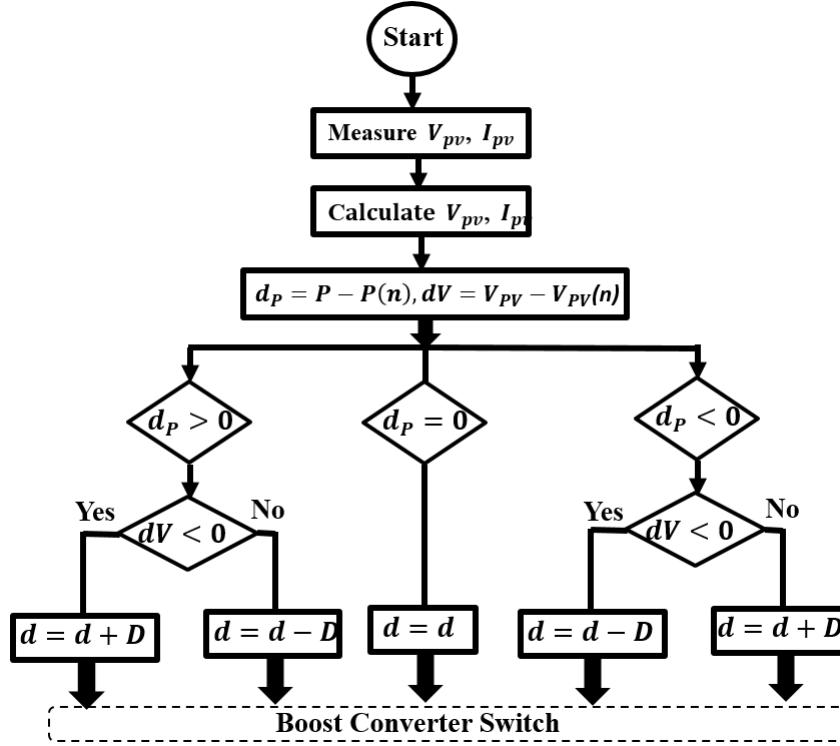


Figure 5.18: The P&O method algorithm

from I_{pv} is connected to the converter dc bus. In this application, the dc link voltage is controlled by the battery controller. By controlling the duty cycle of the boost converter, the maximum voltage of the V_{pv} can be tracked effectively. More details on the mathematical model of the boost converter are presented in [58, 62].

5.2.2.3 Modeling of Battery

The battery model implemented in this paper uses an equivalent circuit model for dynamic power simulation rather than electrochemical or experimental based models. The generic battery model of a Lithium-Ion battery was used in this paper, in which the battery works as a controlled voltage source [56]. The actual simulation was carried out using ATP. This battery model is made up of a voltage controlled source connected with a series resistance as shown in Fig 5.19.

The equation of Lithium-Ion model during discharge and charge modes is shown

in equation (5.5)

$$V_{Batt} = E_0 - Ri - K\left(\frac{Q}{(Q - it)}\right)i^* + Ae^{(-B \cdot it)} \quad (5.5)$$

Where E_0 is no load constant voltage (V); B is exponential capacity $(Ah)^{-1}$; K is polarization voltage constant (V); i^* is low frequency part of the current dynamics (A); i is current of the battery (A); it is extracted capacity (Ah); Q is the capacity of the battery (Ah); A is exponential of voltage zone amplitude (V); R_b ; Internal resistance (ohm); and V_{Batt} terminal battery voltage.

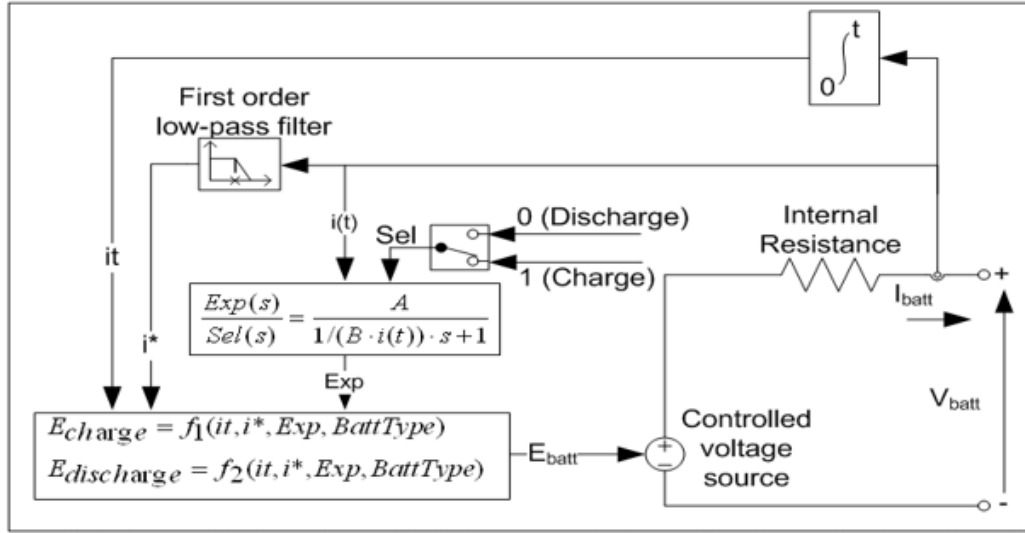


Figure 5.19: The Equivalent Circuit for the Battery [68]

Some assumptions are made to work within software limitations, which includes: the parameters for both discharge and charge can be assumed to be the same, battery sizing is not calculated, the effect of temperature on the battery model is neglected for both discharging and charging the battery, and the internal resistance value of the battery is constant and does not change [1, 68].

The state of charge (SOC) plays an important role in the lifespan of the battery. The SOC increases with charging and decreases with discharging as per energy conservation law. The upper SOC for the battery model used here is set at 85% and

with 25% as the lower limit, which can be calculated with equation (5.6):

$$SOC = 100\left(1 - \frac{1}{Q} \int_0^t i(t) dt\right) \quad (5.6)$$

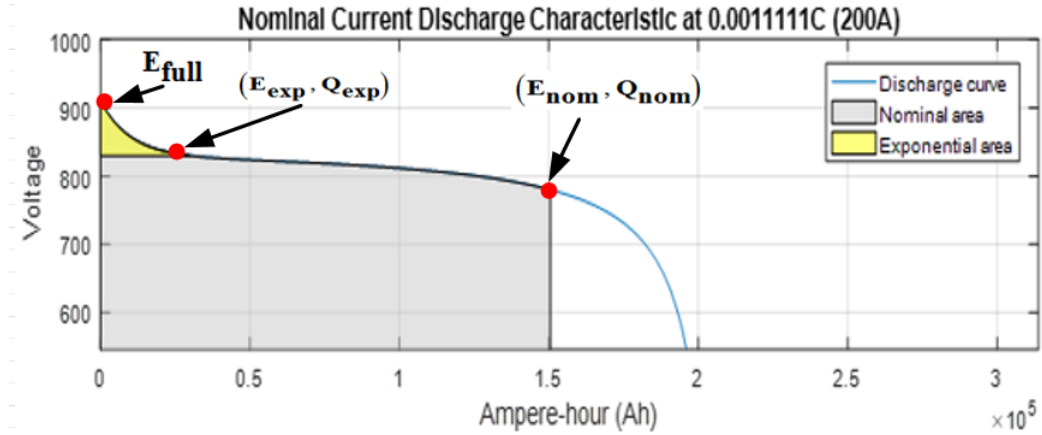


Figure 5.20: Discharge Characteristics Curve of the Battery

Figure 5.20 shows the battery characteristics during discharge. The parameters were calculated using three points in the figure; fully charged voltage E_{full} , end of exponential capacity zone (E_{exp}, Q_{exp}) and nominal zone related with nominal capacity (E_{nom}, Q_{nom}) [68]. As shown in this figure, there are three areas that describe the discharge characteristics of the battery. The first area which is narrow, represents the exponential voltage drop characteristic of the battery when fully charged. The second area represents the charge that can be drawn from the battery until its charge drops to below the nominal voltage of the battery. Finally, the last area indicates a rapid drop of the voltage when the battery discharges totally.

The implemented parameters in this paper are shown in Table 5.1 are obtained by the rated capacity and the internal resistance. The battery parameters were derived from the discharge characteristics curve in (5.5).

Table 5.1: The Parameters of the Battery

Description	Name	Values	Unit
Fully charged voltage	E_{Full}	910	Volt
Exponential voltage	E_{Exp}	830	Volt
Nominal voltage	E_{nom}	780	Volt
Nominal capacity	Q_{nom}	150500	Ah
Exponential capacity	Q_{Exp}	30000	Ah
Internal resistance	R_{in}	0.016667	Ohm
Rated capacity	Q	180000	Ah

5.2.2.4 Bi-Directional Buck/Boost Converter (BDBBC) and control scheme for the battery

A main objective of the battery is to regulate dc voltage while maintaining control of injected power. The voltage reference at dc link can be kept higher compared to the voltage of the battery bank. In this paper we considered the terminal voltage at the battery be around 900 V, while $V_{dc}^* = 1500$ V. Let's suppose the battery SOC is 85% with condition that the battery can supply 2.6 MW power at rated capacity for an hour, if there is no PV irradiation. The battery discharge rate is given by equation (5.7) [68].

$$\frac{2.6MW * 1hr}{900 * 0.85} = 3.4kAhr \quad (5.7)$$

The battery bank is connected to the dc link using BDBBC as shown in Figure 5.21.

The converter consists of two switches S1 and S2 which allows the converter to work on two control modes, buck or boost ,depending on direction of energy flow. The control system for the BDBBC consists of two controls; an outer controller, which is

block. It compares the reference current output for the outer control loop with the measured current of the AC system, and uses the PI controller to generate dq reference frame voltages references in the process. This voltage is summed up with both feed-forward and current decoupling components, and scaled with dc voltage to obtain the modulation functions m_d and m_q [18, 53].

5.2.3 DC Link Voltage Regulation Under Margins

Changes in irradiation and temperature cause a proportional change in both the dc link voltage as well as changes in power injected to the grid load. The BDBBC can control the battery by charging and discharging to meet the inverter power reference. This allows the inverter dc link to be regulated and maintain power stability between the PV generated power and ac load demand [65]. Voltage regulation in the dc/ac converter dc link is necessary because the electronic devices may become damaged if the voltage at the dc link is significantly higher than the reference voltage. Also, if the voltage drops lower than V_{dc}^* , then the operation of the chopper and the converter circuits will be affected [71]. The control of the dc link voltage should operate as buck or boost converter at rated voltage, $V_{dc_{max,on}}$ and $V_{dc_{min,on}}$ for discharging or charging the battery. The battery energy management scheme is shown in Figure 5.23 and explained below.

- When the generated power from PV is higher than the power needed at the grid, then the voltage at the dc link will increase until it is higher than $V_{dc_{max,on}}$. At this point, the control topology makes the BDBBC operate in buck mode allowing charging the battery. Charging the battery makes the voltage at DC decline until it becomes equal to or less than $V_{dc_{max,off}}$. Then the BDBBC stops charging the battery.
- When the power transferred to the grid is higher than the generated power

from PV, then the dc voltage decreases and keeps decreasing until it reaches $V_{dc_{min,off}}$. When the voltage at the dc link becomes less than $V_{dc_{min,on}}$, the control scheme allows the BDBBC to operate in boost mode and discharge to battery. When the boost mode starts, it increases the voltage at the dc link until it is equal to or higher than $V_{dc_{min,off}}$. The boost stops and the battery stops discharging [1, 61].

- The hysteresis energy management aids the elongation of the battery's lifespan because the battery only operates when the threshold voltages $V_{dc_{max,on}}$ and $V_{dc_{min,on}}$ are exceeded.

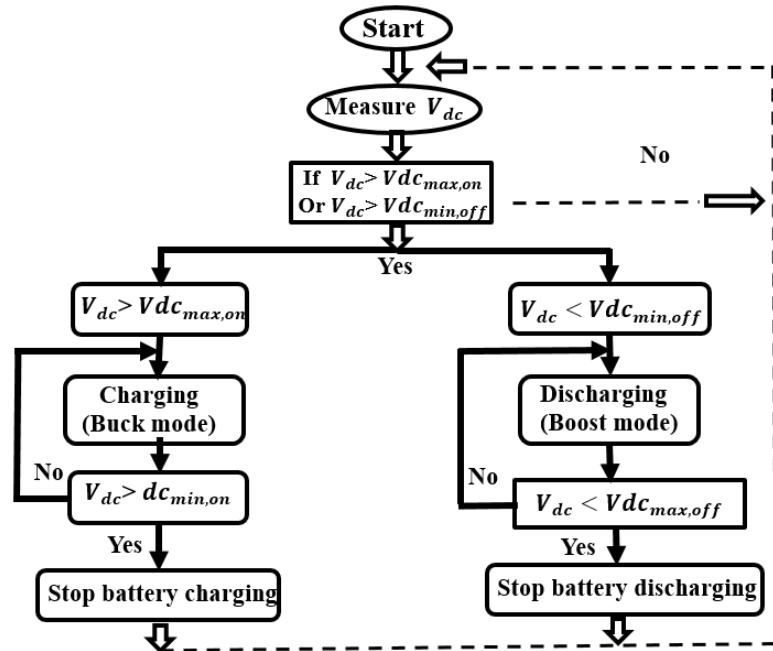


Figure 5.23: The Energy Management Algorithm (Hysteresis) for the DC/AC Converter

5.2.4 Simulation Results and Discussion

The system of Figure 5.15 was implemented and tested in the transient program to observe changes in the dc link voltage as solar irradiation varied as shown in Figure

5.24. Time is scaled assumed that each two seconds in the time axis represents an hour in the day; where the day is assumed to have 12 hours from sunrise to sunset.

The model is investigated the output of hysteresis control algorithm for the battery management system under three conditions, when the PV generation is higher, lower and equal to the grid load. In the model the set point for the ac voltage at the grid side is 690 V and hysteresis control limits of the dc link voltages for upper threshold are $V_{dc_{max,on}}$, $V_{dc_{max,off}}$ as 1510 V and 1505 V respectively. For the lower threshold $V_{dc_{min,on}}$, $V_{dc_{min,off}}$ are 1490 V and 1495 V respectively.

The PV generation varies with respect to changes in solar irradiation as shown in Figure 5.24, As a result, the voltage at the dc link will also vary. When the voltage exceeds the threshold the battery responds to limit the bus voltage variation. The outer voltage control of the BDBBC uses a PI controller to regulate the voltage at dc link.

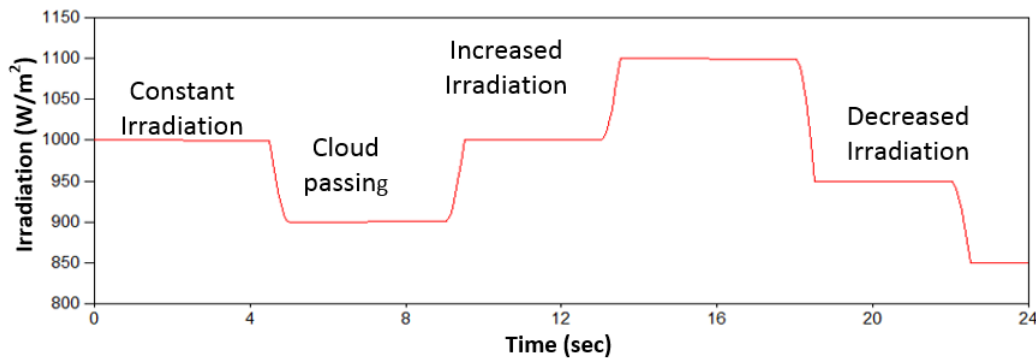


Figure 5.24: Irradiation Change

Initially from 0-4.5 sec, the PV power is equal to the ac output power as shown in Figure 5.25 while the DC voltage is about 1500 V. Figure 5.26 shows the variations of the voltage at the dc link. The voltage at dc bus is within the hysteresis range while the battery is not changing or discharging at this point.

Beyond 4.5 sec, the power generation of the PV starts decreasing due to reduced solar irradiation. This causes the voltage at dc link to be depressed. As soon as the dc voltage crosses the preset minimum threshold of $V_{dc_{min,on}}$ the boost mode turns

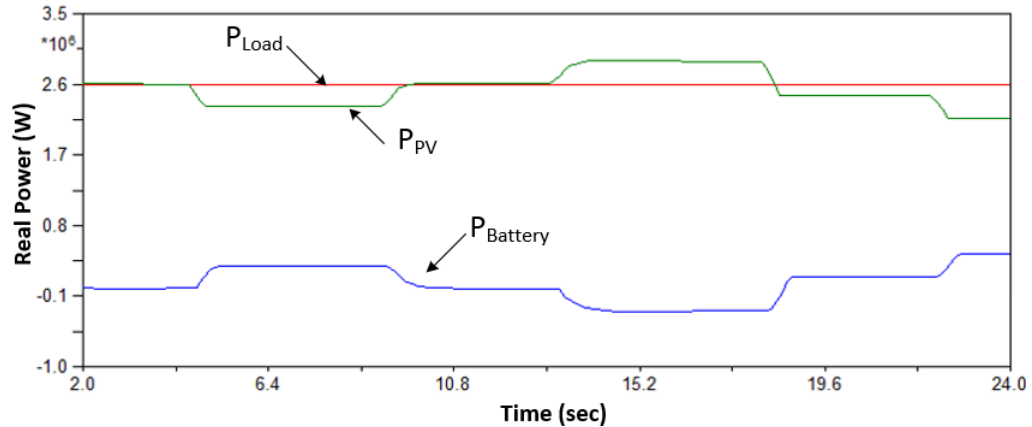


Figure 5.25: The Real Power of the PV, Load, and Battery During Irradiation Changes

on and supplies stored energy to maintain the dc link voltage. Because the battery discharges 287.2 kW instantly into the grid side, the SOC will reduce from an initial value of 85% to 75.7% as shown in Figure 5.27.

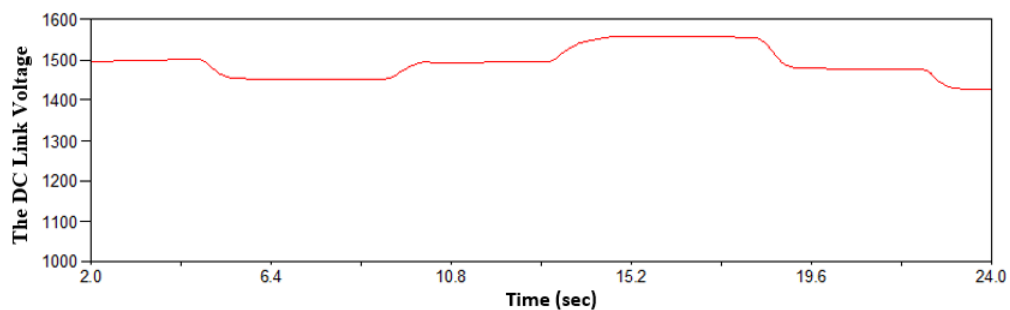


Figure 5.26: Voltage at the dc Bus During Irradiation Changes

The PV generation comes back to the normal operation at 9.5 sec, during which the power generation of the PV is equal to the ac power. The voltage at the dc link starts increasing until it touches the preset maximum upper threshold of $V_{dc_{min,off}}$ at which point the boost mode turns off. The battery stops discharging at that instant with the SOC at 75.7%. The threshold limit can be set according to the battery size and discharge rate to ensure that the battery works only when required.

As can be observed in Figure 5.25, beyond 13.5 sec the power generation of the PV rises above the ac load power, thus increasing the voltage at the dc link. When

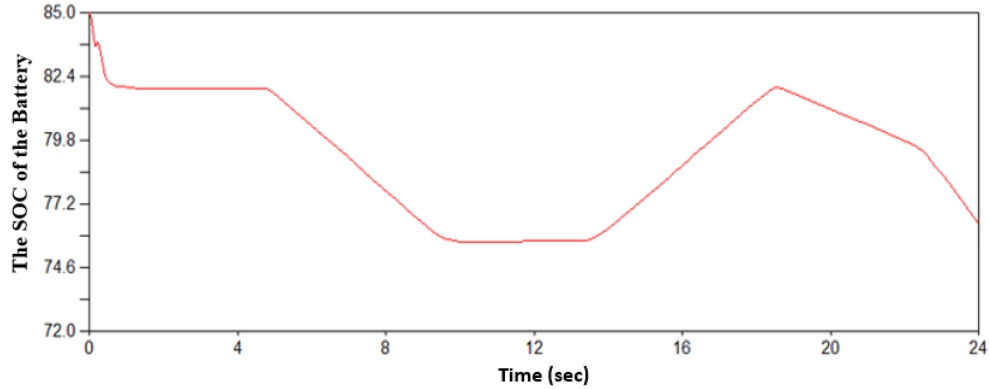


Figure 5.27: The SOC of the Battery

the dc link voltage crosses the preset maximum threshold $V_{dc_{max,on}}$ the buck mode turns on and the battery absorbs the extra energy in order to maintain the dc link voltage. The battery power goes to -293.3 kW following a ramp (the negative sign is an indication that the battery is charging) as shown in Figure 5.25.

The irradiation starts to decrease after 18 sec, causing the PV power generation to decline below the required load power. This prompts the voltage at the dc link to start decreasing until it touches the below threshold $V_{dc_{max,off}}$, at which point the buck mode turns off. The voltage at dc continues decreasing until it crosses the $V_{dc_{min,on}}$ limit, when the boost mode turns on to make the battery discharge with the power rate 143 kW over a ramp and the SOC decreases to 79.4%. After 22 sec, the PV generated power continues to decrease together with the dc link voltage. This causes the battery to discharge progressively at an increased rate of 431 kW with higher current. The SOC continues to decrease to 76.4%. The PI controller can keep the voltage at the dc link close to the threshold voltage set by the user.

At $t=0$ the voltage at the dc link is equal to the V_{ref} , therefore the battery's output current is zero. The battery starts discharging with 320 A from $t = 4.5 - 9.5$ sec, as shown in Figure 5.28. This is due to the decrease in the solar irradiation as shown in Figure 5.24. Similarly, the battery discharges at 155.7 A and later increases discharging 486 A from 18.5 to 22 sec and 22 to 24 sec respectively. Alternatively,

the battery is taking current, thus charging with -313.3 A from time 13.5 to 18.5 sec as shown Figure 5.28.

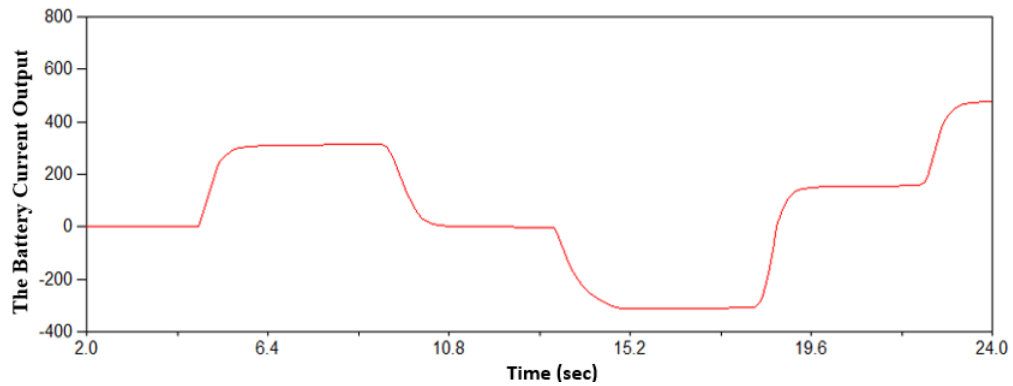


Figure 5.28: The Battery Current During Charging and Discharging

The battery voltage is initially 930 V as seen in Fig 5.29. During charging and discharging the battery's terminal voltage changes correspondingly. When the battery starts discharging the terminal voltage of the battery is decreased, while when the battery is charging, the battery terminal voltage increases, based on equation (2).

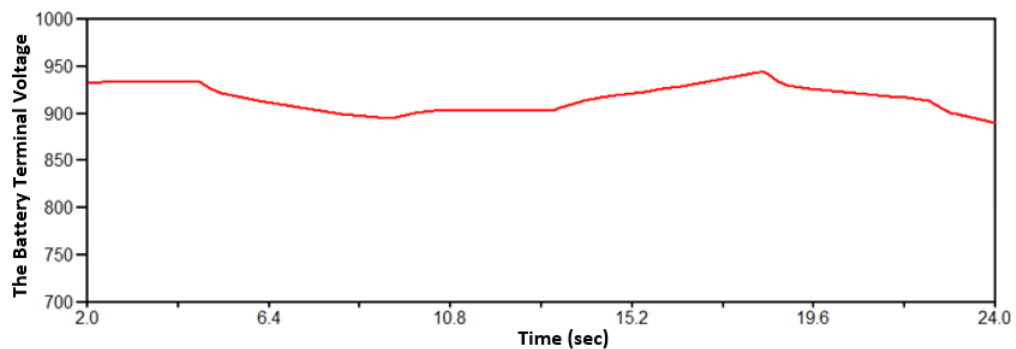


Figure 5.29: The Battery Terminal Voltage During Sequence from Figure 10

5.2.5 Summary and Conclusion

By using the energy storage integrated on a PV converter dc link, the PV performance on power grid can be enhanced. A dc link energy management scheme was presented. The energy management system that was used in this paper to regulate the controller of the battery interface converter works between buck and boost modes. Ramp limits

are applied to reduce stress on the battery and increase lifespan. A system model was developed in a power systems transients program and simulation cases were used to test the proposed system.

Chapter 6: Synchronous generator and Virtual synchronous generator design control and models

This chapter consists of material from two papers, the first paper is published in the proceedings of the IEEE Texas Power and Energy Conference (TPEC) from February 6-7, 2020. And the second paper is published in the proceedings of the IEEE Innovative Smart Grid Technologies (ISGT) Conference held in Washington, DC from February 17-20, 2020.

6.1 Implementation of Emulated Inertia using PV Generation with Energy Storage to Improve Integrated Grid Response (paper1)

6.1.1 Introduction

As renewable energy such as photovoltaic and wind turbines generation becomes more common, there are several great challenges to design, implement and integrate them into the existing power grid without compromising system stability [4]. The overall system inertia is drastically reduced with the integration of these renewable energy sources when they are controlled to track peak power. While the traditional synchronous generating plants has large rotating components that provides adequate generating inertia, the typical renewable energy sources (e.g. PV) has little or no inertia [4] and [45]. When the rotational inertia is low in the power system, the frequency dynamics are faster and it becomes challenging to control frequency and operation of the power system. Due to the control schemes implemented in power electronic devices in coupling the renewable energy units to the existing system, the inherent inertia provided by the conventional generating units offset by the renewable power generation cannot be easily compensated by the renewable sources unless some special measures are taken, thereby increasing the complexity of operating the power

system as a whole [39]. Furthermore, due to the typical control algorithm that optimizes real power output, power-electronic coupled generation, such as photovoltaics, are limited in their ability to supply reactive power to stabilize power system voltage. [32].

Renewable energy combined with power electronic interfaces has some advantages, which includes small output impedance, fast response of active and reactive power control, providing potential for the participation of distributed energy in the frequency and voltage regulation of the distribution and transmission networks [4]. To mitigate the negative impact of renewable energy sources in the existing traditional power grid, energy storage can be employed to provide artificial inertia to the grid. Frequency control is possible if an additional control path is added, allowing an inertia response to be emulated. Without this additional control, the frequency support deteriorates [32]. When additional energy storage control is implemented, the frequency support is further improved. Using this strategy, conventional rotating machines and the renewable energy generation would exhibit similar grid characteristics. This makes the participation of the renewable energy in the frequency control of the power system plausible. In the same vein, the existing power electronics interfaced sources can also provide some ancillary services such as voltage regulation, thereby improving the stability of the power system [32] and [72]. Some of the renewable energy sources that do not have inherent inertia and damping can be controlled to emulate a Synchronous Generator (SG) by adding a virtual synchronous generator (VSG) controller. A VSG generally consists of renewable energy sources combined with storage energy plus one or more power converters and a master controller. The VSG control can provide frequency droop in the grid and damping support for grid oscillations. These behaviours are dynamically the same as the conventional SG [46].

In this paper, virtual inertia was incorporated into a PV system with battery energy storage to enhance grid stability. This virtual inertia is provided by controlling

some renewable energy sources to act as VSGs. The dynamic behavior of synchronous generator is represented by the fundamental swing equation to produce virtual inertia. The parameters of the VSG are controlled in order to improve the system's response, unlike in a real synchronous machine [46].

6.1.2 System description

As shown in Figure 6.1, the power system model consists of a PV system model, MPPT control, a boost converter for the PV system, a BESS, a bidirectional DC/DC converter, and VSG control for the dc/ac converter. These models are built as modules in an EMTP type program environment as explained below.

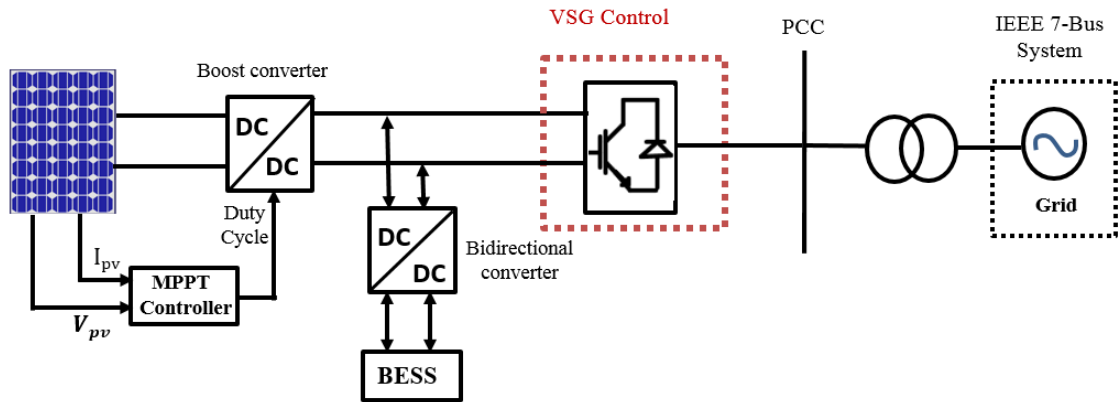


Figure 6.1: The schematic diagram of the power system used in this paper

6.1.2.1 PV modeling

A PV cell generates a dc voltage (V_{pv}) under solar radiation. The PV generation depends on the semiconductor material used in PV cell and the area of the cell. The PV cell modelled in this paper is represented by an equivalent circuit which consist of series resistance (R_s), parallel resistance (R_p), and a diode connected in parallel with a current source that represents the sunlight generation, while I_{PV} and V_{PV} represent

the solar cell terminal output current and voltage respectively, as shown in Figure 6.2[58] and [72].

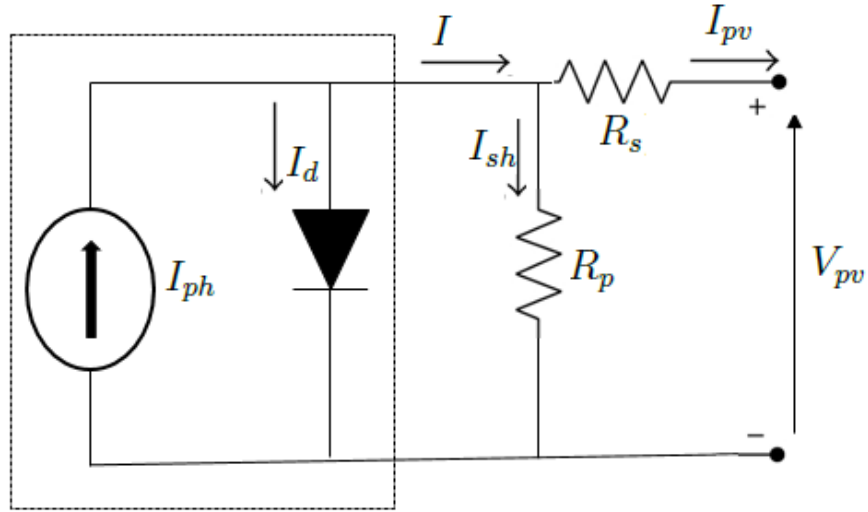


Figure 6.2: Ideal Single Diode PV Model

The mathematical model of an ideal PV cell can be described through the I-V characteristics curve theory of semiconductors [72]. The basic equation showing the output current, I_{pv} , of a PV array module is expressed in equation (6.1).

$$I_{pv} = I_{ph} - I_d - \frac{V_{pv} + (I_{pv}R_s)}{R_p} \quad (6.1)$$

Details of the I_{pv} calculations can be found in [63] and [72]. Due to the irregular nature of the solar irradiation, a maximum power point tracking (MPPT) control is essential to extract the maximum power from the PV array at a given time instance. The Perturb and Observe ($P\&O$) algorithm method is used to implement MPPT in this paper due to its high efficiency. A detailed description of the MPPT can be found in [63].

6.1.2.2 BESS Modeling

In this paper, a generic Lithium-Ion battery model is adopted. The dynamic simulation uses an equivalent circuit model rather than electrochemical or experimental models. The battery model is made up of a controlled voltage source connected behind a series resistance as illustrated in Figure 6.3 [53] and the specifications of the implemented BEES are shown in Table 6.1

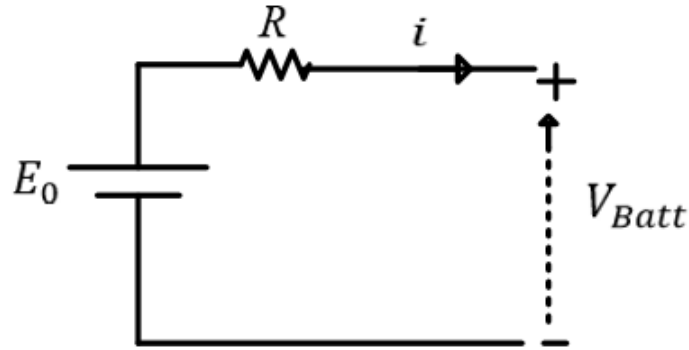


Figure 6.3: The equivalent circuit of the battery

Table 6.1: The Parameters of the BESS

Description	Name	Values	Unit
Fully charged voltage	E_{Full}	910	Volt
Exponential voltage	E_{Exp}	830	Volt
Nominal voltage	E_{nom}	780	Volt
Nominal capacity	Q_{nom}	150500	Ah
Exponential capacity	Q_{Exp}	30000	Ah
Internal resistance	R_{in}	0.016667	Ohm
Rated capacity	Q	180000	Ah

The inherent equation which applies to the charging and discharging operations of the Lithium-Ion model is given in equation (6.2)

$$V_{Batt} = E_0 - Ri - K\left(\frac{Q}{(Q - i_t)}\right)i^* + Aexp(-B.i_t) \quad (6.2)$$

A detailed description of the BESS is presented in [53] and [72]

6.1.2.3 VSG Control Modeling

An overview of the implemented structures of VSG control connected to the grid system is illustrated in Figure 6.4 and the implemented parameters are shown in Table A.1. This control is accomplished through the Voltage source converter that is linked to the power grid through a LC filter. Characteristics of the SG behavior were implemented using the traditional swing equation as additional controls for the VSC to allow the converter to provide emulated inertia [39] and [52].

The swing equation implemented in this study is shown in equation (6.3):

$$\frac{2H}{\omega_{syn}(t)} \cdot \frac{d^2\delta_m(t)}{dt^2} = P_{m.pu}(t) - P_{e.pu}(t) = P_{a.pu}(t) \quad (6.3)$$

Where:

$\delta_m(t)$ is the position of rotor angular (*rad*).

$\omega_{syn}(t)$ is angular velocity of the rotor (*rad/s*).

$P_{e.pu}(t)$, $P_{m.pu}(t)$ and $P_{a.pu}(t)$ respectively are the electrical, mechanical and accelerating power in pu.

H is the desired inertia constant.

This inertia control determines both the phase angle reference, θ_{VSG} , and angular frequency, ω_{VSG} , in the inner control loop of the inverter. In addition, the voltage reference amplitude, \hat{V}_{VSG}^{r*} , is used for a control loop to determine a reactive power reference. The controllers for the VSG and $|V|$ are represented as external loop that produce the voltage control and current control references. A Phase Locked Loop (PLL) is used to detect the measured frequency from the grid and this frequency is

used as an input to the swing equation as a damping term [18] and [1]. Each block from Figure 6.4 will be discussed in the following sections.

1- Active Power Control and Inertia Emulation for VSG

As represented in the block diagram in Figure 6.5, the angular speed of the VSG is defined as ω_{VSG} , while the phase angle θ_{VSG} is obtained from the integral of ω_{VSG} . The per unit (pu) frequency of the grid is estimated and tagged ω_{PLL} from the PLL [4] and [39]. In addition, the part of Figure 6.5 labelled APC is the droop control that represents the equivalent frequency response of a steady-state generator speed governor characteristic to control the VSG power [46].

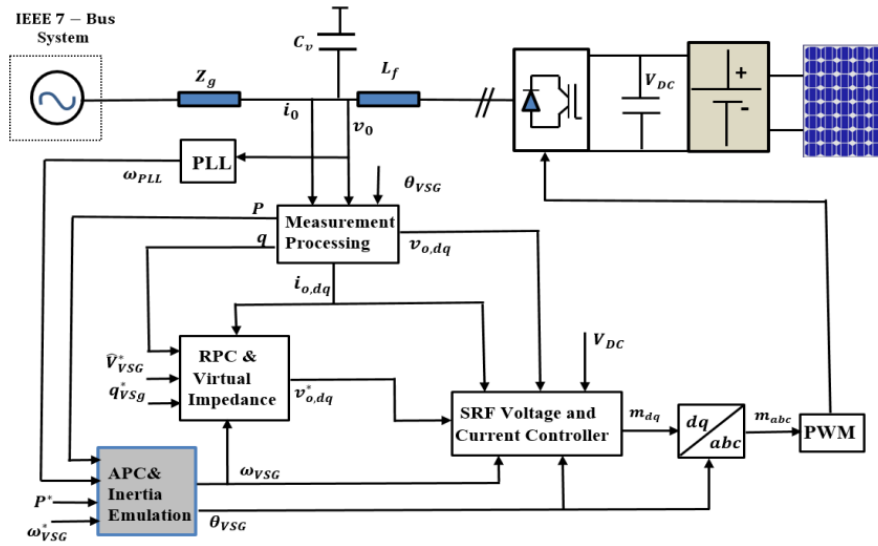


Figure 6.4: Simplified block diagram of VSG model

Equation (6.4) illustrates the VSG virtual speed deviation, $\delta\omega_{VSG}$, and introduces the virtual phase angle, $\delta\theta_{VSG}$. Also, this equation represents the effect of the power balance on the response of the swing equation implemented in the VSG model [4] and [39].

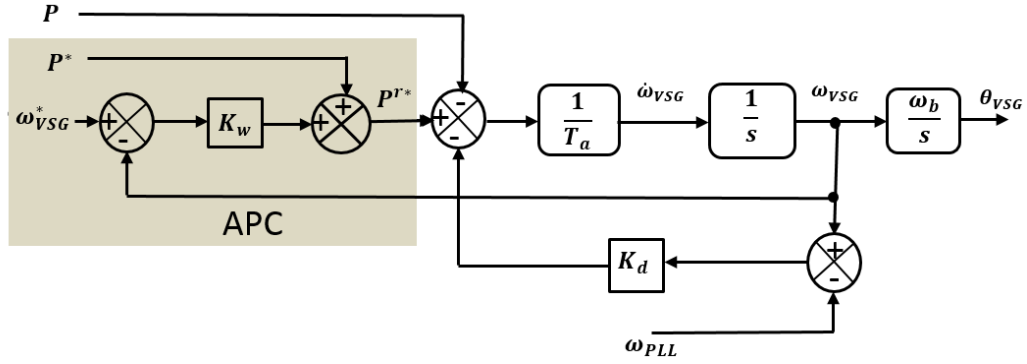


Figure 6.5: Active Power Control and Inertial Emulation Based on Swing Equation

$$\frac{d\delta\omega_{VSG}}{dt} = \frac{1}{T_a}(P^{r*} - P - K_d(\omega_{VSG} - \omega_{PLL}) + K_w(\omega_{VSG}^* - \omega_{VSG})) \quad (6.4)$$

Where:

K_d is the constant damping factor of virtual synchronous generator.

K_w is droop constant gain.

T_a is the inertia time constant of the VSG.

P is active power electrical measured from the grid (pu).

ω_{VSG}^* is the reference speed.

P^{r*} is the virtual mechanical power reference which mimics the SG's mechanical power.

2- Reactive Power Control and Virtual Impedance

The advantage of adding a Reactive Power Control (RPC) is that it enhances the stability of the grid voltage [46]. As shown in Figure 6.6, the output voltage reference, \hat{V}_{VSG}^{r*} , is used as input for the virtual impedance used to represent dynamic behavior in response to power system response.

Where:

q_{VSG}^* is the external reference of reactive power.

K_q is the droop constant gain in (pu).

$\omega_{f,VSG}$ is the filtered output of the measured reactive power in (pu).

The virtual impedance as shown in Figure 6.6 is used to adjust the VSG in steady state and provide dynamic response to the dynamic behavior of the system grid [46].

3- Cascade Voltage and Current Controller

The cascade voltage and current controllers of the VSG, which is sometimes referred to as a synchronous reference frame (SRF) voltage and current controllers can be seen in the Figure 6.7. They operate in the synchronous rotating dq-reference frame making it possible for the controllers to be of a simple PI type. The outer-loop voltage controller receives its reference via the virtual impedance reference and provides a current reference to the inner-loop current controller. The current controller in turn provides voltage modulation reference in the dq-reference frame. The reference is then converted into abc stationary frame by an inverse park/clark Park's transformation [52] and [73].

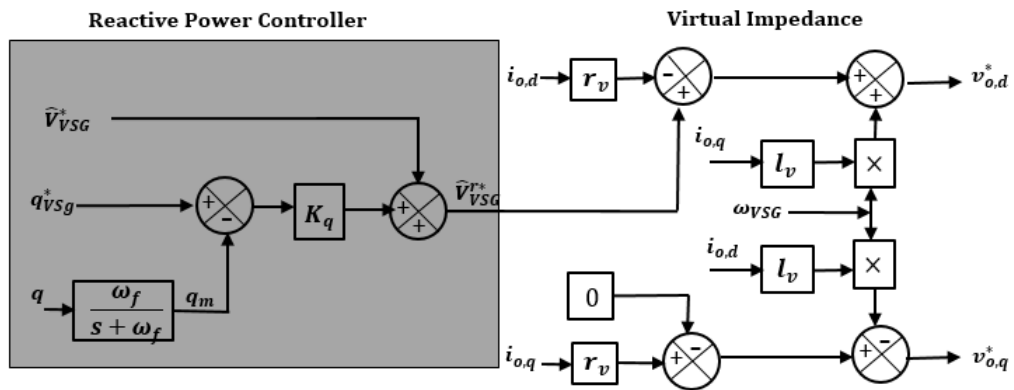


Figure 6.6: Reactive Power Control and Virtual Impedance of VSG

The PI controller of the current loop was tuned with modulus optimum method while the outer voltage loop was tuned using the symmetrical optimum method as implemented in [4] and [46].

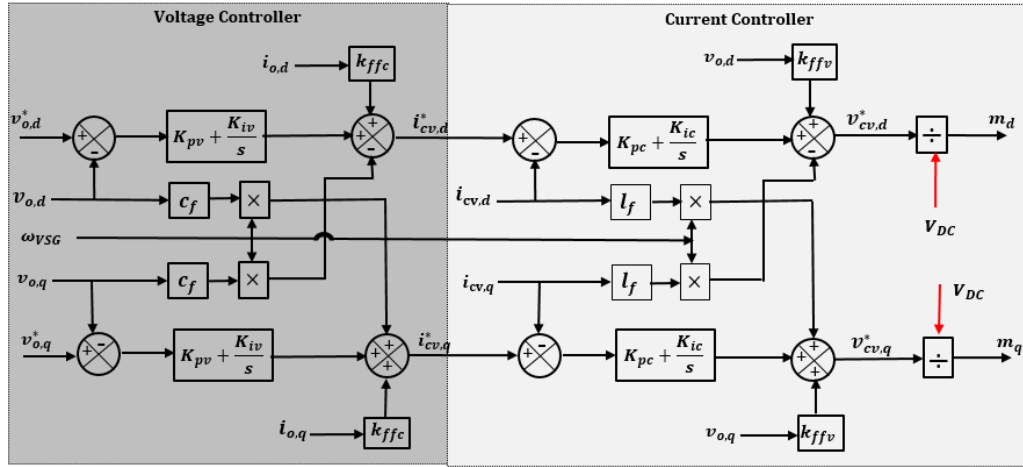


Figure 6.7: Voltage and Current Controller of VSG

6.1.3 Simulation Results and Discussion

In this paper, the base model shown in Figure 6.1 was implemented in ATP. The simulations were conducted under varying conditions to show how the proposed implementation can support the stability of a small grid. For the base model, the rated power of the VSC was set to 2.75MVA, while the rated ac voltage value was 690V ($V_{LL,RMS}$). The initial inputs and parameters of the model of VSG are specified as defined in [46]. Different cases were implemented and tested in this paper. This was achieved by varying the grid frequency, reactive power demand and controlled virtual inertia. The main goal is to demonstrate and explore the various properties and capabilities of the VSG under each case and its practical suitability toward providing inertia support for PV generation.

The variations mentioned above prompt the VSG controller to be activated so that the required voltage and power needed to damp the oscillation are generated. Results obtained from the simulation of these cases are presented and discussed below.

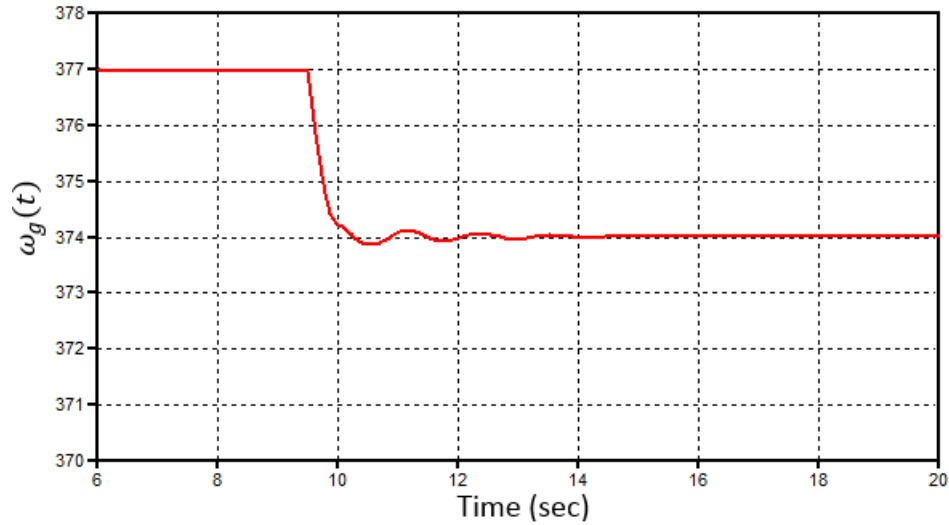


Figure 6.8: Grid frequency decrease

A. Response to Grid Frequency Change

As shown in Fig 6.8, the angular frequency of the grid system is decreased from 1 pu to 0.992 pu (i.e. actual value of 374 *rad/sec*) by rapidly increasing the total load demand as shown in the Figure 6.9 (The simulation was run for 20 sec). The primary objective for this set-up is to show how the active power is distributed from the storage element during events that causes the grid frequency to change. A very large change was used for illustration.

As the grid frequency decreases from the initial steady-state, the frequency droop (K_w) of the APC described in Figure 6.4 and Figure 6.5 starts responding to correct the grid frequency by increasing the output active power of VSG. This is achieved by increasing the P^{r*} . The "speed control" of the VSG responds to a frequency decrease in the system by extracting energy from the effective rotating mass to follow any change in the frequency. This contributes to the control of the frequency by increasing the output power, which causes the frequency to settle to a new, but lower operating point.

As shown in Figure 6.9, from $t = 0 - 10$ sec, the inverter power set point (P_{load}) is

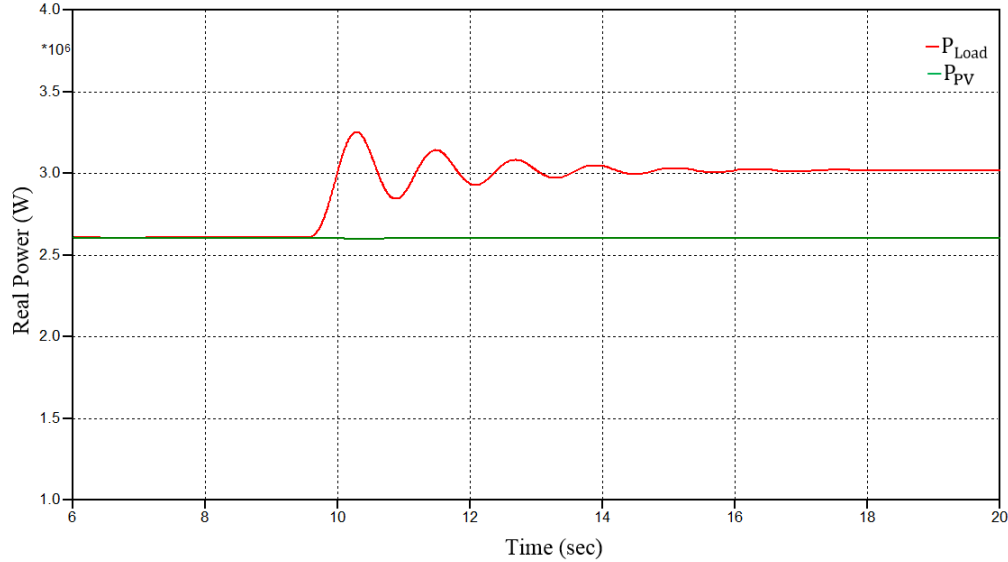


Figure 6.9: VSG active power response

equal to the PV output without any contribution from the battery storage. However, at $t = 10$ sec the grid frequency declines due to an increase in the load. Consequently, the Virtual synchronous generator controller will operate causing the battery to discharge at 600 kW to meet the load increment from the droop controller as shown in Figure 6.10. The amount of active power shared by the battery storage is determined by the constants (K_w) of the power controllers.

B. Response to Change in Voltage at the Point of Interconnect

In this case, there is a large sudden increase in the reactive power required by one of the loads in the grid which causes the voltage at the Point of Interconnect to depress.

This is quite similar to the starting of large induction motor, a situation in which the rotor field needs large reactive power to start up. At time $t = 9.5$ sec, the Point of Interconnection voltage drops as the load reactive power increased as show in Figure 6.11.

The reactive power control of the virtual synchronous generator will respond by increasing its reactive power generation to regulate voltage at the Point of Inter-

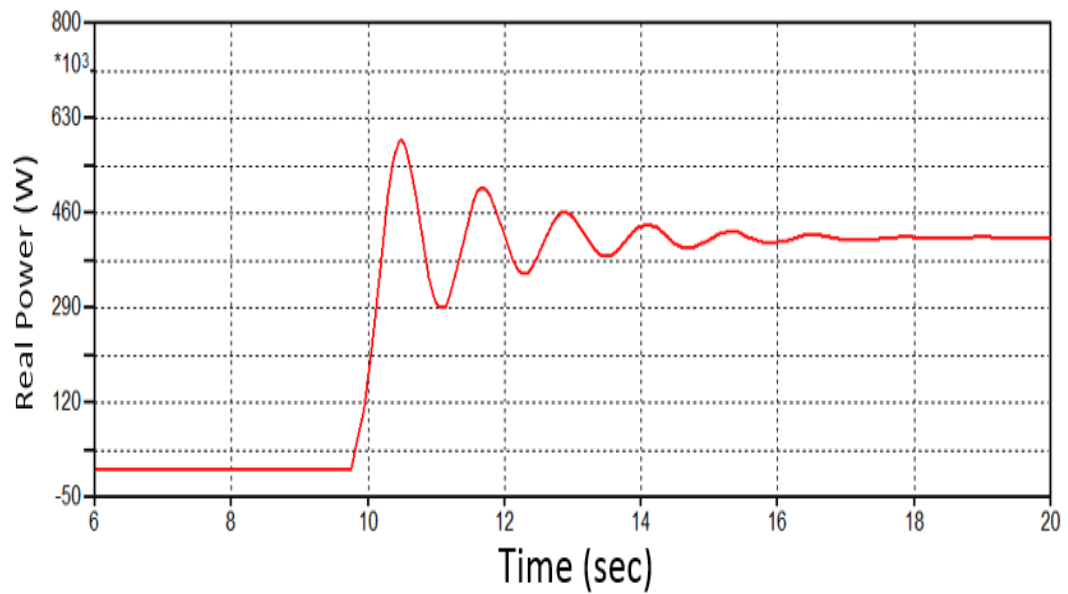


Figure 6.10: Response of the battery power to grid frequency change

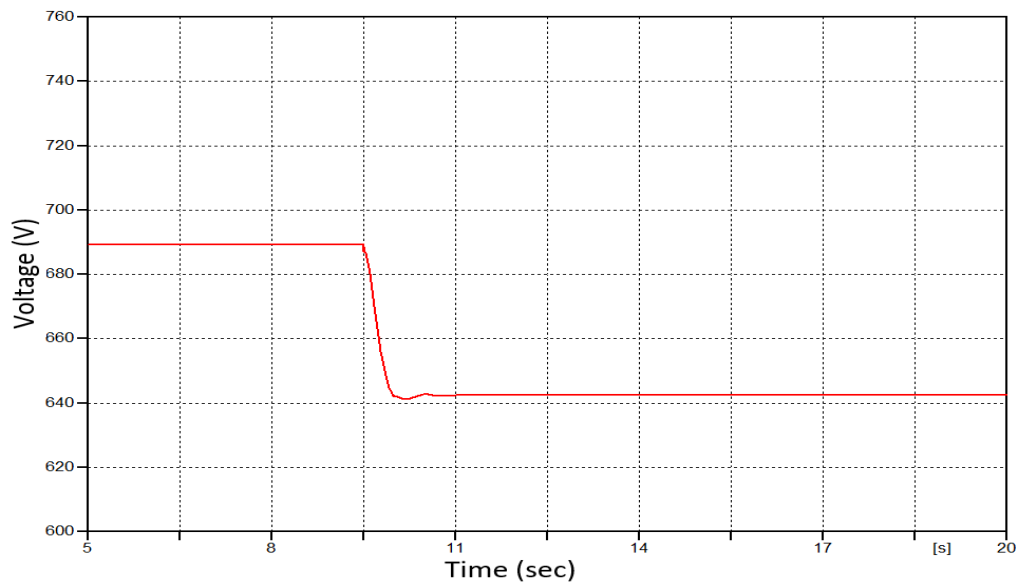


Figure 6.11: Dynamic Response of Load Voltage Amplitude

connection as shown in Figure 6.12. Hence, the VSG is able to contribute to the voltage control and local voltage stability of the grid. Without the implementation of the ac voltage regulation in the virtual synchronous generator, the voltage depression would continue until the grid becomes unstable which could eventually lead to system collapse.

C. Impact of Different Virtual Inertia Constants on Response

In this last case, the impact of different values of the virtual inertia time constant T_a of virtual synchronous generator is examined. The system experiences a grid frequency change similar to that observed in Figure 6.8. The VSG has been simulated at two values, for the inertia time constant, $T_a = 5$ sec and $T_a = 20$ sec. The system response under these two inertia time constants was compared as shown in Figure 6.13.

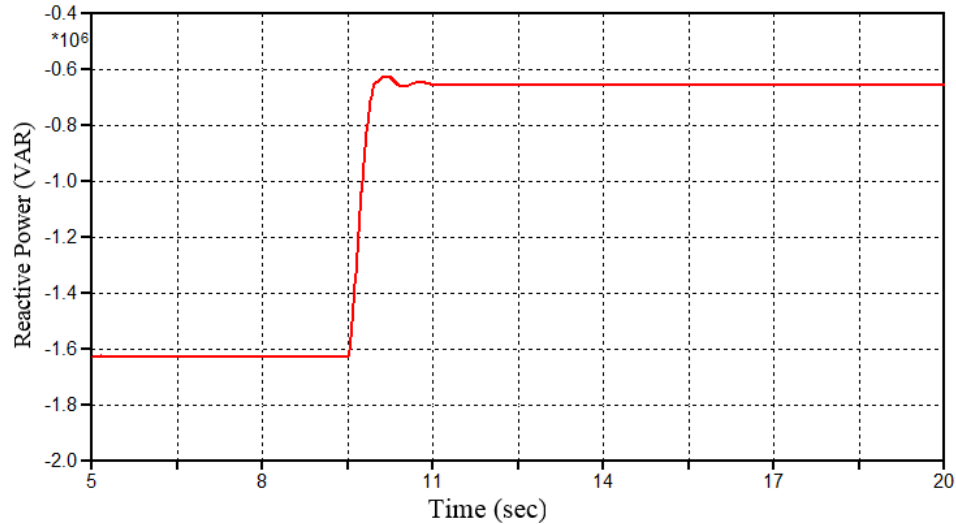


Figure 6.12: VSG Reactive Power Response

In this case, at time $t = 9.5$ sec the frequency decreases from the initial steady-state value. The BESS mitigates the frequency change by discharging, supplying power to the grid. As shown in Figure 6.13 the angular speed of VSG at a large inertia of $T_a = 20$ sec takes a longer time to settle to steady-state as compared with the lower inertia $T_a = 5$ sec. At a lower inertia time constant, the initial variation in speed is much more pronounced, although it reaches the new steady state faster than the larger inertia time constant ($T_a = 20$ sec).

Figure 6.14 illustrates that the change in power output in response to the decrease in the grid frequency for the two different time constants. Prior to time $t = 9.5$ sec,

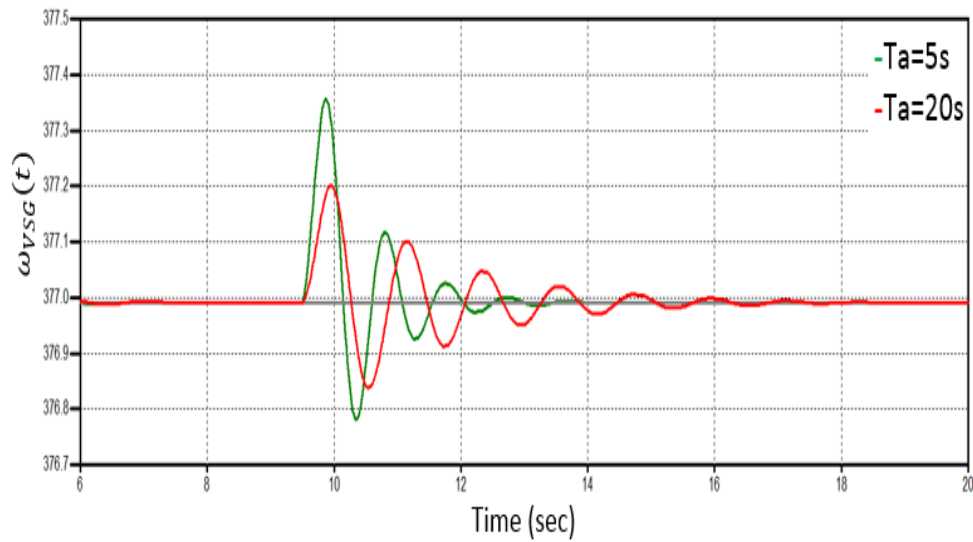


Figure 6.13: VSG angular speed variations with $T_a = 5$ sec and 20 sec

the PV generation is equal to the inverter output (ignoring the losses), hence the battery power is zero, i.e. there is no power contribution from the battery. However, as soon as the grid speed drops at time $t = 9.5$ sec, there is an increase in the power supplied by the inverter due to VSG controller.

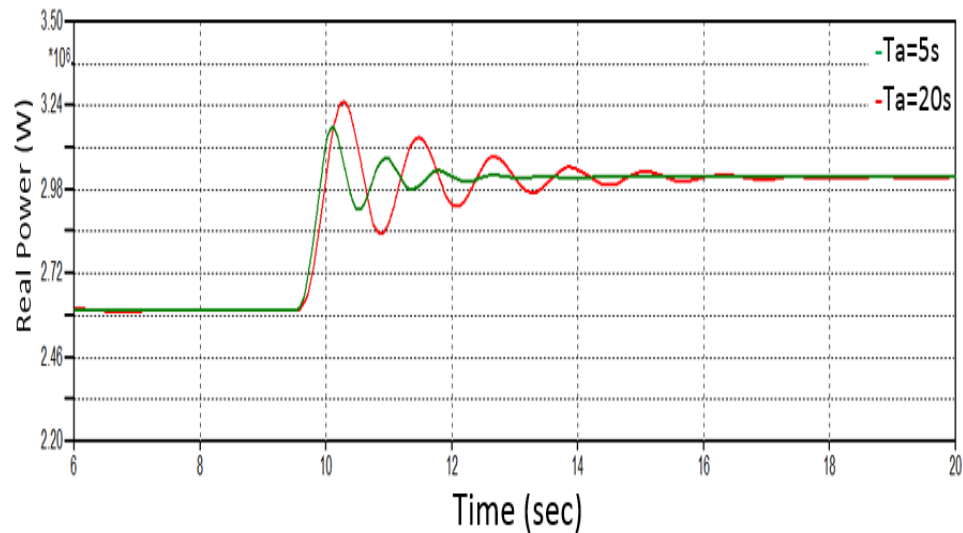


Figure 6.14: VSG Active Power Response

The comparison of the battery response for the two different virtual inertia time constants (i.e. $T_a = 5$ sec and $T_a = 20$ sec) is shown in Figure 6.15. The higher

inertia time constant requires more immediate power output from the battery (i.e. 600kW), while the lower inertia time constant however requires less initial battery power (i.e. 505kW) and a slower ramping of the battery power output. Therefore, it can be concluded that the change in time constant impacts both the peak VSG power needed and the rate of change the battery sees. This is one of the key trade offs for different time constants from battery point of view.

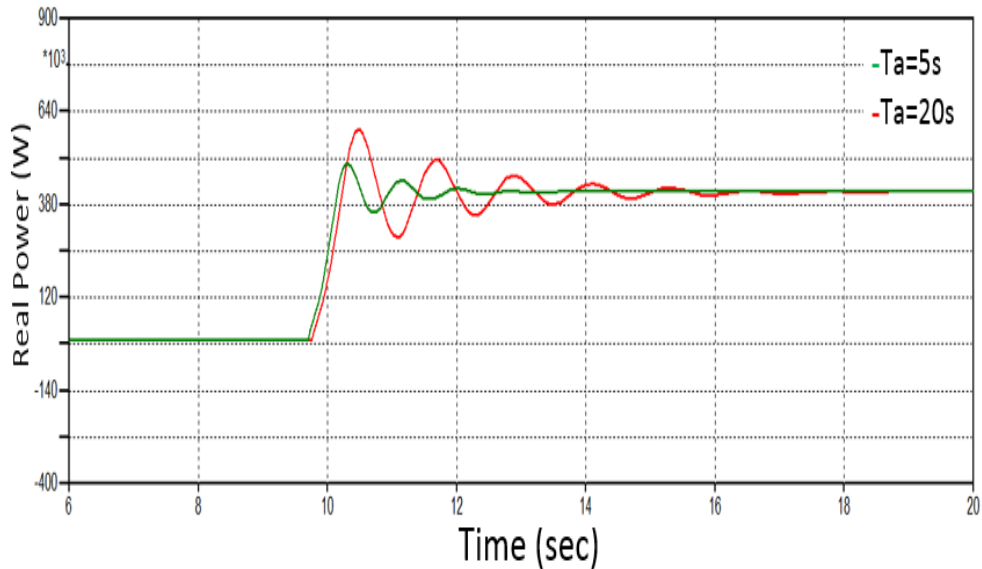


Figure 6.15: Battery Real Power Response

6.1.4 Summary and Conclusion

Coordinated additional control is an important feature to implement a combined battery energy storage system and PV installation to enhance the PV integration to support frequency. In addition, when there are variations in the grid frequency, the combined PV and battery helps to regulate the frequency similar to that of a synchronous generator's inertia behavior using a VSG emulation in the inverter controls. In this paper, the virtual synchronous generator was designed and then demonstrated.

6.2 Evaluation of Virtual Synchronous Generator Compared to Synchronous Generator (paper 2)

6.2.1 Introduction

As distributed generation (DGs) using renewable energy sources (RES) continues to increasingly penetrate the power system, more attention is being paid to the control of the power electronic converters used to integrate the DG to the power grid. These power electronic converters aid the control of the power contribution of renewable energy sources to the traditional power grid [57]. Compared to a conventional power plant which is dominated by synchronous generators, the distributed generation units have little or no rotor kinetic energy, and do not contribute any damping effect to the power system. The overall system inertia of a high penetration DG integrated power grid is drastically reduced. When the net rotational inertia in the power system is low, the frequency dynamics are faster and it becomes challenging to control the frequency for stable operation of the power system. Furthermore, due to typical control algorithms that optimize real power output, power-electronic coupled generation, such as photovoltaics, are limited in their ability to supply reactive power to stabilize power system voltage [72] and [74].

One possible solution that has been proposed and implemented to improve the dynamic response of such grid is the provision of adding inertia, albeit virtually [72]. Virtual inertia can be established in DG by incorporating energy storage, with appropriate control mechanisms for the converter. The behavior of a conventional synchronous generator can be emulated by controlling the output of the converter appropriately. In this idea, the DG can be controlled by the converter to exhibit responses similar to that of a real synchronous machine when there are changes in the operating conditions or when disturbances occur in the power grid. This concept

is referred to as a virtual synchronous generator (VSG). The major objective of the VSG is to mimic the dynamic properties and response of an actual SG for the power electronics based distributed generator units, to inherit the stability enhancement features of a SG. It does not only mimic the SG's steady state behavior, but also its transient characteristics by the application of the swing equation in the controls to enhance the inertia. Therefore, this design is implemented to operate just like the synchronous generator, providing inertia and damping properties by controlling the amplitude, frequency and phase angle of the terminal voltage [39] and [74]. In a nut shell, the VSG can provide frequency droop in the grid and damping support in response to grid oscillation. The renewable energy source can then provide ancillary services to the power grid through this means [72].

The aim of this paper is to compare the dynamic behavior of a VSG implemented in power electronics coupled generation to that of an actual SG. The control for the conventional SG were used for the comparison. Instead of the traditional phase locked loop (PLL), the VSG control implemented in this paper utilizes the swing equation to synchronize with the grid, plus the built-in droop and inertia characteristics of the VSG control can provide better active power-frequency response for grid-connected converters [39] and [75]. Different operating conditions can be accommodated by adjusting the inertia constant and damping ratio of the VSG controls to damp any power system oscillation [76].

6.2.2 System Modelling for SG and VSG Comparison

The implemented models for the VSG and SG are based on the concept of dual modeling and they are represented in the same way. Both VSG and SG models are built as modules in an EMTP type environment. The key modules of the models in the SG model which are shown in Figure 6.16 include reactive power control (RPC), active power control (APC), and an exciter and automatic voltage control (AVR).

The corresponding modules in the VSG model shown in Figure 6.17 consist of PV, battery energy system, virtual impedance control, RPC and APC [22] and [46].

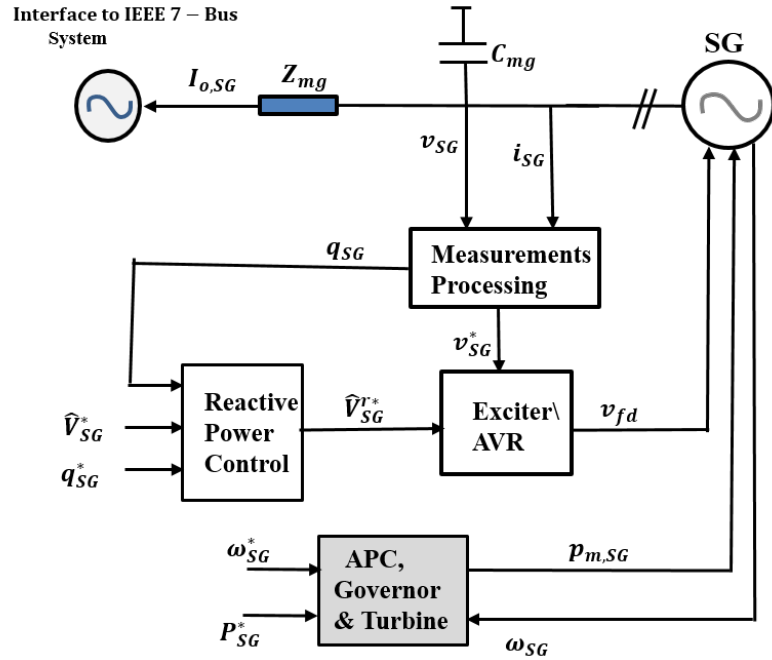


Figure 6.16: The main circuit and control block of SG

The PV and the battery storage system are connected to the dc link. More details about PV and BESS are explained in [53] and [58]. Some of the base values implemented in these models are represented by their appropriate physical units and are determined using the apparent power ratings and the rated peak phase-to-neutral voltage. Lower-case letters denote pu quantities whereas physical values are denoted by uppercase letters [39] and [77].

The active power control implemented in the VSG emulates the swing equation and governor of a SG to maintain frequency stability. While the reactive power control provides the reference ac voltage amplitude for the voltage sourced converter (VSC) to adjust the reactive power and the voltage magnitude at the point of interconnect. These two controllers determine the phase and amplitude of the VSG's voltage reference [77]. The response characteristic of the SG is implemented in the VSG using the swing equation to control the VSC to allow the converter to provide

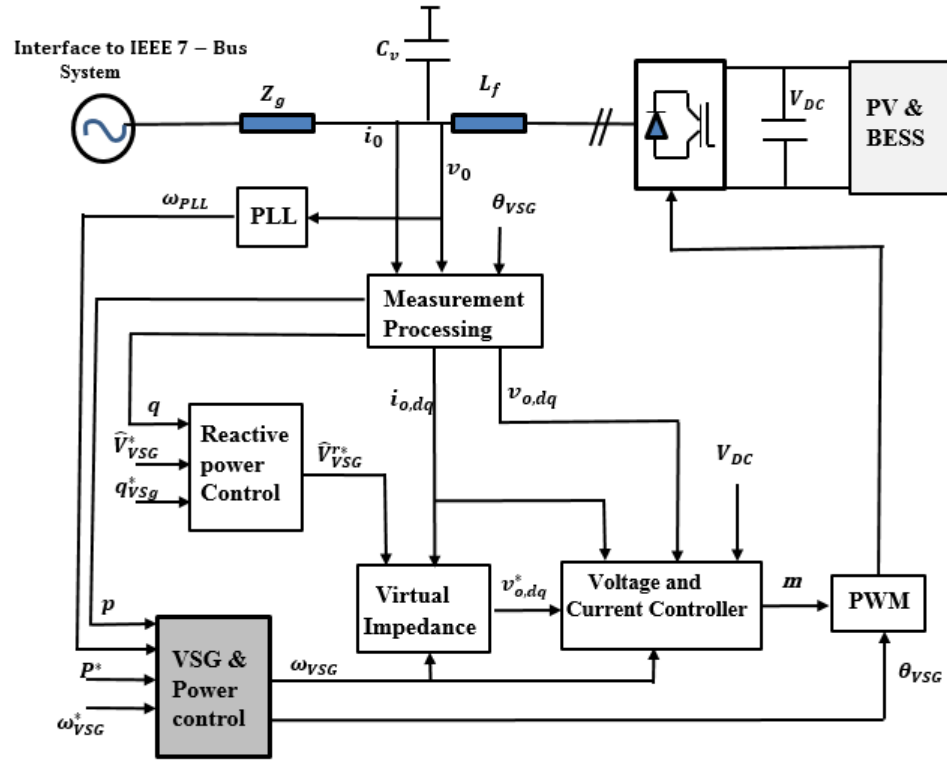


Figure 6.17: The main circuit and control block of VSG

emulated inertia. In the SG and VSG implementation, modeling and control system is applied in a rotating reference frame [22]. Transformations from the stationary reference frame to the rotating reference frame uses the amplitude-invariant Park's transformation, in which the quadrature q -axis leads the d -axis by 90° .

6.2.2.1 Virtual Synchronous Generator Equivalent Circuit to Emulate a Conventional SG

As earlier discussed, the VSG is designed to replicate the behavior and response of a SG to changes in the power system operating conditions. In this section, we will consider the VSG equivalent circuit to emulate a conventional SG and briefly discuss the modeling and operation of the control circuits of the Reactive Power Control and Active Power Control. Detailed description of the virtual impedance which mimics the stator windings is described in [78] and [79].

6.2.2.2 Reactive Power Control (RPC)

The implementation of RPC control in the VSG is very similar to the AVR model used in the SG model. In the VSG model, the output amplitude ac voltage reference, \hat{V}_{VSG}^{r*} , as shown in the block diagram in the Figure 6.18a is used as input of virtual impedance. This voltage reference output is obtained from equation (6.5) [46]:

$$\hat{V}_{VSG}^{r*} = \hat{V}_{VSG}^* + k_{q,VSG}(Q_{VSG}^* - Q_{VSG}) \quad (6.5)$$

Where \hat{V}_{VSG}^* is the voltage amplitude reference; q_{VSG}^* is the external reactive power reference; K_q is the droop constant gain of VSG reactive power; q_{VSG} is the measured reactive power output.

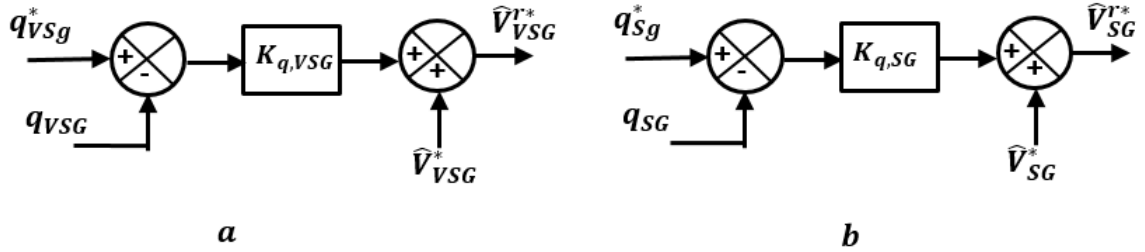


Figure 6.18: Reactive Power Control Loop (a) VSG (b) SG

Figure 6.18b illustrates the reactive power control implementation in the SG model which is quite similar to the RPC implemented for the VSG model. The output voltage amplitude \hat{V}_{SG}^* is used as the reference input voltage to the exciter. This can be mathematically represented as shown in equation (6.6) [22] and [77].

$$\hat{V}_{SG}^{r*} = \hat{V}_{SG}^* + k_{q,SG}(Q_{SG}^* - Q_{SG}) \quad (6.6)$$

Where:

\hat{V}_{SG}^* is the voltage amplitude reference.

q_{SG}^* is the external reference of reactive power.

$K_{q,SG}$ is the droop constant gain of VSG reactive power.

q_{SG} is the reactive power output measured.

6.2.2.3 Active Power Control (APC)

The active power control models of both SG and VSG are somewhat similar in the sense that they both use droop control. The APC of the VSG as shown in Figure 6.19 includes a droop control term that represents the equivalent frequency speed governor steady-state droop characteristic, to the control of the VSG power response to frequency deviations [39] and [78]. The reference power to the VSG, $P_{m,VSG}^*$,

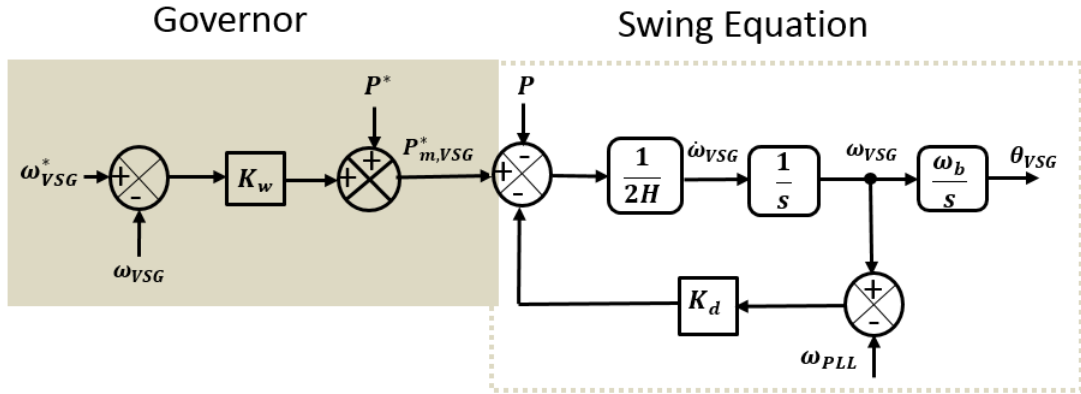


Figure 6.19: Active Power Control loop of VSG

mimics mechanical power of the synchronous generator in the external loop and is used as the reference input for the VSG. Thus, the APC is obtained by multiplying the droop constant gain, K_w , with the difference between reference speed ω_{VSG}^* and actual speed, ω_{VSG} , and finally by adding an external active power reference P^* as shown in equation (6.7) [76] and [79].

$$\frac{d\delta\omega_{VSG}}{dt} = \frac{(P^{r*} - P - K_d(\omega_{VSG} - \omega_{PLL}) + K_W(\omega_{VSG}^* - \omega_{VSG}))}{T_a} \quad (6.7)$$

The block diagram in Figure 6.20 illustrates the active power control, governor and turbine model implemented for the SG in this study. The active power of the

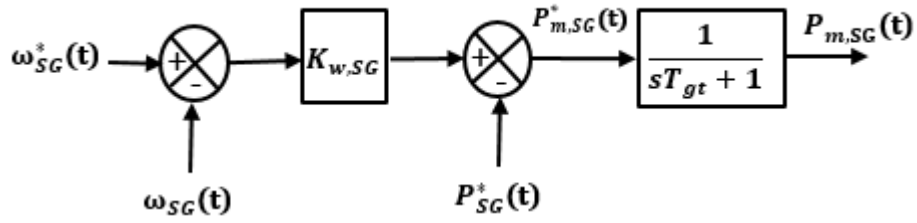


Figure 6.20: Active Power Control, turbine and governor

frequency droop in the APC is determined from equation (6.8) [73], [76] and [80].

$$P_{m,SG}^* = P_{SG}^* - k_{\omega,SG}(\omega_{SG} - \omega_{SG}^*) \quad (6.8)$$

The control of the frequency droop is defined by the frequency droop constant gain, $k_{\omega,SG}$. This droop constant acts on the difference between the reference angular speed ω_{SG}^* and the actual measured SG speed ω_{SG} ; P_{SG}^* is mechanical power; P_{SG}^* is power reference in pu. The response delay of the governor's mechanical system is a first order lag unit with a time-constant, T_{gt} .

6.2.3 Simulation Results

Simulations were carried out on the implemented VSG and SG models in order to compare their dynamic response under different operating conditions. The parameters of both SG and VSG used in this model have the same values. For the base model, the rated power is 2.75 MVA, while a rated voltage of 690 V (V_{LL-RMS}). The same parameters implemented for both VSG and SG to aid the appropriate dynamic response comparison in table A.4 and table A.1 respectively.

To demonstrate the similarity of the VSG and SG dynamic behavior, a number of cases were implemented and tested in this section.

The response of the VSG and SG were studied under varying operating conditions which include variations in the grid frequency, reactive power demand and inertia time constant. Results obtained from the simulation of these cases are presented and discussed below.

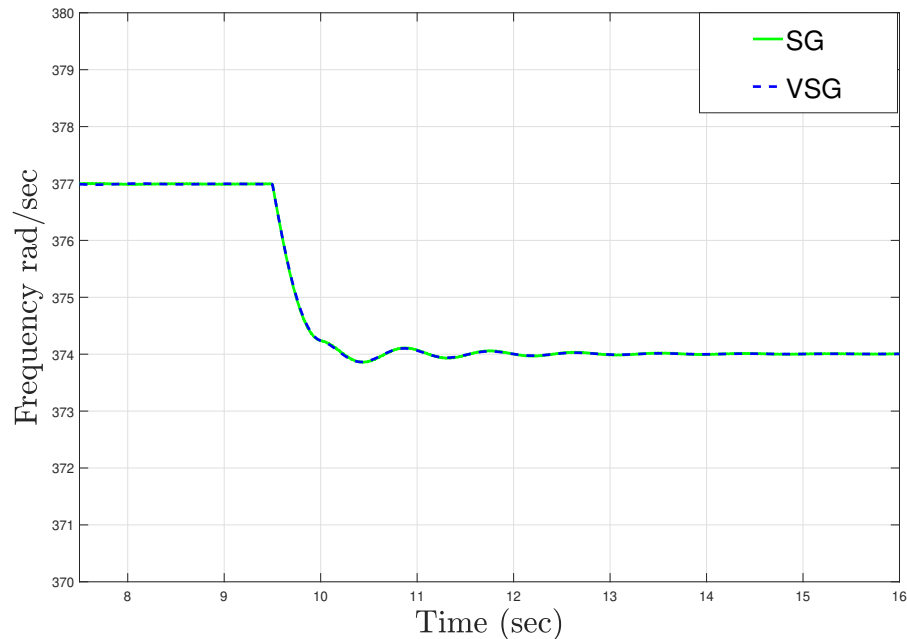


Figure 6.21: Comparison between SG and VSG response to an increase in real power load on the grid with change in frequency

A. Response to Grid Frequency Change

As shown in Figure 6.21, an increase in the load without an increase in the generation causes the angular frequency of the system to decrease. The main objective of this case is to compare the dynamic response of the synchronous generator and virtual synchronous generator to events that cause the grid frequency to change. From time $t = 0$ to 9.5 second, the mechanical power is equal to the electrical power as illustrated in Figure 6.22. However, at time $t = 9.5$ second, there is a change in the system operating condition due to increase load demand at the PCC. This causes a change in both ω_{VSG} and ω_{SG} as they decrease from the reference speed.

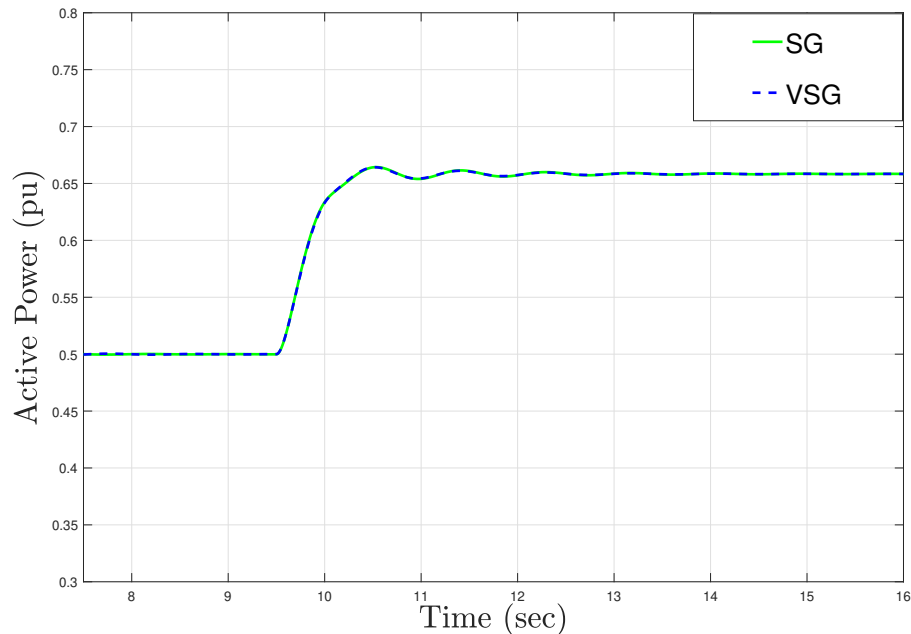


Figure 6.22: Comparison between SG and VSG response to an increase in real power load on the grid with change in per unit power set point

The new steady-state value of the synchronous speed for the VSG and SG can be obtained mathematically using equation 6.9.

$$\omega_{Syn} = \frac{P^* - P_{load} + K_W(\omega^*)}{K_W} \quad (6.9)$$

In this case ω^* is 1 per unit, $P^* = 0.5$ per unit, K_W is 20 pu, which can be used to calculate the new ω_{Syn} . It is observed that the calculated value of 0.992 per unit (i.e. actual value of 374 rad/sec) matches the value for the generator shown in Figure 6.21.

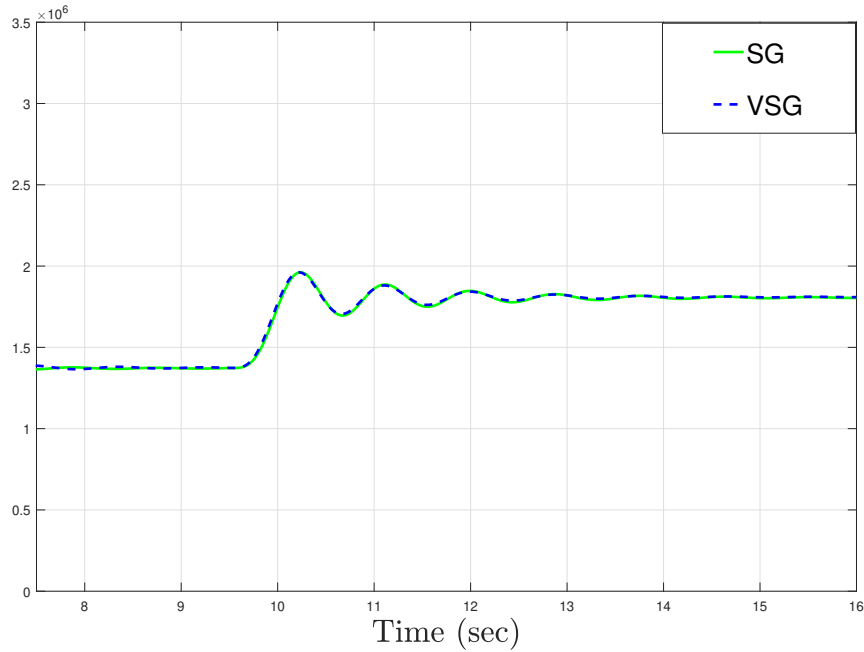


Figure 6.23: Comparison between SG and VSG response to an increase in real power load on the grid with change in output power (W)

As explained in Section 6.2.2, the frequency droop gain constant Kw in the APC of the VSG has the same value as that implemented in the SG. When the grid angular speed decreases from the set point, the APC controls for both SG and VSG respond to adjust the grid speed by increasing the mechanical power as shown in figure 6.22.

The shaft power of the SG is adjusted by the governor in response to the frequency decline in the power grid. In the case of the VSG, the APC increases the power supplied to the grid by pulling energy from the battery to try to restore frequency.

It is important to note that severe oscillations affect the performance of the virtual synchronous generator as converter controls will act to limit the current within the inverter or battery limits, imposing more severe limits than would be the case with

a SG. A higher damping factor can be employed in the VSG to reduce these severe oscillations. On the other hand, intense oscillation is a common phenomenon in the SG and it is unaffected by this issue because it has higher overcurrent capacity than the VSG but the resulting thermal overloading could decrease the time to the next rewind. As shown in Figures 6.21, 6.22 and 6.23 the dynamic control response of the implemented VSG models frequency deviation behavior are very similar to the synchronous generator response. Figure 6.23 shows the matching increase in the output active power for both the VSG and SG in response to the frequency change.

B. Response to Change in the Reactive Power Demand

This scenario examines and compares the dynamic response of the VSG and SG to an increase in the reactive power demand due to sudden load change, which results into voltage depression at the PCC. Equations (6.5) and (6.6) show that a reactive power mismatch causes a change in the excitation reference. As expected, this event causes

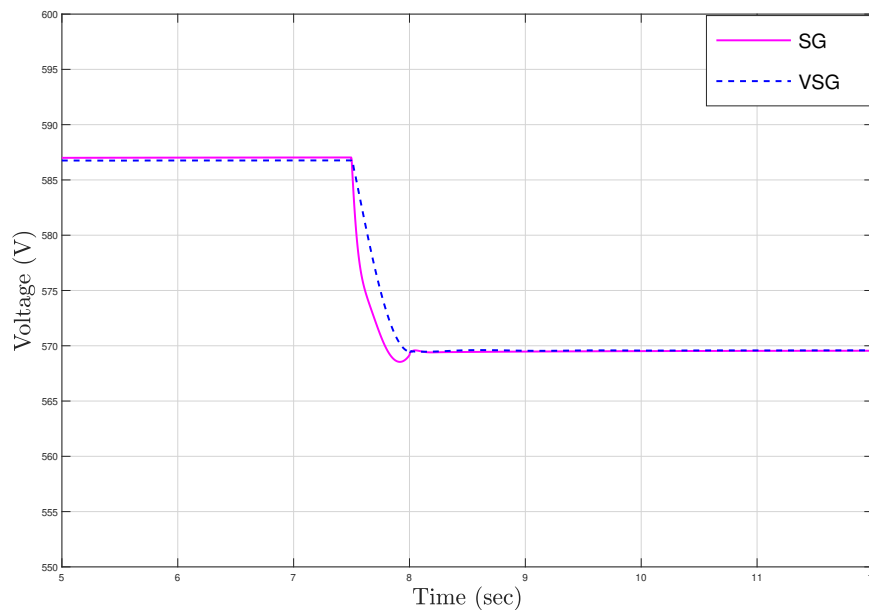


Figure 6.24: Comparison between SG and VSG response to an increase in reactive power load on the grid with change in voltage at point of interconnect

the voltage droop-based reactive power control of the VSG to respond by increasing its reactive power production in order to accommodate the increased demand at the PCC.

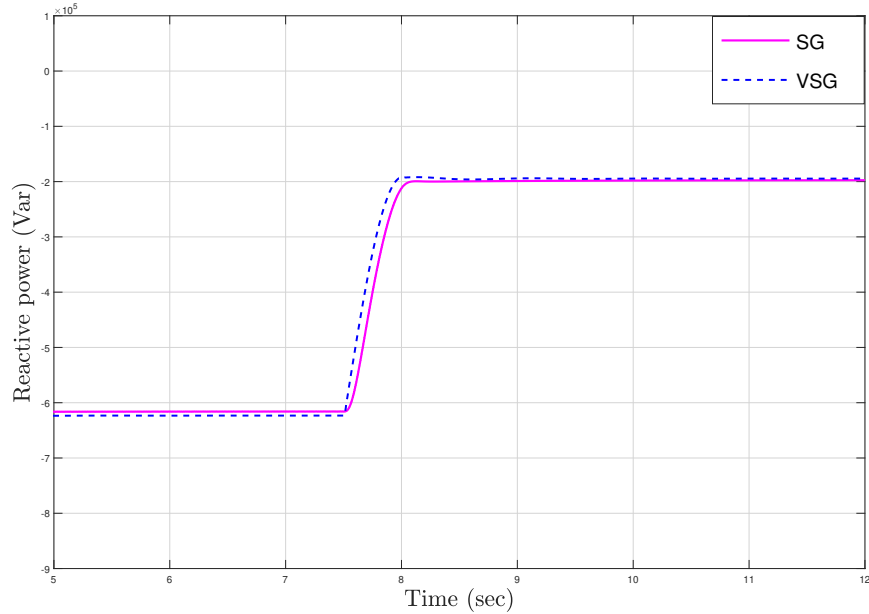


Figure 6.25: Comparison between SG and VSG response to an increase in reactive power load on the grid with change in delivered reactive power

Similarly, the RPC of the SG would operate to mitigate this voltage sag by adjusting the voltage amplitude reference, which prompts the AVR to change the exciter voltage, as shown in the block diagram in Figures 6.18(a) and 6.18(b). In this case the SG does not have the reactive capacity to bring the terminal voltage back to the set point and enters a voltage droop response.

For the time period $t = 0 - 9.5$ sec, the reactive power supply is equal to the reactive power demand. However, at time $t = 9.5$ sec there is a sudden increase in the reactive power demand on the system, with the deficit causing voltage depression at the PCC as shown in Figure 6.24. In response to this event, the RPC of both the VSG and SG increase their respective reactive power setpoints to mitigate the PCC voltage sag. As shown in Figure 6.25, the dynamic responses of both the VSG and SG

to this disturbance are similar with minor discrepancies in their response.

C- Changes in SG and VSG Response with Different Inertia Time Constants

The main objective of this scenario is to observe the inertia response of both the VSG and SG to frequency change under different inertia time constants T_a . As discussed earlier in equation 6.7, kinetic energy is released or absorbed in the SG to damp frequency oscillation due to changes in the power system operating condition. This behavior is emulated in the VSG through the integration of energy storage to provide emulated inertia in the grid. The inertia response versus time for both the virtual synchronous generator and synchronous generator models depend on the value of the inertia time constant. In order to investigate and compare the dynamic performance of both VSG and SG, different inertia time constant were set in the simulation and the angular speed response of the VSG and conventional generator were plotted.

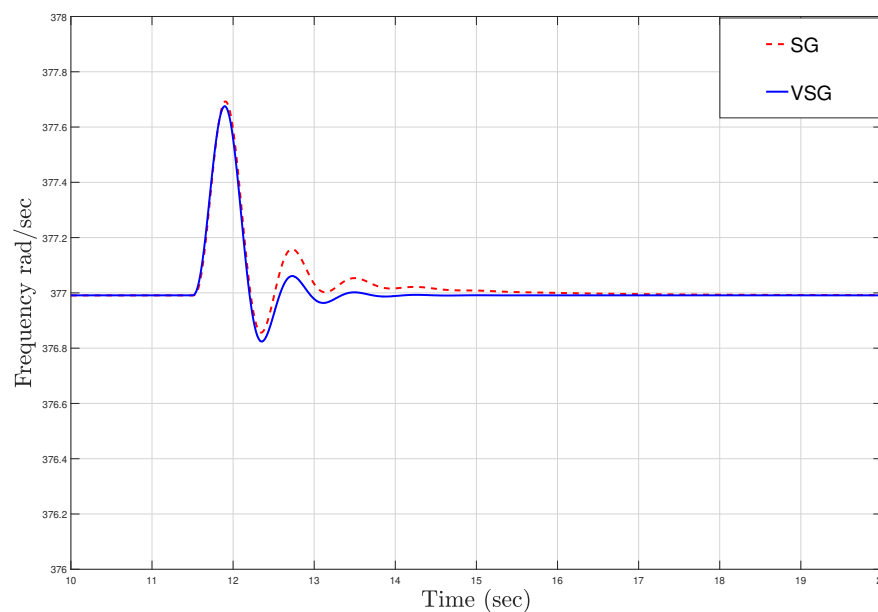


Figure 6.26: Comparison between SG and VSG response to disturbances to different inertia time constants with frequency responses with $T_a=6$ sec

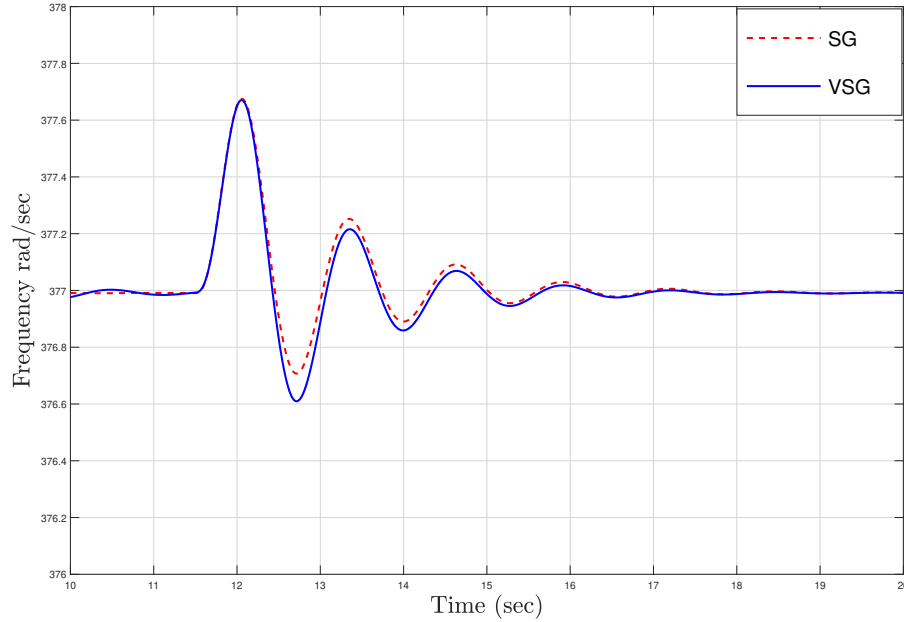


Figure 6.27: Comparison between SG and VSG response to disturbances at different inertia time constants with frequency responses at $T_a = 20$ sec

The VSG and SG models were simulated at two inertia time constants, $T_a = 6$ sec and with $T_a = 20$ sec. In this case, at time $t = 9.5$ sec, the grid frequency decreases due to a sudden increase in the load power demand. As shown in Figures 6.26 and 6.27, the VSG and SG angular speed of the implemented models at large inertia $T_a = 20$ sec takes longer time to reach steady-state as compared to the lower inertia $T_a = 6$ sec. Also, it is observed in the figure that the initial drop in speed in the virtual synchronous generator is a bit more than that of the synchronous generator, although they reach steady-state at the same time so their response characteristics don't match as well. At a lower inertia time constant of $T_a = 6$ sec, both models reach the new steady-state faster than the larger inertia time constant.

6.2.4 Conclusion

In this paper, a VSG was modeled to mimic both the steady-state and the transient characteristics of a SG. The dynamic response of the VSG to a transient disturbance

in the power grid was compared to the response of the SG under similar operating conditions. It is clear from the results that the VSG can be deployed in place of synchronous generator because of the similar dynamic behaviour of both models to varying operating conditions. However, the VSG needs sufficient voltage and current ratings for the VSC, and enough energy storage (energy and power ratings). This study confirms that virtual synchronous generator can indeed be controlled to exhibit similar dynamic response as that of the conventional synchronous generator.

Chapter 7: Results and Discussion

This chapter will present the results of the ATP simulations. The simulated events will try to replicate transient events that impact the structure and operation of the system described in Chapter 6. The goal is to determine the capacity of the battery needed to support the system inertia under largest credible contingency (worst event where a response is desired). The power system must be able to withstand contingencies such as the loss of a major component. It will be helpful to study and test the system's performance during those contingencies.

In the model as shown in the Figure 6.1, the PV system is connected to a small power grid through a step-up transformer. The total load connected to the system is approximately 16 MW. The PV supplies a steady-state output active power of 2.749 MW. The remaining power is supplied by the grid source. The system initially operates in steady-state. To evaluate the ability of the combined PV and energy storage system on the system response disturbances were created applying three phase faults to some critical transmission lines in the grid with the fault cleared after 200 msec. These events will disconnect some loads from the power grid momentarily. For the period of time under consideration, the PV is generating more power than required, hence resulting into generation-load imbalance in the power system. As shown in the Figure 6.1, the battery energy storage system is combined to the grid-tied inverter to enhance the frequency control and power stability of the PV/BESS system. All the parameters of this model are listed in Table A.1.

7.1 Test Scenarios

To validate the model, two scenarios were simulated and studied with the results presented in this section. The inertia constant, damping coefficient and frequency droop settings were varied in order to empirically find a preferred battery size to ensure PV adequate power system stability. Two inertia time constants were considered for both

scenarios. In addition, two different cases were considered for each test scenario. For each case, two values of droop gain (K_ω) were considered, keeping damping factor (K_d) constant.

In both tests, the irradiation of the PV is assumed to be constant providing 2.749 MW. These scenarios tests are done for sizing the battery real power and energy ratings in order to meet desired frequency deviation metrics.

7.1.1 TEST SCENARIO 1

In this test scenario, the inertia time constant is kept constant at four seconds. The cases considered under this scenario is described in the following cases.

Case 1

First, the effect of virtual synchronous generator control parameters on the damping coefficient and frequency droop characteristic, is examined and tested. This test was conducted with the damping coefficient K_d set to 400 and $K_\omega=20$ pu and then equal to 40 pu. Their impact in terms of inertia response was studied in response to a system disturbance. An instantaneous loss of power and a change in frequency dynamics occur when if a generator is dropped. Since both of these characteristics are time varying, the worst-case is considered for analysis. Theoretically, use of the frequency deviation in the swing equation response to a system disturbance can be used to estimate for required stored energy. The proposed method is computationally simple and provides a rapid estimate of the frequency response, and later, ESS sizing. Since the contingency size depends upon the system settings, the event chosen in this work is the loss of 2.749 MW for 0.2 sec, where the ESS provides upwards frequency support in the case of generator outage and downwards support in the case of load outage.

The active power response at point of interconnect is shown in Figure 7.1. After

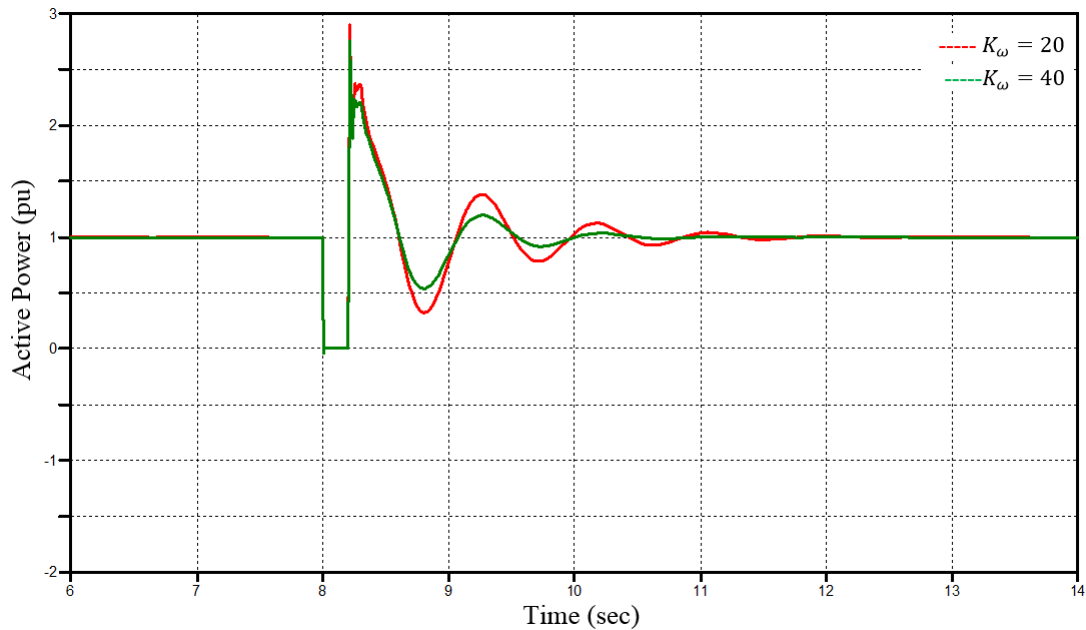


Figure 7.1: Comparing power response at PCC with $T_a = 4$ sec and $K_d=400$ following a loss of generation

the event, the energy storage system capacity and control settings are proposed to improve the frequency response of the grid.

Figure 7.2 shows the frequency deviation at point of interconnect with an energy storage system controlled for two values of inertia time constants. The resulting frequency deviation is ≤ 0.5 Hz for $P_{PV}=2.749$ MW at an inertia time constant $T_a=4$ s. The rate of change of frequency at the PCC connection is important to prevent misoperation of distance protection relays and must not be higher than 0.5 Hz/sec [54]. The verification of the right side and left side of the swing equation is described in Figure 7.3. This figure illustrates the response of the implemented swing equation which represents the relative motion between the synchronously rotating stator field axis with respect to time and the rotor axis. The swing equation as shown in 7.1 is used to study the dynamic response of the machines. The inertial response of the exchange of the power between the electrical grid and the emulated mechanical rotor due to the deceleration or acceleration of the rotor (rotor swing) was described in Chapter 6.

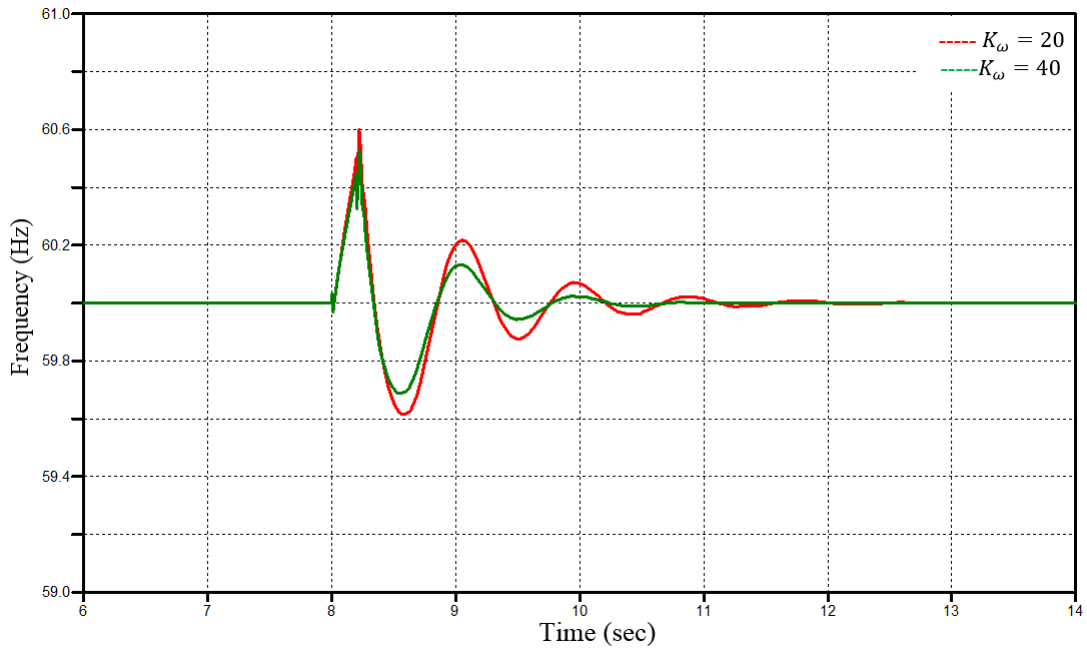


Figure 7.2: Comparison of the system frequency response to disturbances with $T_a = 4$ sec and $k_d = 400$ at different droop gains

$$\frac{2H}{w_s} \cdot \frac{d\omega}{dt} = P_m - P_e \pm P_{ESS} \quad (7.1)$$

The virtual synchronous generator converts the delivered power from the PV generation combined with the energy from the battery to control the power that will be supplied to the loads through the power network while emulating the behavior of a synchronous generator. In Figure 7.3, from the time $t = [0 - 8]$ sec, the accelerating power (mechanical power - electric power) is zero, since there is no disturbance during this time. However, at time $t = 8$ sec, an event was introduced into the power system by the disconnection and reconnection of the VSG to the grid at PCC. The decelerating power due to the loss of generation caused the grid frequency to change and the BESS mitigates the frequency change by varying its output in an oscillatory fashion, damping the disturbance. After time 8.2 sec the system recovers to a steady state.

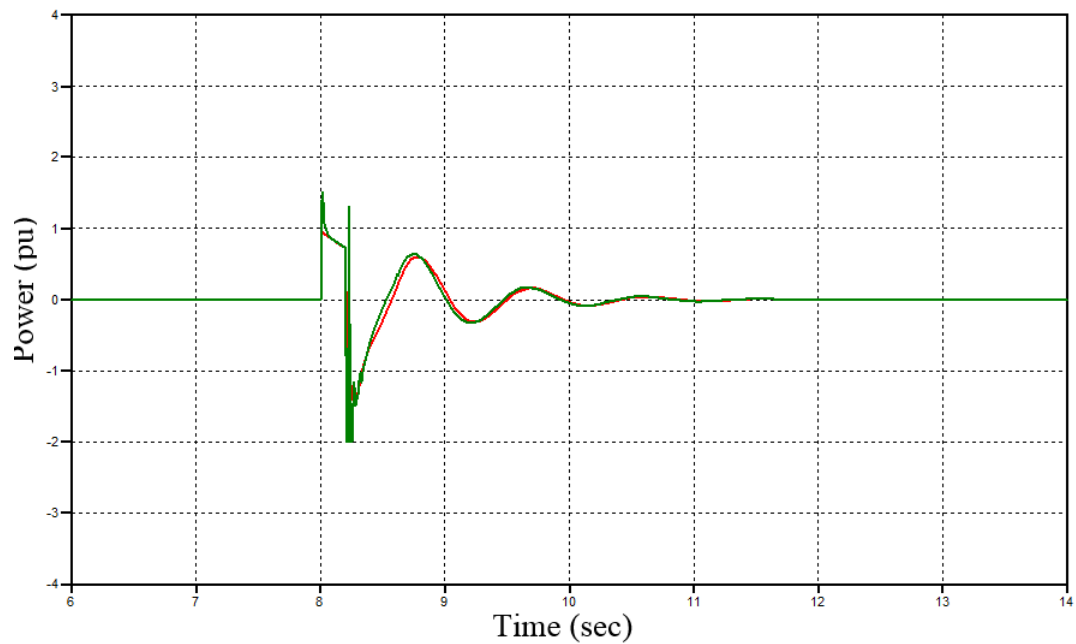


Figure 7.3: The represent of equation governing the rotor motion of the VSG

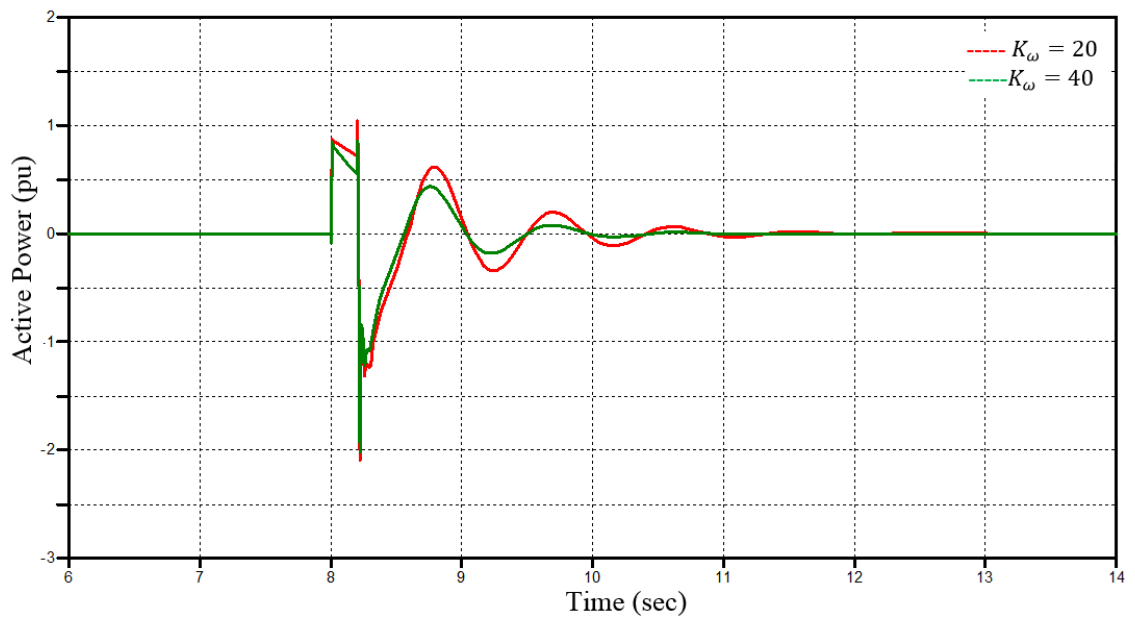
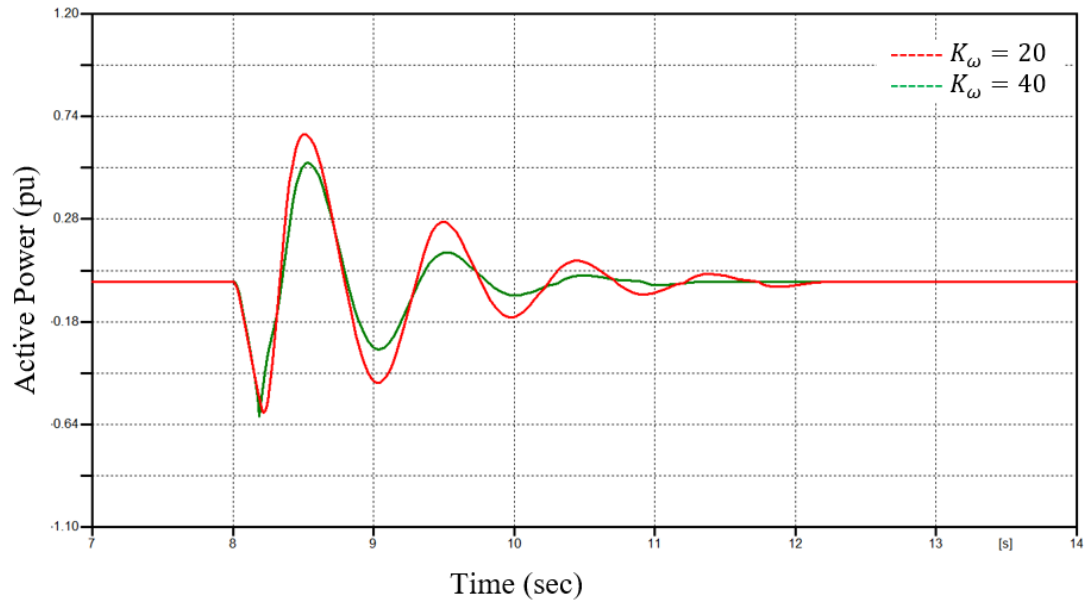


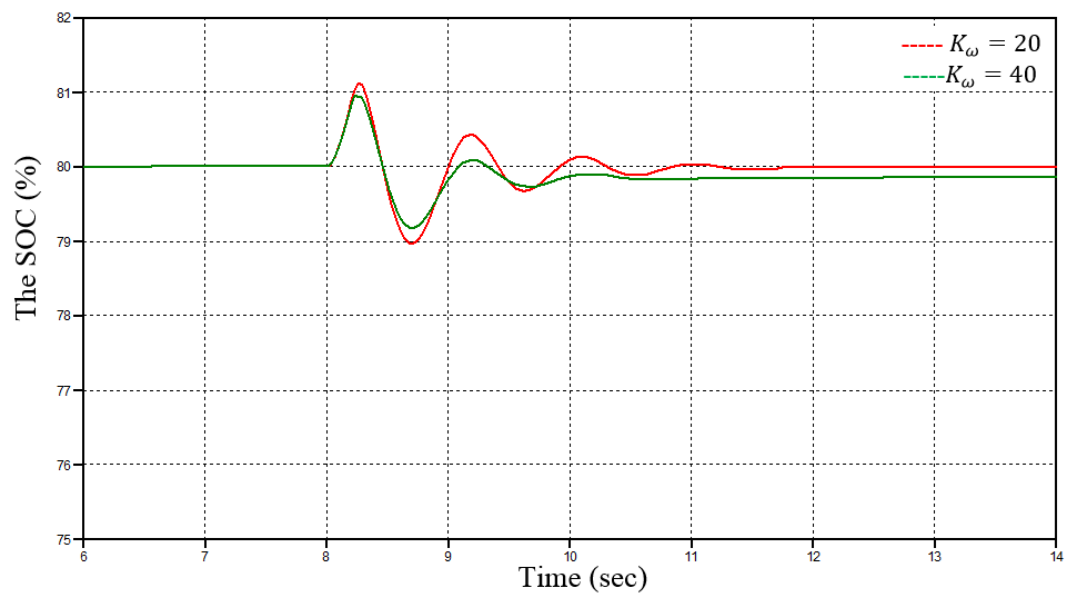
Figure 7.4: Total power from droop term and damping term in response to disturbance with $T_a = 4$ sec and $k_d = 400$

The impact of the droop term P_d (droop) and damping term P_ω which is equal to $K_\omega(\omega_{VSG} - \omega_{VSG}^*)$ are described in equation (4.47). The battery energy storage system must be able to contribute to the inertia of the power grid system until the

frequency reaches the steady-state value by adjusting the damping term as shown in Figure 7.4.



(a)



(b)

Figure 7.5: Comparison of (a) Battery output power under different droop gains and $T_a = 4$ sec (b) variation of the SOC of the battery when K_ω is varied

From the block diagram of the active power control explained in chapter 5, the droop constant gain value acts on the difference between the grid angular speed ω_{VSG}

and reference angular speed ω_{VSG}^* as illustrated in equation (7.2).

$$P_{m,VSG} = P_{m,VSG}^* - K_w(\omega_{VSG} - \omega_{VSG}^*) \quad (7.2)$$

The energy storage system must contain stored energy ESS_s in order to be able to discharge and provide energy to the system when $\omega_{VSG} < \omega_{VSG}^*$ during the disturbance. However it should be able to absorb energy ESS_d from the grid and charge when the $\omega_{VSG} > \omega_{VSG}^*$. The nominal energy is given by equation (7.3) [54].

$$E_{batt} = ESS_s + ESS_d = \int_a^b P_{batt}(t)dt + \int_b^e P_{batt}(t)dt \quad (7.3)$$

Where the start time of providing inertia response is b and the end time of the inertia response as obtained from the first zero-crossing of battery power output. The maximum power capacity required for the battery energy system as calculated by the characteristic of the system inertia is 0.6 pu as shown in Figure 7.5(a). The initial level of SOC is set as 80% based on [53]. During a contingency the SOC's variation depends on the status of the battery (i.e. charging or discharging) as shown in the figure 7.5(b).

Figures 7.6(a) and 7.6(b) illustrate how the voltage phase angle at the filter capacitor varies with respect to the power flow of the grid. However, the virtual inductance of the VSG causes its phase angle to be different when compared to the phase angle of the PLL. Hence, the phase angle of the VSG is equivalent to the conventional SG internal voltage phase angle. On the other hand, the PLL tracks the VSG's terminal voltage phase angle.

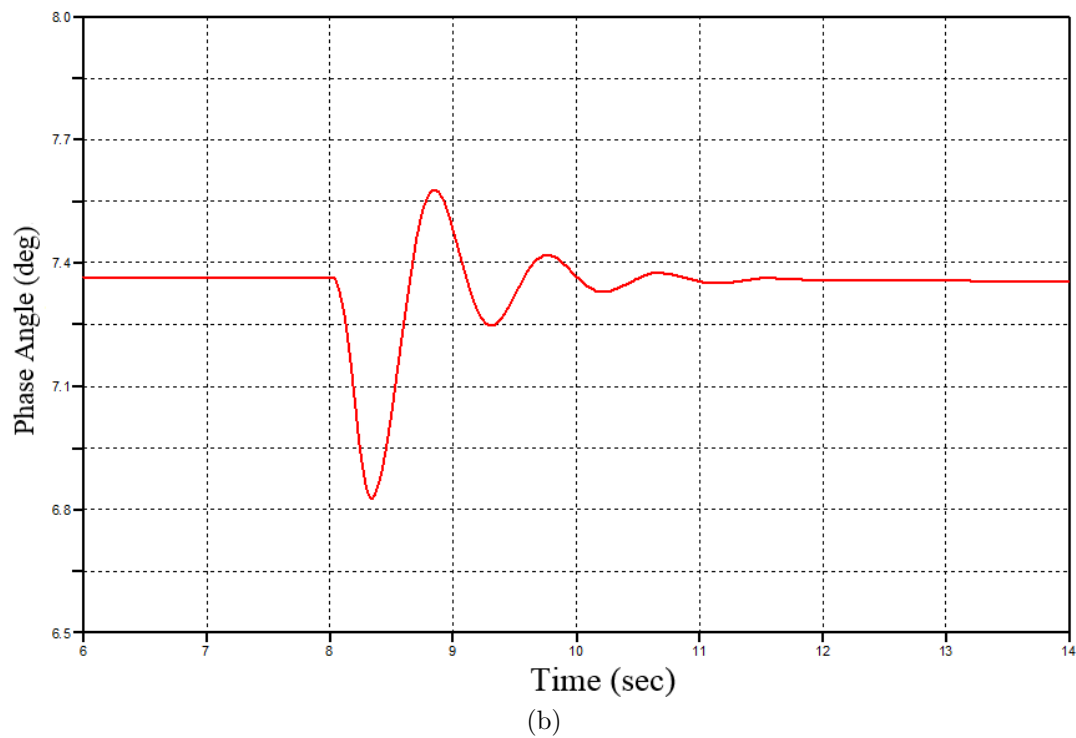
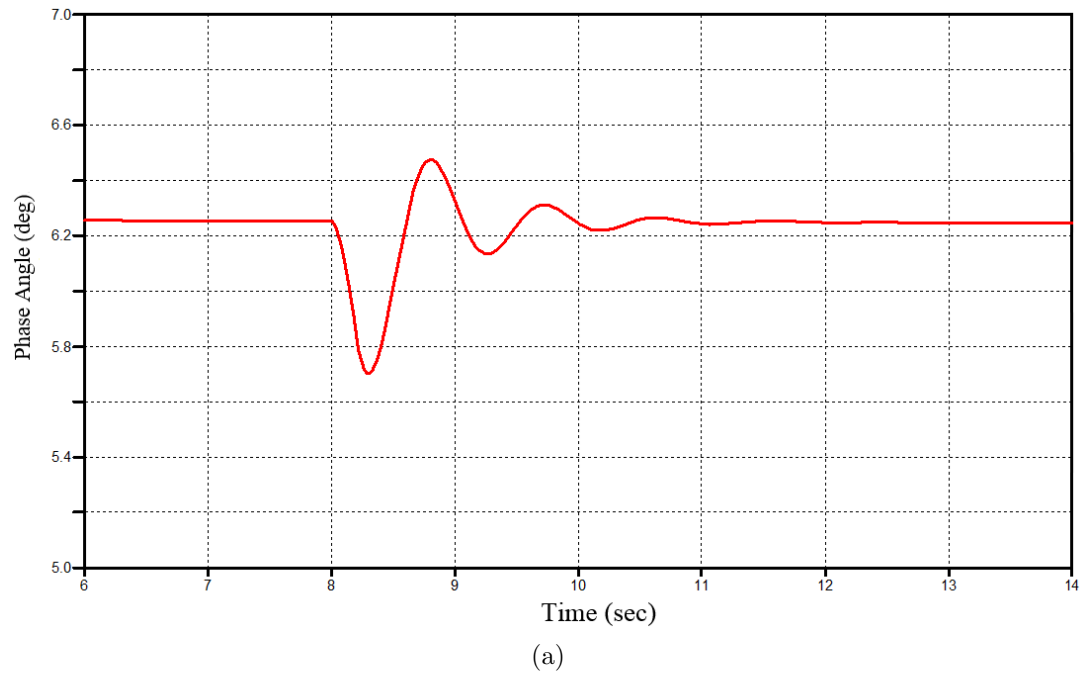


Figure 7.6: Phase angle displacement of (a) VSG reference frame, (b) PLL reference frame

Case 2

Based on the control system theory the damping coefficient is an important parameter for system stability. Similar concept is used for the virtual synchronous generator to

create damping effect for the system stability [60]. To verify the damping effect in the model, K_d was decreased to observe the system response. In this case, the equation of motion of the rotor was applied without including damping. The contingency created for case 1 is repeated in this case 2 with the damping gain K_d set to zero, and $K_\omega=20$ pu and 40 pu. As a result, the frequency swing is very high at point of interconnect due to the absence of the damping component as shown in Figure 7.7. This demonstrates that the damping component is required to damp the oscillation.

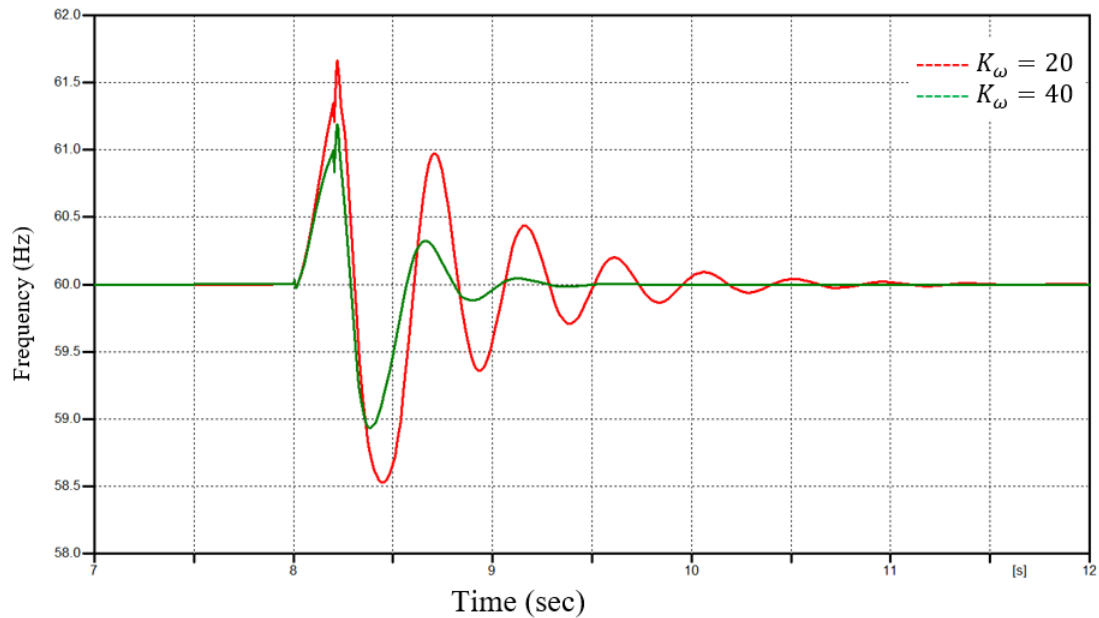


Figure 7.7: Comparison of the system frequency response to disturbances with $T_a=4$ sec and $k_d=0$ when K_ω is varied

In this case, the high gain of K_ω lead to less deviations of the frequency and a lower rate of change of frequency and battery discharging.

The swing equation is used to calculate the power delivered by energy storage system by integrating the area under the power curve between the start of the event and the first zero-crossing. The output power from the battery for the two values of the droop gain due to the generator contingency are shown in Figure 7.8. The battery output changes due to the disturbance event that caused frequency deviation in the power system. By comparing the applied droop gain $K_\omega=20$ and $K_\omega=40$,

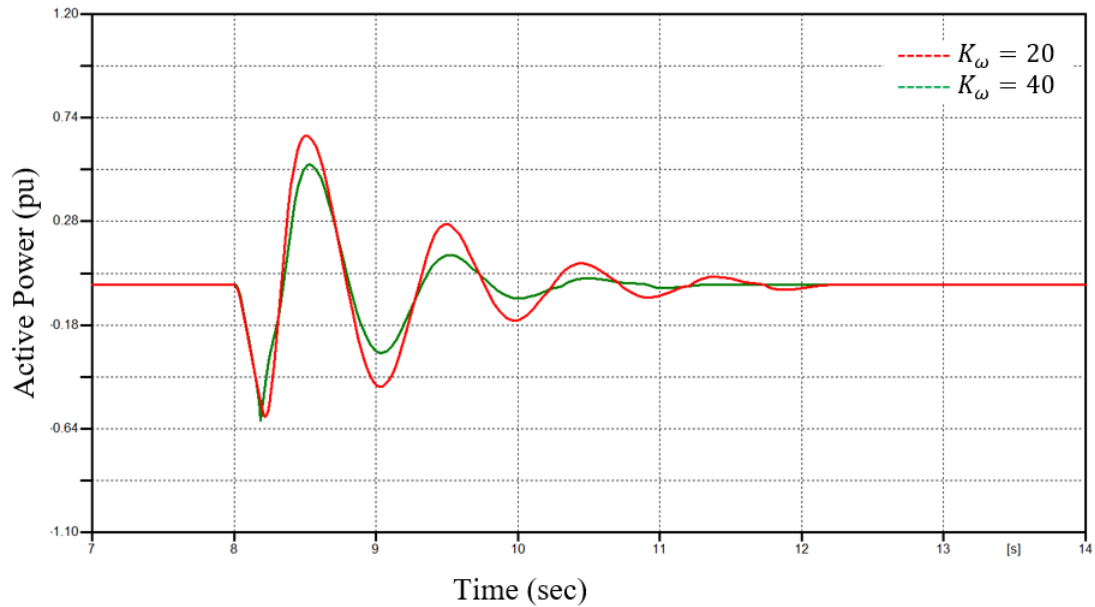


Figure 7.8: Comparing power response at PCC with $T_a = 4$ sec and $K_d = 0$ following a loss of generation

it can be concluded that the higher gain results in more damping of the system frequency. However, due to ROCOF limitation, excessive high gain will cause the dynamic response to deteriorate and cause the control system to be unstable.

The comparison of the response obtained evaluating the VSG response due to the event the quantity of energy required for each case is described in Table 7.1. The ROCOF, df/dt , F_{max} and F_{min} are presented in this table. After performing all tests, in order to provide the inertia response in term of ROCOF as in test 1, it was found that the most severe contingency occurs when K_d is zero and the K_ω is 20 pu and requiring the largest peak power rating for the battery. Moreover, with the removal of the damping K_d , the system frequency and ROCOF increases considerably. The increase of the frequency response can cause the system to be unstable. The ROCOF values and frequency deviation at the PCC increases when the $K_d = 0$ for $K_\omega = 20$ and decrease a little bit when K_ω is increased to 40 pu. However, when implemented with K_d in the system, the ROCOF with $K_\omega = 20$ pu decreases and increases with $K_\omega = 40$ pu. With small inertia $T_a = 4$ sec, the ROCOF and frequency deviation is

still at higher value. The battery power required in test scenario 1 is (0.57 pu) during charging and (0.63 pu) during discharge.

In order to decrease the frequency deviations and rate of change of frequency with the limit values which is less than 0.5 Hz/sec , we have to increase the T_a to limit the ROCOF value from exceeding $\geq 0.5 \text{ Hz/sec}$ and try to find the battery size to provide sufficient system inertia.

Table 7.1: The results for Test 1

(The battery pu values are based on the inverter power rating)

Case		F_{min}	F_{max}	df/dt	Battery Power	
					Charge	Discharge
Case1	$K_\omega=20$	59.65	60.5	0.26	0.57 pu	0.63 pu
	$k_d=400$	$K_\omega=40$	59.7	60.4	0.25	0.5 pu
Case 2	$K_\omega=20$	58.5	61.5	0.57	0.51 pu	0.74 pu
	$k_d=0$	$K_\omega=40$	59	60.8	0.4	0.47 pu

7.2 TEST SCENARIO 2

In this test scenario, the inertia time constant is increased compared to Test 1 and kept constant at 10 seconds. All other parameters and conditions such as solar irradiation or temperature remain unchanged. Two cases are considered in this scenario.

Case 1

The event from Test 1 was repeated with all subcases using the higher inertia value to observe the system response and determine battery size. This test was conducted to assess the impact of increasing the virtual inertia time constant of VSG.

The system experiences a grid frequency change similar to that observed in case 1 under the first test scenario. The parameters of K_d and K_ω implemented in this case are similar to that considered in the test scenario 1. The damping coefficient K_d in this case is set to 400, while $K_\omega=20$ pu and 40 pu. Figure 7.9 shows the response

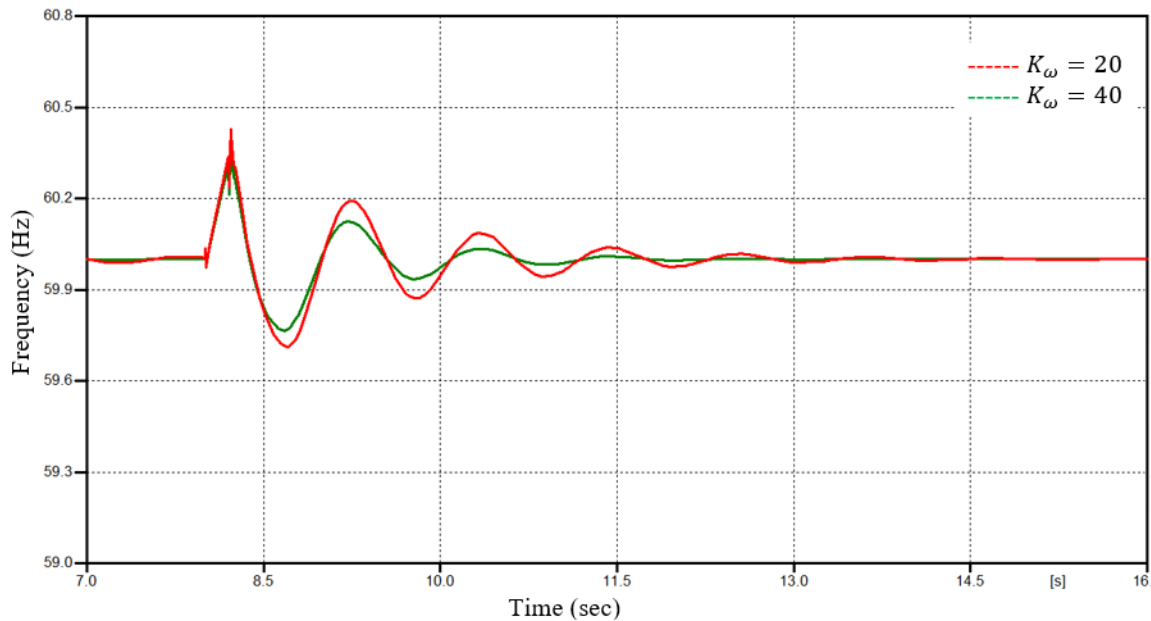


Figure 7.9: Comparison of the system frequency response to disturbances with $T_a=10$ sec and $k_d=400$ at different droop gains.

of the frequency deviation at the point of interconnect. It shows the comparison of

the system response to different droop frequency gains (i.e. $K_\omega=40$ pu and $K_\omega=20$ pu). As illustrated in the figure, the system returns to nominal frequency faster when $K_\omega=40$ pu compared to $K_\omega=20$ pu.

Figure 7.10 shows the comparison of the battery power with two different droop gains $K_\omega=20$ pu and $K_\omega=40$ pu, with the damping coefficient maintained at 400. As shown in the figure, it can be observed that when the droop gain $K_\omega=20$ pu needs a power output from the battery of 0.6 pu. However the $K_\omega=40$ pu only requires a peak battery power transfer of 0.5 pu.

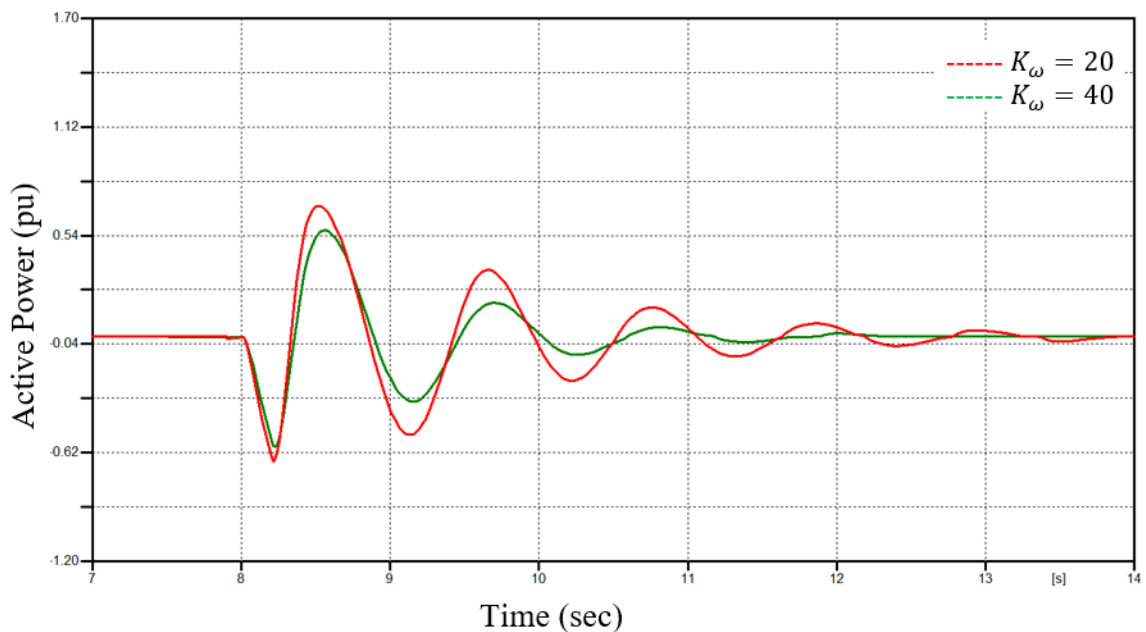


Figure 7.10: Comparison of battery output power to disturbances with $T_a=10$ sec and $k_d=400$ at different droop gains

It can be concluded from Figure 7.10 in this case that a greater maximum peak capacity is required when compared to Figure 7.5(a) in test 1. The reason being that a higher inertia time constant was implemented in test scenario 2.

Case 2

Case 1 was repeated with the damping coefficient K_d in set to 0 in this case, while the inertia time constant and the droop frequency gains are kept constant.

As it is observed in Figure 7.11, the response of the frequency at point of interconnect tends to last for longer time compared to Figure 7.9 in case 1. In addition, the figure shows that frequency at PCC experiences less oscillation when the $K_\omega = 40$ pu compared to the case with a K_ω of 20 pu.

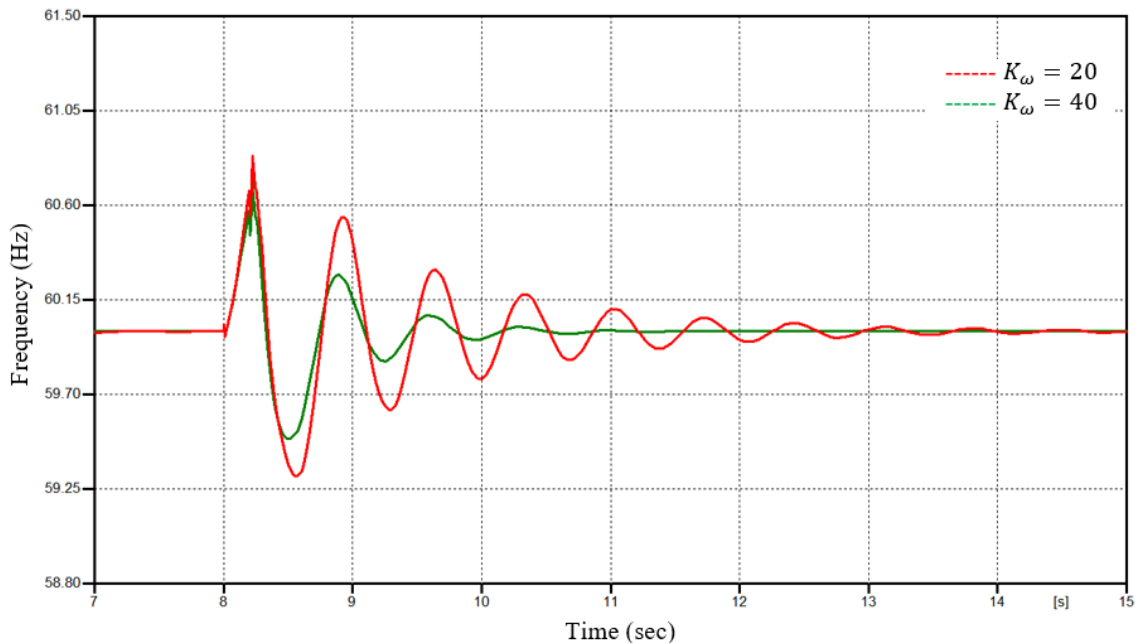


Figure 7.11: Comparison of the system frequency response to disturbances with $T_a = 10$ sec and $k_d = 0$ when K_ω is varied

Figure 7.12 shows the power delivered by the battery due to the inverter response to the frequency variations. This figure illustrates the comparison between output active powers of battery at two different frequency droop gains. It can be observed that, $K_\omega = 20$ requires higher battery sizing when compared to $K_\omega = 40$.

The simulation results from test 2 are summarized in the Table 7.2. The increase in the virtual inertia leads to reduced frequency overshoot and provides slower frequency response. As explained before, when big disturbances occur, the rotor of the

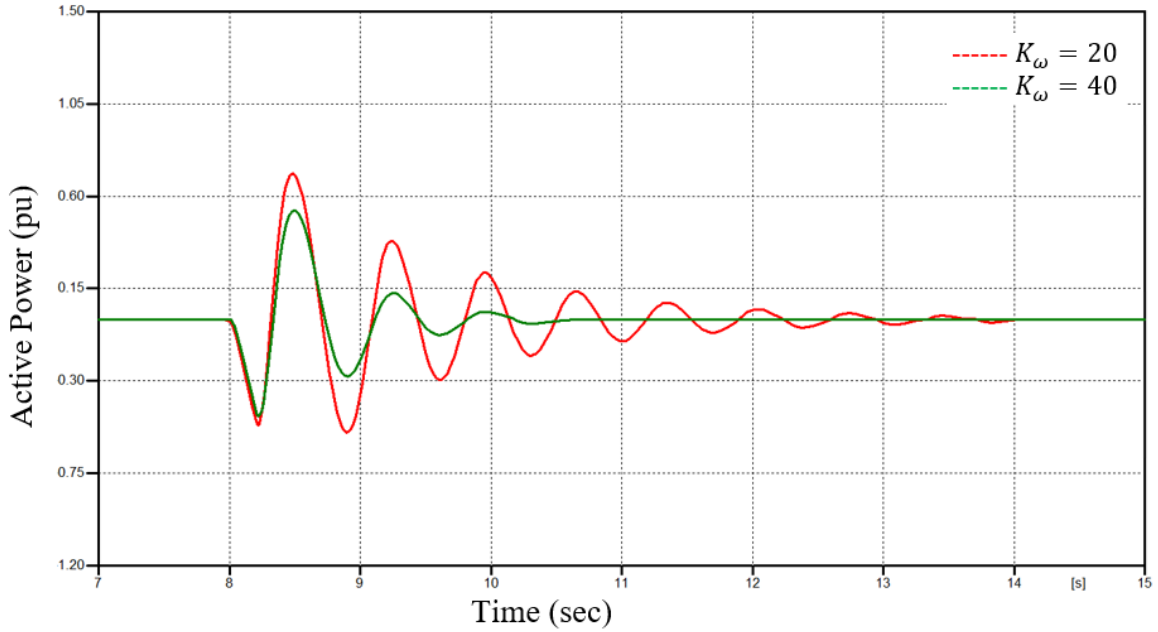


Figure 7.12: Comparison of battery output power to disturbances with $T_a = 10$ sec and $k_d = 0$ when K_ω is varied

conventional synchronous generator accelerates or decelerates to enhance stability of the system. In the virtual synchronous generator the battery energy storage system works working in a similar manner.

Table 7.2: The result for Test 2

(The battery pu values are based on the inverter power rating)

Case		F_{min}	F_{max}	df/dt	Battery power	
					Charge	Discharge
Case 1	$K_\omega=20$	59.7	60.32	0.116	0.62 pu	0.67 pu
	$K_\omega=40$	59.75	60.3	0.112	0.59 pu	0.57 pu
Case 2	$K_\omega=20$	59.3	60.8	0.37	0.57 pu	0.69 pu
	$K_\omega=40$	59.45	60.6	0.35	0.48 pu	0.53 pu

As illustrated in the Tables 7.1 and 7.2, the power system stability depends on the combined response of the components in the system. The rate of change of the power ratio to the ROCOF is directly dependent on the system inertia. A system with larger total inertia can withstand larger disturbances when compared to a system with small inertia. Furthermore, the small inertia system may see large ROCOF value for the large disturbance which may cause nuisance tripping of protective relays. The reason behind this is that large inertia system has slower ROCOF as compared to small inertia system. The virtual synchronous generator needs increased energy storage capacity in order to emulate a larger inertia.

In order to fulfill all operational requirements in these tests with high impact disturbances, it can be concluded from the results that the battery power needed in the test scenario 2 is 0.62 pu during charging and 0.69 pu during discharge. This section presents the results for the vary limited test conditions that were considered in order to find a battery peak power rated size (MW) that meet the project goal.

The objective of the this study is to investigate the change of inertia coefficient gain and frequency droop gains needed to allow a significant renewable energy source integration and determine the battery power rating.

7.3 Energy Storage Capacity Estimation

The same contingencies that were described in the earlier scenarios were also considered in this section. The main objective of this section is to calculate the energy storage capacity required to respond to these disturbances. As discussed in the construction of VSG, emulated inertia replaces kinetic energy (KE) of the rotor. KE can be expressed by equation (7.4) [8].

$$KE = \frac{1}{2} \cdot J \cdot \omega_m^2 \quad (7.4)$$

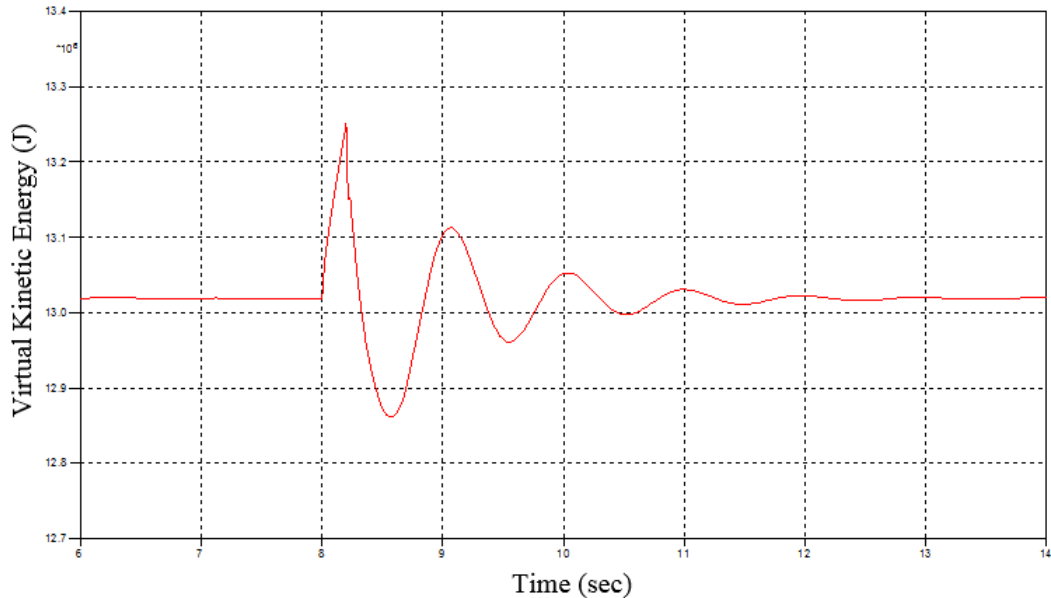


Figure 7.13: Virtual Kinetic Energy

The simulation result in Figure 7.13 shows that the steady-state kinetic energy for a synchronous machine rated at 2.75 MVA, with $H = 10$ seconds is 13.03 MJ. However, when the disturbance the KE fluctuates between 13.25 MJ and 12.87 MJ with respect to the frequency speed variations at transient state. The battery does not need to start out storing 13.03 MJ as an initial state of charge, but it needs

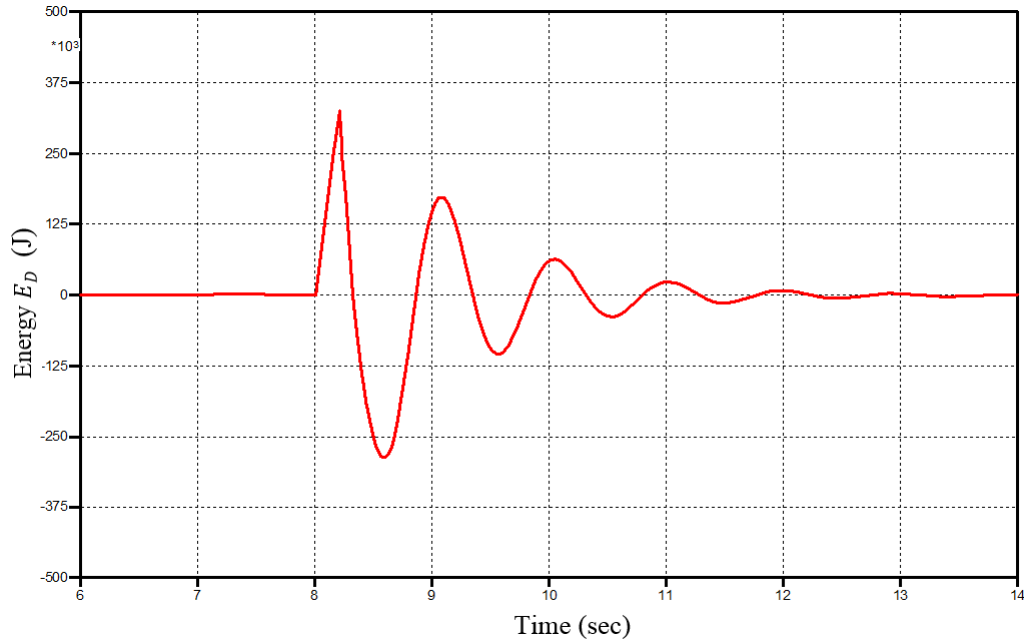


Figure 7.14: Energy required to satisfy damping term

to be able to supply or absorb energy associated with the swings for the set inertia constant.

Equation (7.5) illustrates the motion of the machine which mimics conventional generator with a damping coefficient. In order to fully emulate a synchronous generator, there is a desire to add damping term (D_s) to the virtual synchronous generator. The inverter could also implement a damping controller without the inertia emulation.

$$\frac{2H}{\omega_s} \cdot \frac{d\omega}{dt} = (P_{input} - P_{output}) - D_s \quad (7.5)$$

Figure 7.14 shows the result determining D_s from the simulation results using (7.5) and integrating the result using (7.6). This plot shows the energy required to implement a damping controller.

$$E_D = - \int D_s \cdot dt \quad (7.6)$$

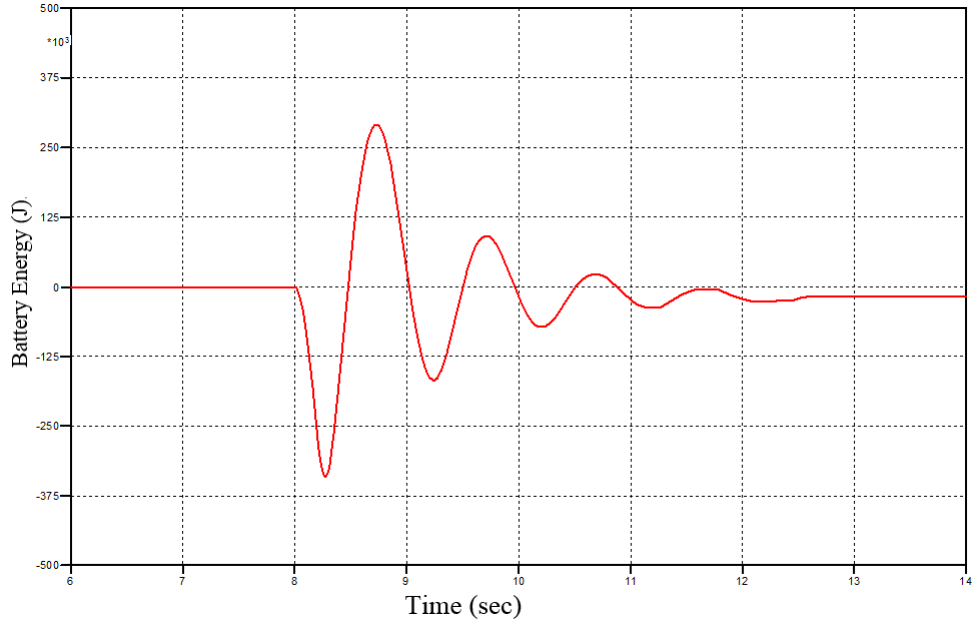


Figure 7.15: Change in energy from the battery in response to the disturbance

In the conventional generator, the resistance of the damping winding absorbs the energy consumed by the damping term. However, in the case of the virtual synchronous generator, the energy storage performs this role. Figure 7.15 shows the energy the battery needs to exchange with the grid in response to the disturbance.

The difference PV output (equivalent to mechanical power) and inverter output electrical power is supplied by the energy storage. The integral of the power difference is stored as E_{total} as illustrated in equation (7.7).

$$E_{total} = - \int (P_m - P_e).dt \quad (7.7)$$

The maximum energy storage requirement to compensate the P_e being controlled to emulate the swing equation is shown in the Figure 7.16.

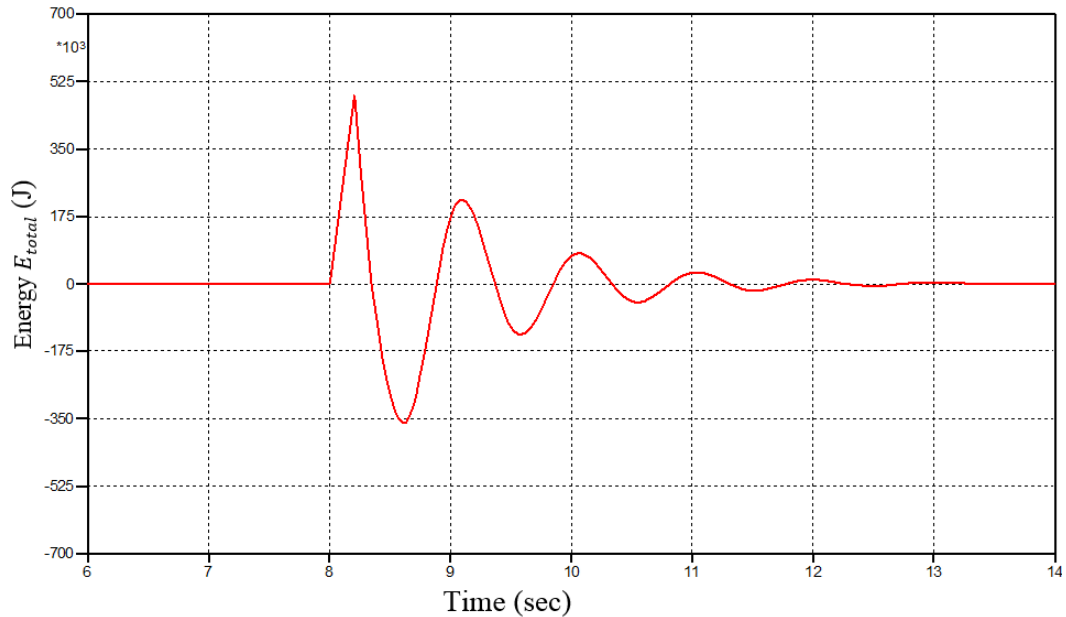


Figure 7.16: Total energy (E_{total})

7.4 Discussion

Energy storage systems need to be added to the system to replace the lost inertia when synchronous generators are replaced. The power and energy ratings of the energy storage are impacted by the inertia settings for the virtual synchronous generator.

This chapter illustrated the possible impacts of high renewable energy integration and proposed a simple technique for approximating battery sizing with respect to power and energy by providing emulation inertia in order to meet the target system, power and frequency characteristics. Three scenarios were simulated in order to determine the battery energy sizing required to support the power system inertia which prevents rate of change of frequency. Nevertheless, one major limitation of using battery energy storage system as opposed to a synchronous generator is that it is limited in terms of power rating of the inverter and of the battery as well as energy, which prevents them from providing most of the possible beneficiary impact they can have on the network. In order to achieve all operational needed in these test scenarios with major disturbances, the results in test scenario 1 show that the battery needs

to absorb a peak power of 0.57 pu and supply a peak power of 0.63 pu. The results from test scenario 2 show that the battery needs to absorb a peak power of 0.62 pu and supply a peak power of 0.69 pu.

Chapter 8: Summary, Conclusions and Future Work

8.1 Summary

Although the penetration of the distributed renewable energy source into the traditional grid has risen over the past few decades, the potential negative impact of this integration can never be overemphasized. One issue is the absence of inertia in the renewable energy sources. To mitigate this problem, this dissertation examines the integration of virtual synchronous generators (VSG) controlled based on swing equation. Through this concept, it is plausible for the renewable distributed generator to exhibit the characteristics and behavior of synchronous generators (SG) such as inertia, frequency droop functions and damping. One of the aims of this dissertation was to determine the extent to which frequency stability can be improved using a storage element in conjunction with the renewable energy source to create virtual inertia.

The models in this dissertation are implemented, designed and simulated in an electromagnetic transient program (EMTP) a PV inverter connected to a 9-bus AC system.

This dissertation illustrated the results of several scenario that include some contingency such as rapid increase in electrical load and variations in PV generation power. In this dissertation, we are trying to make the PV generation more stable and reliable by using battery energy storage system. The model depends on batteries paired with a PV inverter to store energy acquired during sunlight hours. This model consists of three types of converters a boost DC/DC converter with the PV inverter, a bidirectional DC/DC converter interfacing the battery, and the grid connected DC/AC inverter. Different simulation scenarios were tested and evaluated. The simulation model reacts correctly demonstrate how the maximum power point tracking (MPPT) control would react corresponding to the irradiation state. The response of the system with energy storage was tested by simulating cases with solar

irradiation change and ac load changes described the first half of Chapter 5 (paper1). In addition, the second paper in Chapter 5 described the impact of control setpoints for the dc/dc converter for the BESS on charge cycling. The energy management designed in the chapter was used to regulate the controller of the battery interface converter. Ramp limits are implemented to make the lifetime of the battery longer.

To ensure the positive contribution of the PV to the stability of the grid, this dissertation models the virtual synchronous generator based on the swing equation to control the power setpoint for the grid-imposed inverter based on 9-bus AC. This dissertation also examines the response of the grid under diverse varying conditions. The cases considered includes variations in the grid frequency, inertia time constant, active and reactive power. The control of the virtual synchronous generator was presented and the simulation results showing the effectiveness as covered in first section in Chapter 5. Also the second section in Chapter 6 explains the implemented models and presents the comparison between models for the VSG and SG. The response of the VSG and synchronous generator were studied under varying operating conditions which includes variations in the grid frequency, reactive power demand and inertia time constant.

Lastly, chapter 6 present empirical simulation results to determine power and energy ratings for the battery energy storage to for set values of inertia emulation and damping control. The estimated size of these devices to maintain the stability of the system was also observed.

8.2 Conclusions

This dissertation developed and implemented and tested a VSG by adding a battery energy storage system on the dc link of the inverter for a PV system. The dc/dc converter for BESS provides voltage regulation for dc link voltage allowing the inverter setpoint to be controlled using the swing equation. This was successfully demonstrated using simulation with the VSG connected to a 9 bus system.

The virtual synchronous generator was implemented in such a way that it overcomes the renewable energy sources shortcomings. VSG was modeled to mimic both the steady state and the transient characteristics of the SG. The dynamic response of the virtual synchronous generator to transient disturbance in the power grid was compared to the response of the synchronous generator under similar operating conditions. It is clear from the results that the virtual synchronous generator can be deployed in place of synchronous generator because of the similar dynamic behavior of both models to varying operating conditions. However, the VSG needs sufficient voltage and current ratings for the voltage source converter, and enough energy storage (energy and power ratings). This study confirms that VSG can indeed be controlled to exhibit similar dynamic response as that of the conventional synchronous generator.

8.3 Future Work

The following research topics can be explored to build on the results in this dissertation.

- The dissertation implements VSG based on swing equation using battery energy storage. Future researchers could look at the trade-offs between using battery energy storage, flywheel energy storage or other energy storage technologies.
- The proposed approach could be improved by having a more detailed model of the PV system and more comprehensive scenarios. This improved system model will include more detailed implementations of PV during 12 months duration, such as irradiation change or the temperature. This would make it possible to extend study on the impacts of disturbances on this system; find the response of the VSG on these proceedings, and what is the big energy storage capacity requirement to make the system stable in response to disturbances.
- This research implemented the VSG on a single PV inverter with storage connected to a small ac system with one synchronous generator. Future researchers should look at cases with a large number of PV inverters with installations at widely spaced buses. This can be used to address multiple research questions including: what percentage of the PV inverters need storage added, developing a decentralized control for dispersed VSGs, and addressing performance during variable cloud conditions when there could be demands on the storage to only cover PV output variations.
- This model was implemented BESS combined with PV that is connection in the dc link of the inverter. Further research could explore connecting the battery energy storage system to the ac system through a dedicated voltage source converter and compare complexity, efficiency and cost.

- For further study, another approach such as stochastic optimization calculate the optimal energy sizing can be applied to.
- Cost-benefit studies were not discussed in this research. In future study, the cost estimation for different approaches to address the challenges of reduced inertia can be explored. .
- In what ways will the new services affect investment in energy storage?
- To what degree can the energy storage improve the system's stability during severe frequency event?

Bibliography

- [1] Hongbin Wu et al. “Energy management and control strategy of a grid-connected PV/battery system”. In: *International Transactions on Electrical Energy Systems* 25.8 (2015), pp. 1590–1602.
- [2] Mohammed Benidris and Joydeep Mitra. “Enhancing stability performance of renewable energy generators by utilizing virtual inertia”. In: *2012 IEEE Power and Energy Society General Meeting*. 2012, pp. 1–6.
- [3] Paulo F Ribeiro et al. “Energy storage systems for advanced power applications”. In: *Proceedings of the IEEE* 89.12 (2001), pp. 1744–1756.
- [4] Hassan Bevrani, Toshifumi Ise, and Yushi Miura. “Virtual synchronous generators: A survey and new perspectives”. In: *International Journal of Electrical Power & Energy Systems* 54 (2014), pp. 244–254.
- [5] Andreas Ulbig, Theodor S Borsche, and Göran Andersson. “Impact of low rotational inertia on power system stability and operation”. In: *IFAC Proceedings Volumes* 47.3 (2014), pp. 7290–7297.
- [6] Alok Kumar Mohanty and Amar Kumar Barik. “Power system stability improvement using FACTS devices”. In: *International Journal of Modern Engineering Research (IJMER)* 1.2 (2011), pp. 666–672.
- [7] DM Greenwood et al. “Frequency response services designed for energy storage”. In: *Applied Energy* 203 (2017), pp. 115–127.
- [8] K Sakimoto, Y Miura, and T Ise. “Stabilization of a power system with a distributed generator by a virtual synchronous generator function”. In: *8th International Conference on Power Electronics-ECCE Asia*. 2011, pp. 1498–1505.
- [9] Amir Hosein Azizi and Mohsen Rahimi. “Dynamic performance analysis, stability margin improvement and transfer power capability enhancement in DFIG

- based wind turbines at weak ac grid conditions”. In: *International Journal of Electrical Power & Energy Systems* 99 (2018), pp. 434–446.
- [10] Tine L Vandoorn et al. “Microgrids: Hierarchical control and an overview of the control and reserve management strategies”. In: *IEEE industrial electronics magazine* 7.4 (2013), pp. 42–55.
- [11] Ujjwol Tamrakar et al. “Virtual inertia: Current trends and future directions”. In: *Applied Sciences* 7.7 (2017), p. 654.
- [12] Aboutaleb Haddadi et al. “Impact of Wind Generation on Power Swing Protection”. In: *IEEE Transactions on Power Delivery* 34.3 (2019), pp. 1118–1128.
- [13] V Salehi, S Afsharnia, and S Kahrobaee. “Improvement of voltage stability in wind farm connection to distribution network using FACTS devices”. In: *IECON 2006-32nd Annual Conference on IEEE Industrial Electronics*. 2006, pp. 4242–4247.
- [14] Nimit Boonpirom and Kitti Paitoonwattanakij. “Static voltage stability enhancement using FACTS”. In: *2005 International Power Engineering Conference*. 2005, pp. 711–715.
- [15] Asha Vijayan and S Padma. “Maintaining Voltage Stability in Power System using FACTS Devices”. In: *International Journal of Engineering Science Invention* 2.2 (2013), pp. 1–6.
- [16] Fariba Shavakhi Zavareh, Hadi Fotoohabadi, and Reza Sedaghati. “Improvement of Voltage Profile of Grid Integrated Wind Distributed Generation by SVC”. In: *system* 1 (2015), p. 3.
- [17] J Driesen and K Visscher. “Virtual synchronous generators”. In: *2008 IEEE Power and Energy Society General Meeting-Conversion and Delivery of Electrical Energy in the 21st Century*. 2008, pp. 1–3.

- [18] Amirnaser Yazdani and Reza Iravani. *Voltage-sourced converters in power systems*. Vol. 34. Wiley Online Library, 2010.
- [19] Prabha Kundur, Neal J Balu, and Mark G Lauby. *Power System Stability and Sontrol*. Vol. 7. McGraw-Hill New York, 1994.
- [20] Jan Machowski, Janusz Bialek, and Jim Bumby. *Power system dynamics: stability and control*. John Wiley & Sons, 2011.
- [21] J Duncan Glover, Mulukutla S Sarma, and Thomas Overbye. *Power System Analysis & Design, SI Version*. Cengage Learning, 2012.
- [22] Paul M Anderson and Aziz A Fouad. *Power system control and stability*. John Wiley & Sons, 2008.
- [23] Michael John Gibbard, David J Vowles, and Pouyan Pourbeik. *Small-signal stability, control and dynamic performance of power systems*. University of Adelaide Press, 2015.
- [24] Daniel Remon, Antoni Mir Cantarellas, and Pedro Rodriguez. “Equivalent model of large-scale synchronous photovoltaic power plants”. In: *IEEE Transactions on Industry Applications* 52.6 (2016), pp. 5029–5040.
- [25] Antonio Gomez-Exposito, Antonio J Conejo, and Claudio Canizares. *Electric energy systems: analysis and operation*. CRC press, 2018.
- [26] Oluwafemi E Oni, Innocent E Davidson, and Kamati NI Mbangula. “Dynamic voltage stability studies using a modified IEEE 30-bus system”. In: *2016 IEEE 16th International Conference on Environment and Electrical Engineering (EEEIC)*. IEEE. 2016, pp. 1–6.
- [27] Alexandre Oudalov, Daniel Chartouni, and Christian Ohler. “Optimizing a battery energy storage system for primary frequency control”. In: *IEEE Transactions on Power Systems* 22.3 (2007), pp. 1259–1266.

- [28] Vaclav Knap et al. “Grid inertial response with lithium-ion battery energy storage systems”. In: *2014 IEEE 23rd International Symposium on Industrial Electronics (ISIE)*. IEEE, pp. 1817–1822, 2014.
- [29] Federico Milano. *Power system modelling and scripting*. Springer Science & Business Media, 2010.
- [30] Fam Moura et al. “The dynamic interaction of independent power producer synchronous machines connected to a distribution network in ATP-EMTP”. In: *The XIX International Conference on Electrical Machines-ICEM 2010*. 2010, pp. 1–6.
- [31] Simon Hobi. “Simulation of a Synchronous Machine Model”. In: *Power Syst. Lab* (2018).
- [32] SR Oscar. “Small-signal modelling and stability analysis of a traditional generation unit and a virtual synchronous machine in grid-connected operation”. In: *Trondheim, Norway: Delft University of Technology* (2015).
- [33] Jia Liu et al. “Parallel operation of a synchronous generator and a virtual synchronous generator under unbalanced loading condition in microgrids”. In: *2016 IEEE 8th International Power Electronics and Motion Control Conference (IPEMC-ECCE Asia)*. 2016, pp. 3741–3748.
- [34] Salvatore D’Arco and Jon Are Suul. “Small-signal analysis of an isolated power system controlled by a virtual synchronous machine”. In: *2016 IEEE International Power Electronics and Motion Control Conference (PEMC)*. 2016, pp. 462–469.
- [35] Remus Teodorescu, Marco Liserre, and Pedro Rodriguez. *Grid converters for photovoltaic and wind power systems*. Vol. 29. John Wiley & Sons, 2011.

- [36] Elyas Rakhshani and Pedro Rodriguez. “Inertia emulation in AC/DC interconnected power systems using derivative technique considering frequency measurement effects”. In: *IEEE Transactions on Power Systems* 32.5 (2016), pp. 3338–3351.
- [37] Ali Q Al-Shetwi and Muhamad Zahim Sujod. “Grid-connected photovoltaic power plants: A review of the recent integration requirements in modern grid codes”. In: *International Journal of Energy Research* 42.5 (2018), pp. 1849–1865.
- [38] Jia Liu, Yushi Miura, and Toshifumi Ise. “A novel oscillation damping method of virtual synchronous generator control without PLL using pole placement”. In: *2018 International Power Electronics Conference (IPEC-Niigata 2018-ECCE Asia)*. IEEE. 2018, pp. 775–781.
- [39] Salvatore DâArco, Jon Are Suul, and Olav B Fosso. “A Virtual Synchronous Machine implementation for distributed control of power converters in Smart-Grids”. In: *Electric Power Systems Research* 122 (2015), pp. 180–197.
- [40] Saeed Golestan et al. “Droop based control of parallel-connected single-phase inverters in DQ rotating frame”. In: *2009 IEEE International Conference on Industrial Technology*. 2009, pp. 1–6.
- [41] Tatjana Kalitjuka. “Control of voltage source converters for power system applications”. MA thesis. Institutt for elkraftteknikk, 2011.
- [42] Md Ashraful Islam. *Implementation of virtual synchronous generator methodologies for renewable integration*. Temple University, 2017.
- [43] T Navpreet et al. “Voltage source converters as the building block of HVDC and FACTS technology in power transmission system: a simulation based approach”. In: *Advances in Applied Science Research* 3.5 (2012), pp. 3263–3278.

- [44] Nagaraju Pogaku, Milan Prodanovic, and Timothy C Green. “Modeling, analysis and testing of autonomous operation of an inverter-based microgrid”. In: *IEEE Transactions on power electronics* 22.2 (2007), pp. 613–625.
- [45] Mahdi Ghadiri, Ali Moeini, and Hossein Yassami. “Impact of Islanding on Governor Signal of Distributed Resources”. In: *Journal of Electromagnetic Analysis and Applications* 3.02 (2011), p. 56.
- [46] Olve Mo, Salvatore D’Arco, and Jon Are Suul. “Evaluation of virtual synchronous machines with dynamic or quasi-stationary machine models”. In: *IEEE Transactions on industrial Electronics* 64.7 (2016), pp. 5952–5962.
- [47] Bingtuan Gao et al. “Virtual synchronous generator based auxiliary damping control design for the power system with renewable generation”. In: *Energies* 10.8 (2017), p. 1146.
- [48] Yanbo Che et al. “An improved coordinated control strategy for PV system integration with VSC-MVDC technology”. In: *Energies* 10.10 (2017), p. 1670.
- [49] Salvatore D’Arco, Jon Are Suul, and Olav B Fosso. “Control system tuning and stability analysis of virtual synchronous machines”. In: *2013 IEEE Energy Conversion Congress and Exposition*. 2013, pp. 2664–2671.
- [50] Jianhui Meng et al. “A virtual synchronous generator control strategy for distributed generation”. In: *2014 China International Conference on Electricity Distribution (CICED)*. 2014, pp. 495–498.
- [51] Krzysztof Szabat and Teresa Orłowska-Kowalska. “Vibration suppression in a two-mass drive system using PI speed controller and additional feedbacks Comparative study”. In: *IEEE Transactions on Industrial Electronics* 54.2 (2007), pp. 1193–1206.

- [52] Xiangwu Yan et al. “Research on distributed PV storage virtual synchronous generator system and its static frequency characteristic analysis”. In: *Applied Sciences* 8.4 (2018), p. 532.
- [53] Mohamed Abuagreb, Mohammed Allehyani, and Brian K Johnson. “Design and Test of a Combined PV and Battery System Under Multiple Load and Irradiation Conditions”. In: *2019 IEEE Power & Energy Society Innovative Smart Grid Technologies Conference (ISGT)*. IEEE. 2019, pp. 1–5.
- [54] Vaclav Knap et al. “Sizing of an energy storage system for grid inertial response and primary frequency reserve”. In: *IEEE Transactions on Power Systems* 31.5 (2015), pp. 3447–3456.
- [55] Simone Barcellona et al. “Control strategy of virtual synchronous generator based on virtual impedance and band-pass damping”. In: *2016 International Symposium on Power Electronics, Electrical Drives, Automation and Motion (SPEEDAM)*. 2016, pp. 1354–1362.
- [56] Nahidul Hoque Samrat et al. “Modeling, control, and simulation of battery storage photovoltaic-wave energy hybrid renewable power generation systems for island electrification in Malaysia”. In: *The Scientific World Journal* 2014 (2014).
- [57] Narsa Reddy Tummuru, Mahesh K Mishra, and S Srinivas. “Dynamic energy management of hybrid energy storage system with high-gain PV converter”. In: *IEEE Transactions on Energy Conversion* 30.1 (2014), pp. 150–160.
- [58] Yiqun Wang et al. “Storage-less and converter-less photovoltaic energy harvesting with maximum power point tracking for internet of things”. In: *IEEE Transactions on Computer-Aided Design of Integrated Circuits and Systems* 35.2 (2015), pp. 173–186.

- [59] S Sumathi, L Ashok Kumar, and P Surekha. “Application of matlab/simulink in solar PV systems”. In: *Solar PV and Wind Energy Conversion Systems*. Springer, 2015, pp. 59–143.
- [60] Jonathan W Kimball and Philip T Krein. “Discrete-time ripple correlation control for maximum power point tracking”. In: *IEEE Transactions on Power Electronics* 23.5 (2008), pp. 2353–2362.
- [61] Xiong Liu, Peng Wang, and Poh Chiang Loh. “A hybrid AC/DC microgrid and its coordination control”. In: *IEEE Transactions on smart grid* 2.2 (2011), pp. 278–286.
- [62] Abosalah ElMehdi et al. “Analysis, modeling, and control of a stand-alone photovoltaic generation system”. In: *2016 4th International Conference on Control Engineering & Information Technology (CEIT)*. IEEE. 2016, pp. 1–6.
- [63] KL Lian, JH Jhang, and IS Tian. “A maximum power point tracking method based on perturb-and-observe combined with particle swarm optimization”. In: *IEEE journal of photovoltaics* 4.2 (2014), pp. 626–633.
- [64] Nevzat Onat. “Recent developments in maximum power point tracking technologies for photovoltaic systems”. In: *International Journal of Photoenergy* 2010 (2010).
- [65] Fei Ding et al. “Modeling and simulation of grid-connected hybrid photovoltaic/-battery distributed generation system”. In: *CICED 2010 Proceedings*. 2010, pp. 1–10.
- [66] Mauricio Restrepo et al. “Modeling and testing of a bidirectional smart charger for distribution system EV integration”. In: *IEEE Transactions on Smart Grid* 9.1 (2016), pp. 152–162.

- [67] Ibrahim Sefik and Dimas Anton Asfani. “Performance analysis of hybrid electric vehicle with electric double layer capacitor under short circuit fault”. In: *International Journal of Innovative computing Information and Control* 11.1 (2015), pp. 257–280.
- [68] Essam M Allam. “Study Vehicle Battery Simulation and Monitoring System”. In: *American Journal of Modeling and Optimization* 3.2 (2015), pp. 40–49.
- [69] Mahmoud Hussein et al. “Control of a stand-alone variable speed wind energy supply system”. In: *Applied Sciences* 3.2 (2013), pp. 437–456.
- [70] Mattia Marinelli et al. “Testing of a predictive control strategy for balancing renewable sources in a microgrid”. In: *IEEE Transactions on Sustainable Energy* 5.4 (2014), pp. 1426–1433.
- [71] Lie Xu and Dong Chen. “Control and operation of a DC microgrid with variable generation and energy storage”. In: *IEEE Transactions on Power Delivery* 26.4 (2011), pp. 2513–2522.
- [72] Xiaoyu Wang, Meng Yue, and Eduard Muljadi. “PV generation enhancement with a virtual inertia emulator to provide inertial response to the grid”. In: *2014 IEEE Energy Conversion Congress and Exposition (ECCE)*. 2014, pp. 17–23.
- [73] Yunjie Gu, Wuhua Li, and Xiangning He. “Frequency-coordinating virtual impedance for autonomous power management of DC microgrid”. In: *IEEE Transactions on Power Electronics* 30.4 (2014), pp. 2328–2337.
- [74] Xin Meng, Jinjun Liu, and Zeng Liu. “A Generalized Droop Control for Grid-Supporting Inverter Based on Comparison Between Traditional Droop Control and Virtual Synchronous Generator Control”. In: *IEEE Transactions on Power Electronics* 34.6 (2018), pp. 5416–5438.

- [75] Qing-Chang Zhong et al. “Self-synchronized synchronverters: Inverters without a dedicated synchronization unit”. In: *IEEE Transactions on power electronics* 29.2 (2013), pp. 617–630.
- [76] Xin Meng et al. “Comparison between virtual synchronous generator and droop controlled inverter”. In: *2016 IEEE 2nd Annual Southern Power Electronics Conference (SPEC)*. 2016, pp. 1–6.
- [77] Qing-Chang Zhong and George Weiss. “Synchronverters: Inverters that mimic synchronous generators”. In: *IEEE Transactions on Industrial Electronics* 58.4 (2010), pp. 1259–1267.
- [78] Xiangwu Yan et al. “Parallel operation of virtual synchronous generators and synchronous generators in a microgrid”. In: *The Journal of Engineering* 2019.16 (2019), pp. 2635–2642.
- [79] Heng Wu et al. “Small-signal modeling and parameters design for virtual synchronous generators”. In: *IEEE Transactions on Industrial Electronics* 63.7 (2016), pp. 4292–4303.
- [80] Jiebei Zhu et al. “Inertia emulation control strategy for VSC-HVDC transmission systems”. In: *IEEE Transactions on Power Systems* 28.2 (2012), pp. 1277–1287.

Appendix A: Virtual Synchronous Generator, Synchronous Generator, and PV Model Parameters

The parameters of the VSG, SG, and PV model parameters are listed in Tables A.1 through A.4. Some of these parameters come from [5], and other parameters were tuned in the Simulink to make the system stable.

Table A.1: Virtual Synchronous Generator Parameters

Description	Name	value	Unit
Rated Power	S	2.75	MVA
Rated nominal voltage	$V_{LL,RMS}$	690	V
Rated angular frequency	ω_b	$2\pi \cdot f$	rad/s
Frequency droop gain	K_ω	20	pu
Reactor power droop gain	K_q	0.2	pu
Damping factor	K_d	400	
Inertia time constant	T_a	2	sec
Active power reference		0.5	pu
Reactive power reference	q	0.0	pu
Voltage reference		1.02	pu
Voltage controller gains	K_{pv}, K_{iv}	0.59, 736	
Current controller gains	K_{pc}, K_{ic}	1.27, 14.3	
Reactive power filter	ω_f	1000	rad/s
Filter resistance	r_f	0.003	pu
Filter inductance	l_f	0.08	pu
Filter capacitance	c_f	0.074	pu
Grid resistance	r_g	0.01	pu
Grid inductance	l_g	0.2	pu
Grid voltage	v_g	1.0	pu
Virtual resistance	r_v	0.0	pu
Virtual inductance	l_v	0.2	Pu
Active damping gain	K_{AD}	0.5	pu
Active damping filter	ω_{AD}	60	rad/s

Table A.2: Synchronous generator governor and exciter parameters

Description	Name	value	Unit
Frequency droop gain	$K_{\omega,SG}$	20	pu
Angular frequency reference	ω_{SG}^*	1	pu
Reactive power droop gain	$K_{q,SG}$	0.2	pu
Damping factor	$K_{d,SG}$	0	
Inertia time constant	T_{SG}	2	sec
Active power reference	P_{SG}^*	0.5	pu
Reactive power reference	q_{SG}^*	0.0	pu
Voltage reference	V_{SG}^*	1.00	pu
Proportional gain	K_{pex}	0.0235	
Integral gain	K_{iex}	0.00503	
Time constant for exciter	T_{ex}	0.1	sec
Time-constant	T_{gt}	0.5	sec
Reactive power filter	$\omega_{f,SG}$	1000	rad/s
Grid angular frequency	ω_G	1	pu
Grid voltage	v_g	1.0	pu

Table A.3: Synchronous generator machine parameters

Description	value	Unit
Rated power	2.75	MVA
Nominal rated voltage	690	V
Rated angular frequency	60	rad/sec
Number of poles (pole pairs *2)	8	
Armature resistance	0.004	pu
Synchronous reactance d-axis	1.8	pu
Synchronous reactance q-axis	1.672	pu
Leakage reactance	0.1	pu
Transient reactance d-axis	0.166	pu
Transient reactance q-axis	0.98	pu
Subtransient reactance d-axis	0.119	pu
Subtransient reactance q-axis	0.17	pu
Zero sequence reactance	0.046	pu
Open circuit time const in d-axis	1.754	sec
Open circuit time const in q axis	0	sec
Open circuit subtransient time const in d axis	0.019	sec
Open circuit subtransient time const in q axis	0.164	sec

Table A.4: The parameters of the KC200GT solar array at 25°C , $1000\text{W}/\text{m}^2$ [8]

Parameters	Symbol	Value
Voltage-temperature coefficient	K_V	-0.123v/K
Current-temperature coefficient	K_i	0.0032A/K
Open-circuit voltage at T_n and G_n	V_{0cn}	32.9V
Short-circuit current at T_n and G_n	I_{scn}	8.2 A
Experimental maximum power	$P_{max,e}$	200.14W
Current at maximum power	I_{mp}	7.6 A
Voltage at maximum power	V_{mp}	26.3
Parallel numbers of PV modules	N_p	500
Serious numbers of PV modules	N_s	24

Appendix B: Virtual synchronous generator control and simple dynamic machine model implemented in ATPDraw

B.1 Reactive Power Control, Governor and VSG swing equation

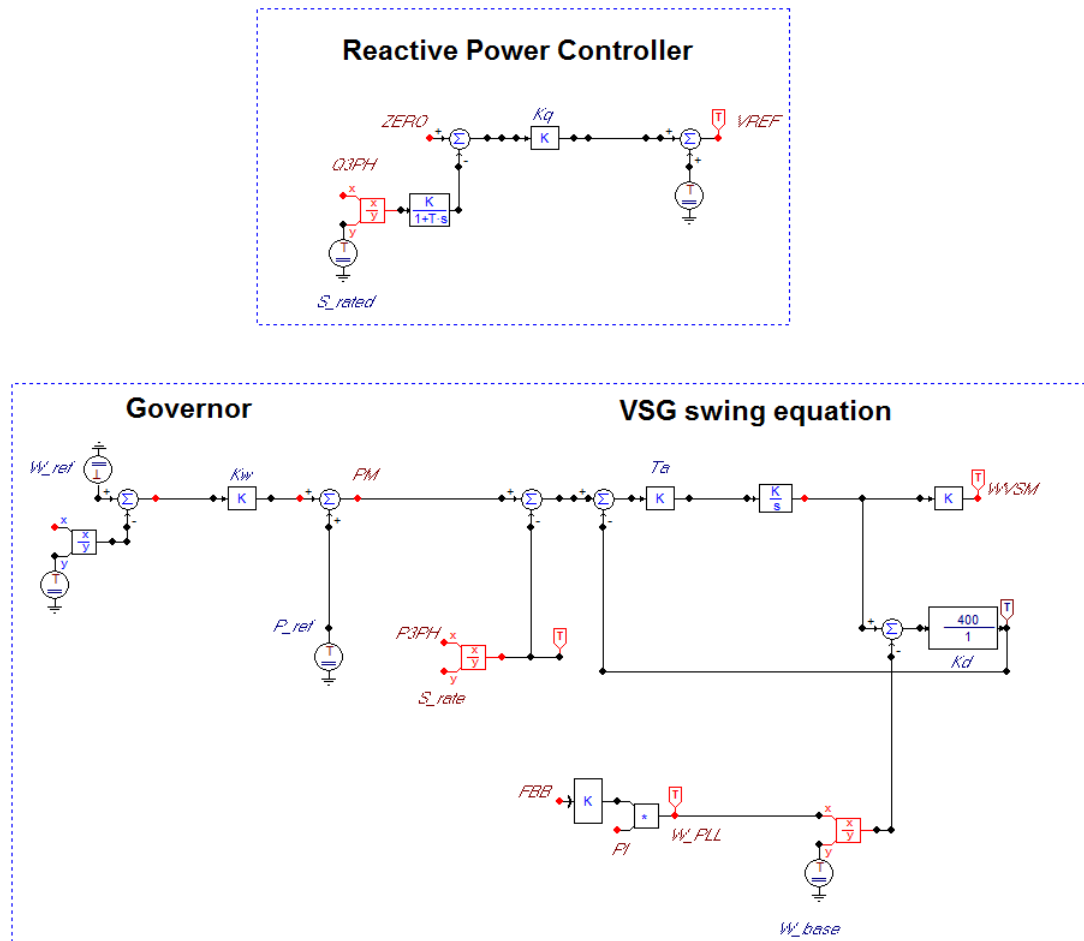


Figure B.1: Reactive Power Droop Control and VSG Inertia with Governor

B.2 Virtual Impedance, Voltage Control and Current Control

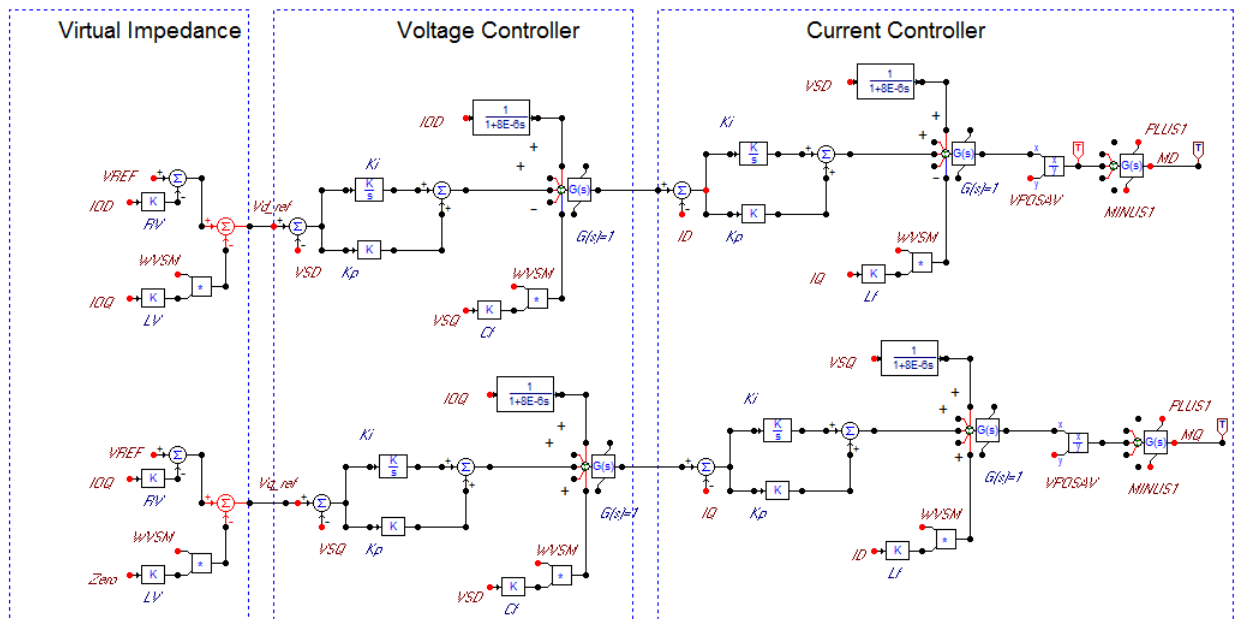


Figure B.2: Virtual Impedance, Voltage and Current Controllers of VSG implemented in ATPDraw

B.3 Synchronous Generator Parameters

Component: SM

Attributes

DATA	UNIT	VALUE	NODE	PHASE	NAME
Frequency	Hz	60	BUS	ABC	VBUS1
Power	MVA	2.749	POWER	1	PM
Voltage L-L	kVrms	0.69	EXFD	1	V_EX
Poles	2*PP	8	EXOUT1	1	WS0
Ra	pu	0.004			
Xd	pu	1.8			
Xq	pu	1.793			
Xl	pu	0.1			

Copy Paste Reset Order: 0 Label:

Comment:

General Field current Masses Output

Steady state
 Volt: [V]p L-G
 Ang: [deg]

Time constants
 Open Short
 Delta connection
 Type 58 (phase)

Parallel operation Hide

Edit definitions OK Cancel Help

Figure B.3: Parameters of Synchronous Generator implemented in ATPDraw

Appendix C: Average model boost converter and Phase Locked Loop

C.1 DC/DC Boost Converter Average Model

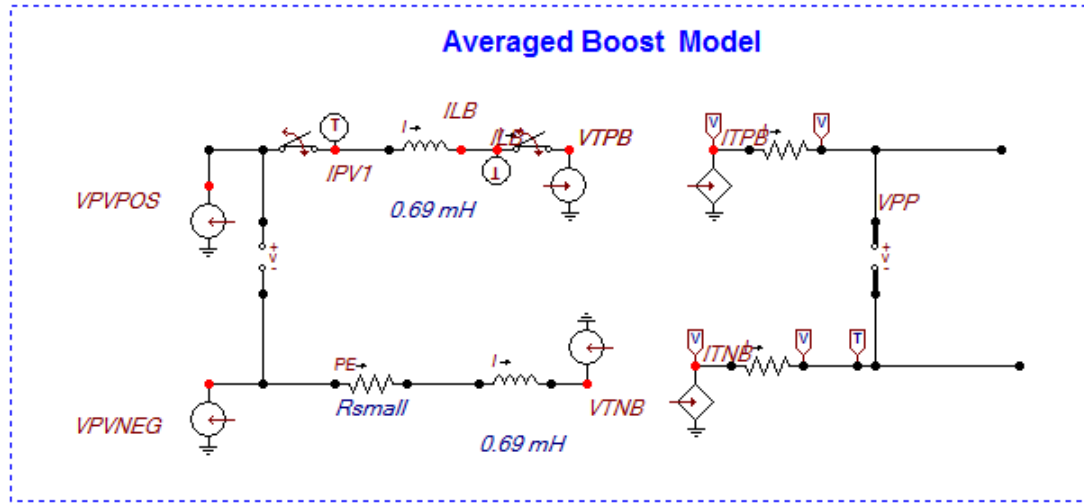


Figure C.1: DC/DC converter average model implemented in ATPDraw

C.2 Bidirectional Buck Boost Converter Average Model

The state equations of BDBBC average model as shown in equations (C.1 and (C.2)

$$L \frac{d}{dt} i_L(t) = V_g(t) - V_c(1 - d)(t) \quad (C.1)$$

$$C \frac{d}{dt} V_C(t) = i_L(1 - d)(t) - I_0(t) \quad (C.2)$$

Where:

$V_g(t)$ is voltage input of the converter (V).

$I_o(t)$ is the output current of the converter (A).

$i_L(t)$ is inductor current (A).

$V_C(t)$ is capacitor voltage (V).

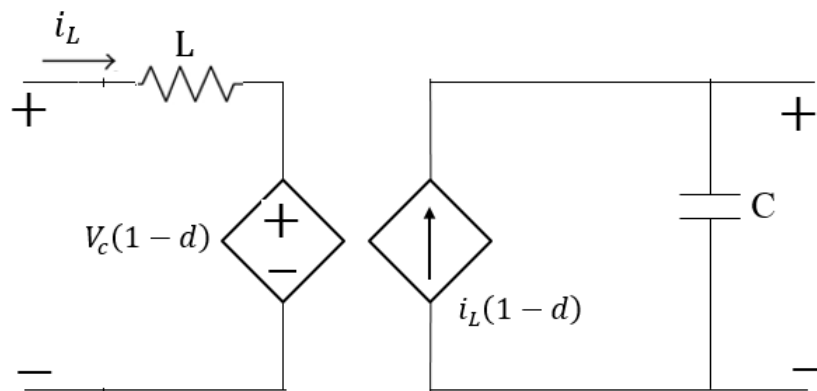


Figure C.2: DC/DC converter average model implemented in ATPDraw

C.3 Phase-Locked Loop

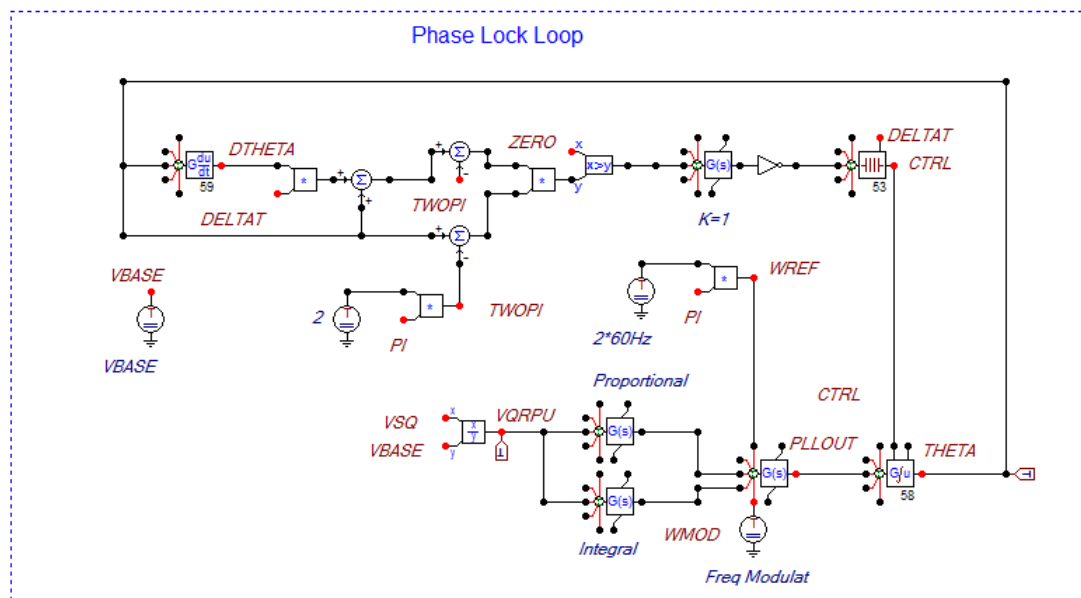


Figure C.3: Schematic Diagram of the PLL implemented in ATPDraw

Appendix D: IEEE Formal Reuse License

As list in the Chapter 5 and Chapter 6, some of the content of these chapters are currently copyrighted by the Institute of Electrical and Electronics Engineers Inc. (IEEE). Permission for reproduction of the complete article for use in this dissertation has been given by (IEEE). Figures D.1, D.2 and D.3 are proofs of this permission. The content of these reproduced articles has been changed to suit the format of dissertation; instead of a scholarly article. The numbering of figures and listings has changed, due to being reproduced in this dissertation. However, the figures and listings, and their captions themselves remain uncharged. Also, some paragraphs may have gone through minor edits resulting from the dissertation review and editing process. There are also present in this dissertation chapters, figures and paragraphs not present in the publications. This is due to work performed after paper submission and publication, and also not included due to conference proceeding length limitations.



**Copyright
Clearance
Center**




Home


Help


Email Support


Sign in


Create Account



Requesting
permission
to reuse
content from
an IEEE
publication

Design and Test of a Combined PV and Battery System Under Multiple Load and Irradiation Conditions

Conference Proceedings:
2019 IEEE Power & Energy Society Innovative Smart Grid Technologies Conference (ISGT)

Author: Mohamed Abuagreb

Publisher: IEEE

Date: Feb. 2019

Copyright © 2019, IEEE

Thesis / Dissertation Reuse

The IEEE does not require individuals working on a thesis to obtain a formal reuse license, however, you may print out this statement to be used as a permission grant:

Requirements to be followed when using any portion (e.g., figure, graph, table, or textual material) of an IEEE copyrighted paper in a thesis:

- 1) In the case of textual material (e.g., using short quotes or referring to the work within these papers) users must give full credit to the original source (author, paper, publication) followed by the IEEE copyright line © 2011 IEEE.
- 2) In the case of illustrations or tabular material, we require that the copyright line © [Year of original publication] IEEE appear prominently with each reprinted figure and/or table.
- 3) If a substantial portion of the original paper is to be used, and if you are not the senior author, also obtain the senior author's approval.

Requirements to be followed when using an entire IEEE copyrighted paper in a thesis:


- 1) The following IEEE copyright/ credit notice should be placed prominently in the references: © [year of original publication] IEEE. Reprinted, with permission, from [author names, paper title, IEEE publication title, and month/year of publication]
- 2) Only the accepted version of an IEEE copyrighted paper can be used when posting the paper or your thesis on-line.
- 3) In placing the thesis on the author's university website, please display the following message in a prominent place on the website: In reference to IEEE copyrighted material which is used with permission in this thesis, the IEEE does not endorse any of [university/educational entity's name goes here]'s products or services. Internal or personal use of this material is permitted. If interested in reprinting/republishing IEEE copyrighted material for advertising or promotional purposes or for creating new collective works for resale or redistribution, please go to http://www.ieee.org/publications_standards/publications/rights/rights_link.html to learn how to obtain a License from RightsLink.

If applicable, University Microfilms and/or ProQuest Library, or the Archives of Canada may supply single copies of the dissertation.


BACK


CLOSE WINDOW


Figure D.1: Permission from IEEE to Reproduce an Article as Chapter 5 of this Dissertation





**Copyright
Clearance
Center**






Home


Help


Email Support


Sign in


Create Account



Requesting
permission
to reuse
content from
an IEEE
publication

Energy Management of a Battery Combined with PV Generation

Conference Proceedings: 2019 North American Power Symposium (NAPS)

Author: [::Mohamed::] [::Abuagreb::]; Hussain Beleed; Brian K. Johnson

Publisher: IEEE

Date: 13-15 Oct. 2019

Copyright © 2019, IEEE

Thesis / Dissertation Reuse

The IEEE does not require individuals working on a thesis to obtain a formal reuse license, however, you may print out this statement to be used as a permission grant:

Requirements to be followed when using any portion (e.g., figure, graph, table, or textual material) of an IEEE copyrighted paper in a thesis:

- 1) In the case of textual material (e.g., using short quotes or referring to the work within these papers) users must give full credit to the original source (author, paper, publication) followed by the IEEE copyright line © 2011 IEEE.
- 2) In the case of illustrations or tabular material, we require that the copyright line © [Year of original publication] IEEE appear prominently with each reprinted figure and/or table.
- 3) If a substantial portion of the original paper is to be used, and if you are not the senior author, also obtain the senior author's approval.

Requirements to be followed when using an entire IEEE copyrighted paper in a thesis:

- 1) The following IEEE copyright/ credit notice should be placed prominently in the references: © [year of original publication] IEEE. Reprinted, with permission, from [author names, paper title, IEEE publication title, and month/year of publication]
- 2) Only the accepted version of an IEEE copyrighted paper can be used when posting the paper or your thesis on-line.
- 3) In placing the thesis on the author's university website, please display the following message in a prominent place on the website: In reference to IEEE copyrighted material which is used with permission in this thesis, the IEEE does not endorse any of [university/educational entity's name goes here]'s products or services. Internal or personal use of this material is permitted. If interested in reprinting/republishing IEEE copyrighted material for advertising or promotional purposes or for creating new collective works for resale or redistribution, please go to http://www.ieee.org/publications_standards/publications/rights/rights_link.html to learn how to obtain a License from RightsLink.

If applicable, University Microfilms and/or ProQuest Library, or the Archives of Canada may supply single copies of the dissertation.

BACK

CLOSE WINDOW

Figure D.2: Permission from IEEE to Reproduce an Article as Chapter 5 of this Dissertation



Copyright Clearance Center




Home


Help


Email Support


Sign in


Create Account



Requesting permission to reuse content from an IEEE publication

Design and Test of a Combined PV and Battery System Under Multiple Load and Irradiation Conditions

Conference Proceedings:
2019 IEEE Power & Energy Society Innovative Smart Grid Technologies Conference (ISGT)

Author: Mohamed Abuagreb

Publisher: IEEE

Date: Feb. 2019

Copyright © 2019, IEEE

Thesis / Dissertation Reuse

The IEEE does not require individuals working on a thesis to obtain a formal reuse license, however, you may print out this statement to be used as a permission grant:

Requirements to be followed when using any portion (e.g., figure, graph, table, or textual material) of an IEEE copyrighted paper in a thesis:

- 1) In the case of textual material (e.g., using short quotes or referring to the work within these papers) users must give full credit to the original source (author, paper, publication) followed by the IEEE copyright line © 2011 IEEE.
- 2) In the case of illustrations or tabular material, we require that the copyright line © [Year of original publication] IEEE appear prominently with each reprinted figure and/or table.
- 3) If a substantial portion of the original paper is to be used, and if you are not the senior author, also obtain the senior author's approval.

Requirements to be followed when using an entire IEEE copyrighted paper in a thesis:

- 1) The following IEEE copyright/ credit notice should be placed prominently in the references: © [year of original publication] IEEE. Reprinted, with permission, from [author names, paper title, IEEE publication title, and month/year of publication]
- 2) Only the accepted version of an IEEE copyrighted paper can be used when posting the paper or your thesis on-line.
- 3) In placing the thesis on the author's university website, please display the following message in a prominent place on the website: In reference to IEEE copyrighted material which is used with permission in this thesis, the IEEE does not endorse any of [university/educational entity's name goes here]'s products or services. Internal or personal use of this material is permitted. If interested in reprinting/republishing IEEE copyrighted material for advertising or promotional purposes or for creating new collective works for resale or redistribution, please go to http://www.ieee.org/publications_standards/publications/rights/rights_link.html to learn how to obtain a License from RightsLink.

If applicable, University Microfilms and/or ProQuest Library, or the Archives of Canada may supply single copies of the dissertation.

BACK

CLOSE WINDOW

Figure D.3: Permission from IEEE to Reproduce an Article as Chapter 6 of this Dissertation